UNIVERSITY OF SIENA

DEPARTMENT OF BIOTECHNOLOGY,
CHEMISTRY AND PHARMACY

DOCTORAL THESIS IN
BIOCHEMISTRY AND MOLECULAR BIOLOGY
Cycle XXXV

Coordinator: Prof. Lorenza Trabalzini

Development of Advanced Tests for Bio-inspired Hybrid Organic-Inorganic Electronic Devices

SCIENTIFIC-DISCIPLINARY SECTOR: BIO/10

Supervisor:
Prof. Annalisa Santucci
Co-Supervisor:
Dr. Lucio Cinà

Candidate:
Bastiaan de Jong

Academic year 2022 – 2023

Bastiaan De Jong

ABSTRACT

This thesis describes the management and development of an advanced testing platform for bio-inspired hybrid organic-inorganic devices. with the help of external collaborators, perovskite (PSC) and dye-sensitized solar cells (DSSC), luminescent solar concentrators (LSC) and neuromorphic organic devices (NOD) working as artificial synapses have been characterized in steady state and transient conditions on the system. The goal of the thesis is to correlate different advances optoelectronic characterization techniques through the use of a single equipment to improve the throughput of device assessment.

The thesis is organized into three parts:

1. Steady state characterizations on the three device typologies are performed. JV and IPCE measurements for photovoltaic (PV) devices show the importance of the illumination spectra, which is emphasized by the measurements of photoluminescence for LSCs and absorption dynamics of NODs.
2. Transient analysis has been demonstrated to measure the dynamic behaviour of perovskite devices and correlate it with the improvements in the steady state tests due to the addition of a hole blocking buffer layer to the device stack.
3. A second system was developed for statistical measurements on many devices. As the stability of emerging PV technology is still under development due to fabrication inconsistencies, a high throughput many devices measurement system was developed to improve the statistics focussing on the design of a parallel maximum power point tracker.

PUBLICATIONS

1. Castro-Hermosa, S. et al. Efficient fully blade-coated perovskite solar cells in air with nanometer-thick bathocuproine buffer layer. Nano Res. 14, 1034–1042 (2021).
2. Papucci, C. et al. Luminescent solar concentrators with outstanding optical properties by employment of D–A–D quinoxaline fluorophores. J. Mater. Chem. C 9, 15608–15621 (2021).
3. D'Amico, F. , de Jong, B. et al. An Overview of Organic Dyes for Application in Dye-Sensitized Solar Cells under Indoor Lighting Conditions. MDPI (2023). *Under review*

PROCEEDINGS

1. (Poster) de Jong, B. Characterizing Charge Recombination Dynamics: From Perovskite Solar Cells to Luminescent Solar Concentrators. *HOPV22*, Valencia, 2022 (https://www.nanoge.org/proceedings/HOPV22/6260fc261f819f5c11620224)
2. (Oral) de Jong, B. Characterizing UV degradation in perovskites for space applications. *PVSPACE*, Online, 2022 (https://www.nanoge.org/PVSPACE/program-info/program)
3. (Oral) Cinà, L. et al. Charge recombination dynamics in Perovskite based devices: a guide to correlate steady-state and dynamic measurements. *ENERCHEM*-2, Padova, 2020 (https://enerchem-2.icmate.cnr.it/programme/scientific-programme)
4. (Oral) de Jong, B., Cinà, L. & Santucci, A. Charge recombination dynamics: an experimental approach from perovskite-based devices to luminescent solar concentrators. *GIF2021*, Turin, 2021 (https://www.moflabunito.com/gif2021)

DIDACTIC ACTIVITY

1. 2x: 12 hours - Profarmabio teaching activity - on the use and programming of stepper motors and their role in syringe pumping, *University of Siena*, 2021
2. 2x: 4 hours - International School on Hybrid and Organic Photovoltaics (ISOPHOS) Summer school Live hands-on session with the testing equipment on perovskite and organic solar cells, *Talamone*, 2022 & 2023 (https://www.isophos.it/)

PHOTOS OF SCIENTIFIC ACTIVITIES

(Oral) de Jong, B., Cinà, L. & Santucci, A. Charge recombination dynamics: an experimental approach from perovskite-based devices to luminescent solar concentrators. GIF2021, Turin, 2021

(Poster) de Jong, B. Characterizing Charge Recombination Dynamics: From Perovskite Solar Cells to Luminescent Solar Concentrators. HOPV22, Valencia, 2022

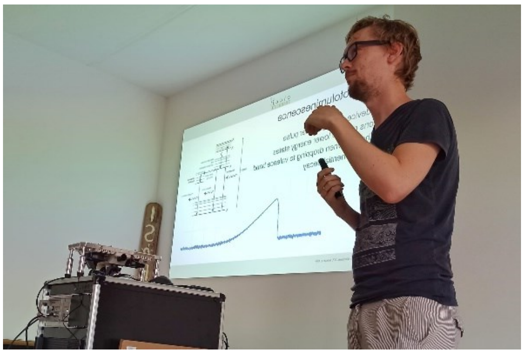

International School on Hybrid and Organic Photovoltaics (ISOPHOS) Summer school Live hands-on session with the testing equipment on perovskite and organic solar cells, Talamone, 2022 & 2023

Profarmabio teaching activity - on the use and programming of stepper motors and their role in syringe pumping, University of Siena, 2021

ACKNOWLEDGEMENTS

Thank you to the entire team of Cicci Research for the support during the years and the help in the development of the system. Special thanks to Lucio for the inspiration for this PhD work and work we did together to arrive at this point.

Thank you to prof. Annalisa Santucci for the opportunity of the PhD position.

1 TABLE OF CONTENTS

TABLE OF FIGURES

2 THE QUEST FOR ADVANCED ELECTRO-OPTICAL TESTS

The world is using more energy every year as the population grows and developing nations are increasing the wealth[1,2]. Fossil fuels are being exhausted and, due to pollution affecting the greenhouse effect, must be reduced. Renewable energy sources such as hydropower, wind and solar have rapidly increased in the last two decades as the need for clean energy became increasingly important. Solar power in particular increased the most recently due to falling costs of photovoltaic (PV) devices[3–5].

While the efficiency of regular silicon PV devices has stagnated in recent years (Figure 1), emerging technologies such as Perovskite (PSC), bio-inspired dye-sensitized (DSSC) and organic (OSC) solar cells have had rapid improvements in their efficiency and stability[6]. Standard PV applications have been limited to opaque panels mounted on roofs of private and commercial buildings or in large solar farm fields[7]. New technologies aim to broaden the application windows by allowing integration into buildings as they can be made transparent or coloured. Flexible panels printed on plastic substrates allow for more design freedom and easier integration in existing infrastructures as they are generally lightweight (Figure 2). Development of these technologies is still ongoing, especially in the fields of stability and material considerations[8–11].

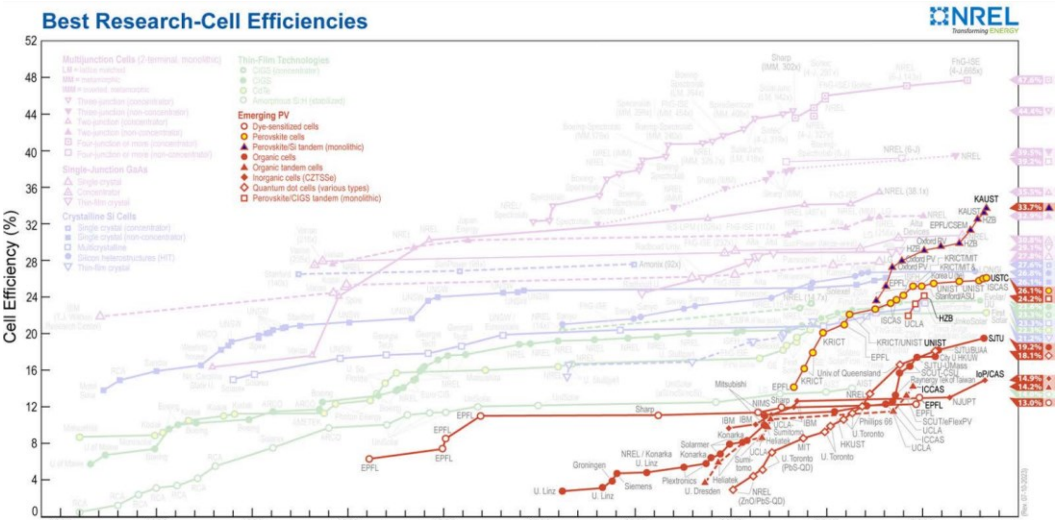

Figure 1 – Efficiency of different PV technologies over the year, with emerging technologies hightlighed[6].

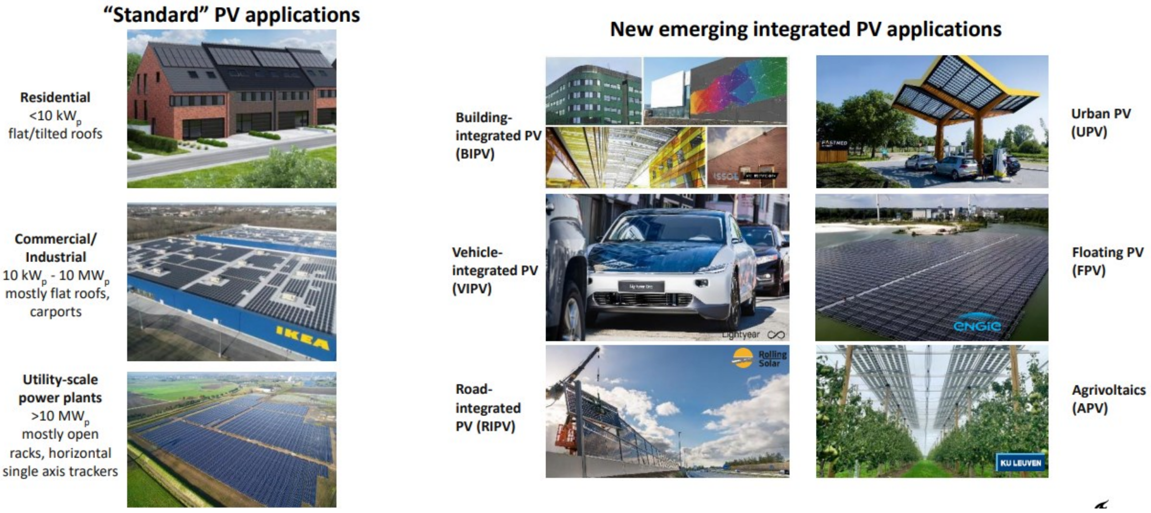

Figure 2 – Different applications for standard silicon panels and emerging technologies.

Assessing the performance of any electro-optical device requires a comprehensive understanding of its various physical behaviour and characteristics, which may influence its overall efficiency, durability, and long-term operation. There is no single test that captures the complete working behaviour of a device[10,12]. Specific tests reveal one or more physical parameters specific to the test. Combining different tests gives a more complete understanding of the performance of a device[13]. Traditional equipment is focussed on performing a single or a couple of tests. As more tests are needed for a complete understanding, the device must be transported between the different equipment locations, potentially being exposed to less-than-ideal conditions during transport.

From this problem, the solution of an all-in-one testing apparatus was born to present a groundbreaking advancement in characterization. Although the origin of the apparatus was the need for correlating advanced tests in photovoltaic devices, it became apparent that the system could be in different fields of research. Recent technologic advancements in electronic components allowed for the fast development of new experimental setups that push the boundaries of these scenarios. The focus of the research therefore extended to a wide range of bio-inspired devices such as: hybrid organic-inorganic PV devices like dye-sensitized solar cells, organic polymers used for light guiding in luminescent solar concentrators and electrochemical neuromorphic devices working as artificial synapses.

Figure 3 – Overview of a complete system showing the thermal stage, a monochromatic line, and several accessories.

This system combines multiple test procedures into a single platform, addressing the challenge of deploying various systems for different assessment protocols. By streamlining the evaluation process, we not only enhance the consistency and reproducibility of the measurements but also optimize the throughput. This is achieved through a modular architecture that can flexibly accommodate various test components, ensuring the apparatus remains adaptable to the evolving demands of PV research. Based on the evolution of characterization protocols, new hardware can be developed and added as plug-and-play modules. New software to control the system can be created based on a community consensus or a customer's specific wishes. Precision-calibrated sensors and state-of-the-art data acquisition systems ensure the accuracy of measurements, ranging from spectral response to temperature-dependent efficiency metrics. By consolidating these diverse test protocols into one cohesive unit, we enhance the operational efficiency, reduce the margin of error introduced by system-to-system variations, and provide a more complete understanding of a device's performance.

2.1 A Stage for Electrical and Environmental Control

Connecting a device in a comfortable, repeatable, yet flexible way can be challenging depending on individual use cases. Devices may differ in area or height and contact pads may be small, large, or irregularly placed. Chucks or sample holders are sometimes used to ease the connection but may result in delays should the layout be changed during a research project. The thermal stage uses modular probes to connect to any type or size device. The 3D printed probes have magnets on the bottom and are placed on magnetic plates to ensure firm placement. Precision screws are used to carefully lower the spring-loaded contacts onto the device to avoid scratching the contact pads with too much force. The magnetic plates are fixed using several screws and can be moved or removed altogether when using large device or devices with large sealing material. Each probe has 2 BNC connectors, one for forcing current, the other for sensing voltage. This so-called 4-wire sensing is essential for precise measurements as it eliminates any voltage drops from cable resistance and capacitance. The probe connection passes through the stage using a BNC pass-through to the cube. The pass-through is added to better remove any background light when placing a cover over the stage.

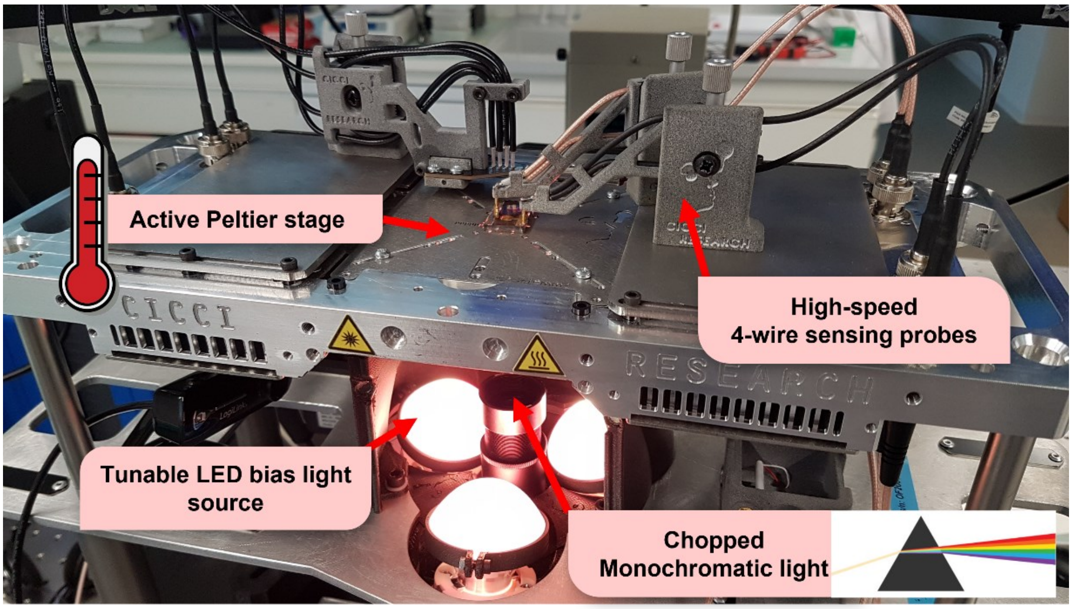

Figure 4 – The thermal stage with a back-contact device connected upside down. A monochromatic light beam enters from the bottom with tunable bias light source around it.

Devices are placed onto a copper heat plate containing 2 Peltier elements, driven by a PID controlled temperature controller mounted on a Eurocard formatted board. The Peltier elements allow for flexible temperature control as they have the capability of both heating and cooling. Practically, the temperature range is -5 °C to 90 °C, although care must be taken when reaching sub ambient as condensation will occur. Peltier elements are shaped like a plate and work by displacing heat energy from one side to the other. They work more efficiently when the temperature difference is greater[14]. Fans are therefore placed under the stage to keep the heat sink temperature around ambient temperatures.

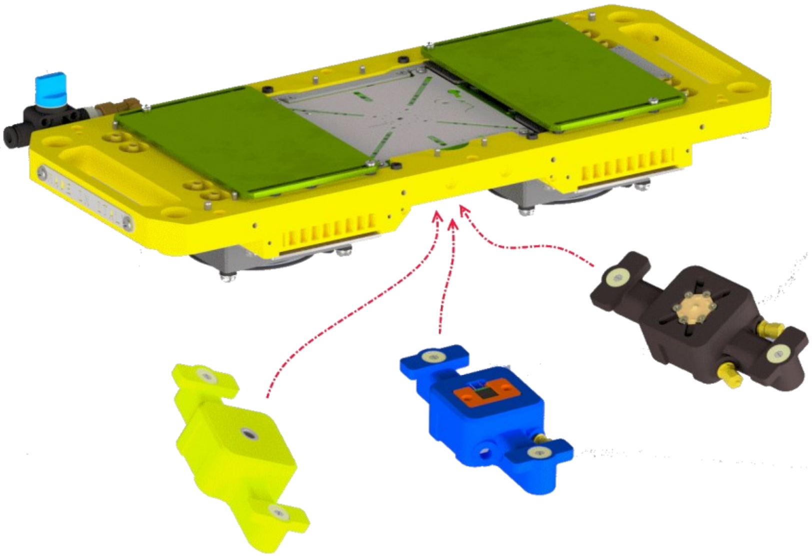

Figure 5 – Different module can be attached to the thermal stage using toolless magnetic slots.

The copper plate onto which the devices are placed, has a 1 cm² circular aperture. Magnetic modules are placed under the stage depending on the type of test to be performed as shown in Figure 5.

Examples are a light source for JV tests; A fibre directing monochromatic light from a monochromator for EQE tests; A spectrometer sensor for luminescence tests and many more. The modules are made from a standardized 3D printed plastic design and can easily be replaced or upgraded on demand. The copper plate contains screws holes to allow shadowing masks to be placed onto it.

All cables from the stage go the acquisition unit, using standard BNC, DB9 or DB25 cables. The acquisition unit has a standard 19” form factor with the height being dependent on the number of modules installed. A standard acquisition unit has four parts:

1. Eurocard formatted plug-and-play modules
2. Power supplies
3. Digitizers
4. PC with Windows

The top front of the system is filled with Eurocard style boards for each installed module. The temperature controller, LED driver, BNC connector panes and spectrometers are examples of plug-and-play modules. Some are self-contained and connect to the Windows based computer via USB. Others require an additional connection to the digitizer boards on the back of the system. All modules connect to a backplane which distributes power and electrical signal to their appropriate receivers. The back of the system contains the power supplies needed to run the system, again in Eurocard format. Replacements can therefore be easily performed without technical knowledge of the system. The control software is written in National Instruments® LabVIEW™ with some data post-processing done in Python, everything running on a standard Windows PC.

The base system has a high-performance source meter unit (SMU) to handle steady state tests and low-frequency transient tests using a 100 kS/s acquisition speed. The SMU can supply currents up to 3A and a resolution up to 100 fA, with a voltage range of up to ±60V and a resolution of up to 100 nV. Higher speeds can be obtained by adding a high-speed oscilloscope having a sampling rate of up to 100 MS/s and voltage ranges of up to ±10 V with a resolution of up to ±1 mV. Current is measured as the voltage drop over a 50 Ω internal resistance. Higher precision can be obtained by adding an additional current amplifier, boosting the current resolution by a factor of 100, 1000 or 10,000. The oscilloscope is paired with a high-speed arbitrary waveform generator with a sampling rate of 100 MS/s and a voltage range of ±12 V.

The software suite is designed to be modular and be compatible with certain 3rd party equipment. Many equipment suppliers provide a programming interface to control them. 3rd party equipment can be fully integrated on-demand into the software suite. Examples include Keithley source meter units, Stellarnet and Avantes spectrometers and Newport monochromators.

2.2 Photo-Stimulation: A LED-Based Approach

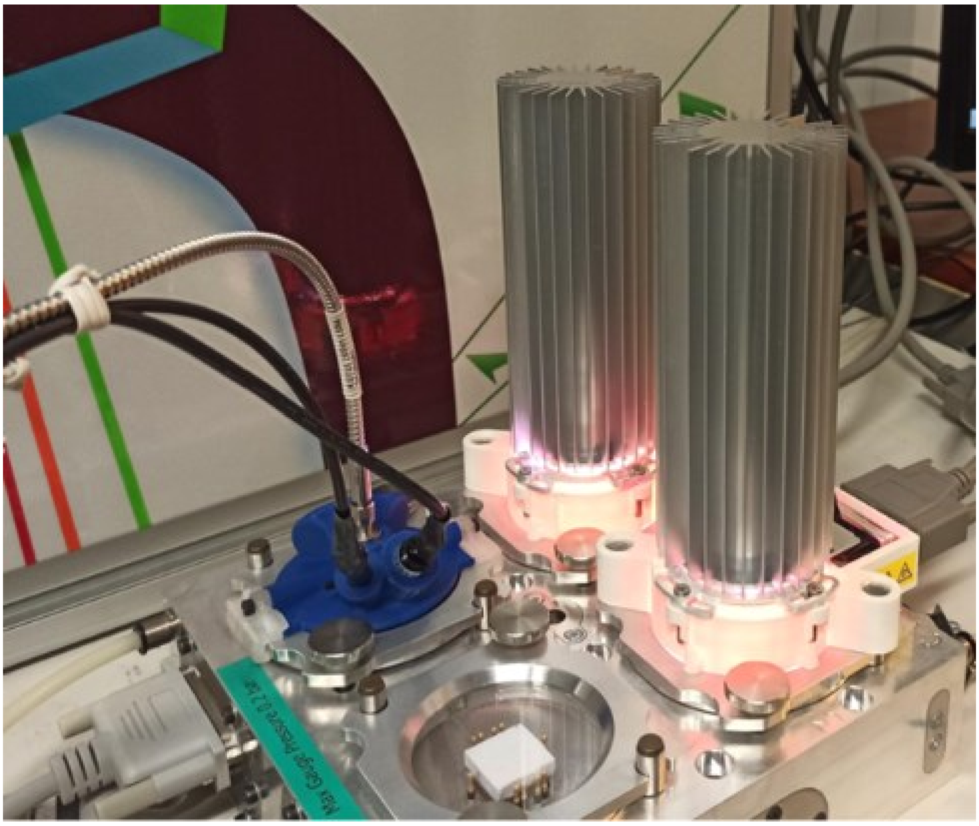

Figure 6 – A 4 compartment environmental chamber with devices illuminated by a tuneable high-intensity LED based light source. The leftmost compartment has a spectrometer module attached for luminescence measurements.

The spectral shape of a light source heavily influences the performance of solar cells and LSCs. Having access to the flexibility of a tuneable light source has become apparent during the development of the system. Traditional, single-lamp based sources such as a xenon arc lamp are often used due to their stability, high intensity, broad spectrum, and similarity to the AM1.5G solar spectrum. Disadvantages are low lifetime (<1000 hours) and non-variable output intensity (light cycling possible, but expensive due to stressing of the lamp when cycling). Moreover, a xenon or carbon-arc based light source requires a large setup and optics, limiting the portability of the system. Their tuneablity is limited through the use of a monochromator, lowering the intensity significantly.

The precision of a monochromator does not necessarily outweigh its costs and usability. LED technology has advanced far enough to make it a good contender for use as a solar simulator. LEDs have the advantage of long lifetimes (>1000 hours), higher efficiency and are less bulky allowing for easier and cheaper setups. LEDs have localized emission spectra with FWHM of <100 nm. This requires a light soaker to have multiple LEDs working together to obtain similarity to the solar spectrum. The ASTM E927-19 standard categorizes light sources by classifing them into class A+, A, B or C depending on the mismatch to a reference spectrum. The total irradiance of the light source between each band of 100 nm (e.g. 300-400 nm) should not differ more than 12.5%, 25%, 40%, 60%, from the reference spectrum, respectively. The IEC 60904-9:2020 improves on this standard by extending the required wavelength range from 300-1100 nm to 300-1200 nm. Moreover, each band is divided such that each band has the same total intensity instead of having fixed band widths. LEDs have the advantage of tuning the intensity of each individual LED allowing them to adapt to different types of classifications and reference spectra.

The solar spectrum according to the AM1.5G standard spans a range of wavelengths from ultraviolet (UV), which is less than 400 nm, to the far-infrared, extending beyond 800 nm. The spectral irradiance of this range is measured in watts per square meter (W/m²), and direct sunlight has an irradiance value of approximately 1000 W/m². Notably, a substantial fraction of this spectrum is in the infrared region, which is generally not absorbable by conventional photovoltaic technologies. Additionally, this infrared fraction falls outside the scope of human visual sensitivity. In contexts where human visual perception is a factor, light intensity is quantified using illuminance, expressed in units of lux (lm/m²). The equation for illuminance can be represented as:

$$Illuminance = k \int_{390\ nm}^{830\ nm} P(\lambda)\, E(\lambda)\, d\lambda$$

With k defined as 683 lumens/Watt, $P(\lambda)$ irradiance of the light source and $E(\lambda)$ the photopic luminosity function luminous efficacy function (Figure 7)[15].

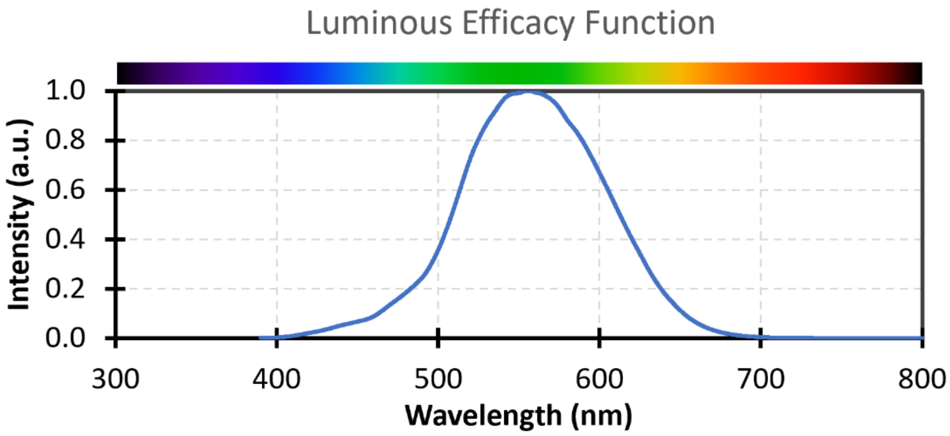

Figure 7 - Luminous efficacy function used to convert irradiance to illuminance.

From the definition of illuminance, any change in illuminance can be directly observed by humans. While illuminance serves as a convenient metric for assessing the brightness of light in human-centric contexts, it is not suitable for determining the efficiency of photovoltaic systems. This limitation arises because a direct conversion from illuminance to irradiance is unfeasible without information regarding the spectral composition of the light source. Therefore, for applications involving the performance evaluation of photovoltaic devices, irradiance should always be the provided for light intensity,[16].

2.2.1 Localized light stressing

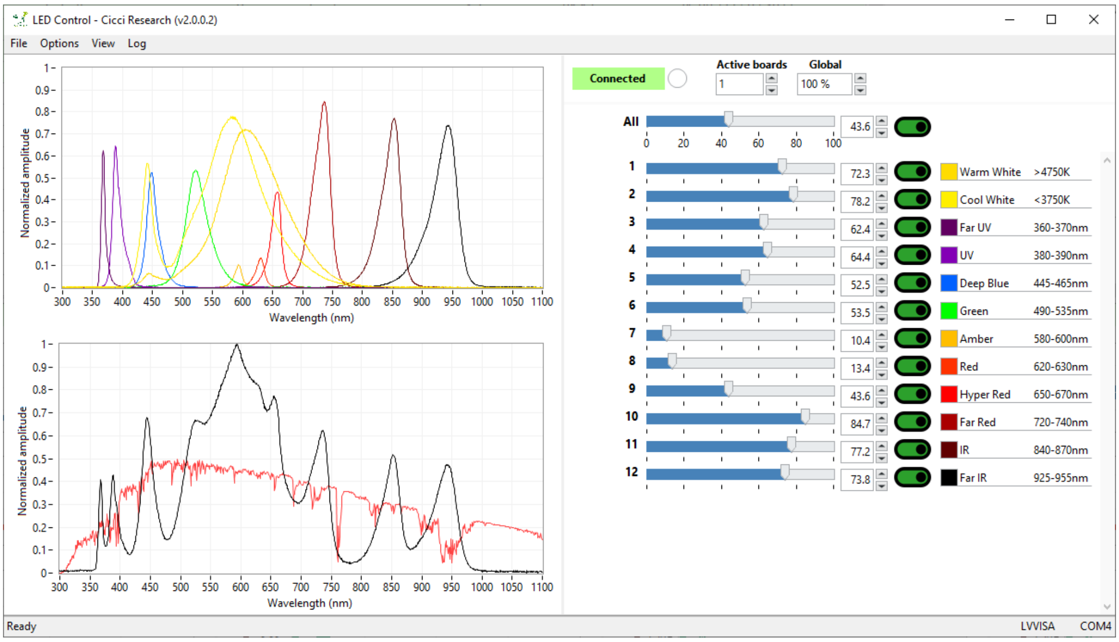

Active boards: 1

Global: 100 %

	Value		
All	43.6		
1	72.3	Warm White	>4750K
2	78.2	Cool White	<3750K
3	62.4	Far UV	360-370nm
4	64.4	UV	380-390nm
5	52.5	Deep Blue	445-465nm
6	53.5	Green	490-535nm
7	10.4	Amber	580-600nm
8	13.4	Red	620-630nm
9	43.6	Hyper Red	650-670nm
10	84.7	Far Red	720-740nm
11	77.2	IR	840-870nm
12	73.8	Far IR	925-955nm

Figure 8 – Control software for the Multi-LED light source showing a preset for the AM1.5G spectrum. Note: the spectrum on the left is for cosmetic purposes only and does not represent the actual power output of the LEDs.

For use on the thermal stage, a bulky system is unnecessary. A small, concentrated light source is sufficient to illuminate a single devices. For this purpose, the MultiLED was designed, having 12 individually controllable LEDs covering the entire visible spectrum in addition to the infrared spectrum up to 1000 nm, sufficienct for he research done with the system as it is focussed on measurements of devices with a response between 300 nm and 1000 nm. LEDs, however, have a relatively narrow peak, necessitating the need for multiple LEDs to cover the desired spectrum. Figure 8 shows the software interface to control 12 individual LEDs at different wavelength, highlighting the flexibility of this approach with Figure 9 showing the capability to reach the AM1.5G spectrum.

The LEDs are controlled by a digital microcontroller with a 12-bit ADC for 4096 levels of control. The PWM output signal passes through a stabilization filter and finally to a galvanostatic controller to control the LEDs in current instead of voltage for better stability. Each LED has its own separate circuit for fully independent control. The LED driver board is integrated into a Eurocard format for easy plug-and-play into the system backplane. The modular design also allows the LED driver board to be used as a stand-alone in smaller format if just a light source is required. The communication signal from the PC is converted to an RS485 signal. This fast and robust signal passes to the backplane into all connected LED driver boards. As many boards as can fit into the system can be controlled in the way, each fully independent from each other.

Finally, the LED can be mounted onto a standard holder for use with the thermal stage or, as shown in Figure 6 as localized light soakers for use in long-term environmentally controlled stability tests.

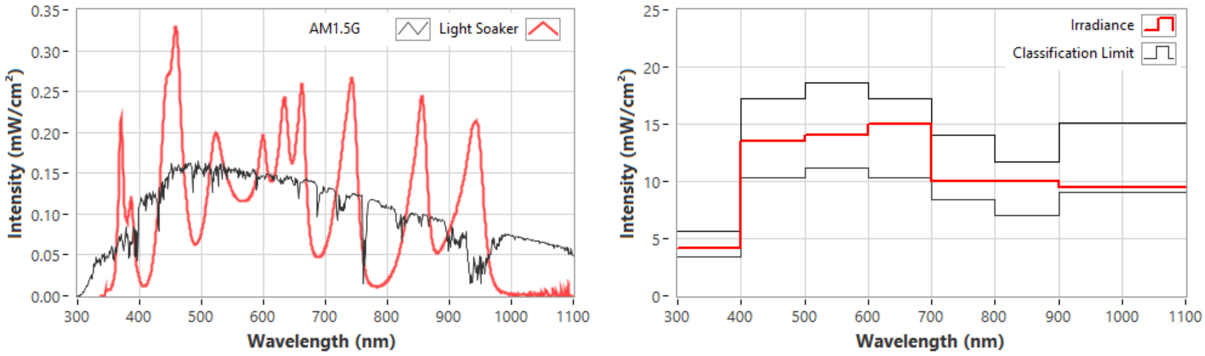

Figure 9 – Left: Spectral shape of the MultiLED showing a comparison to the AM1.5G spectrum. Right: Classification graph according to the ASTM E927-19 standard

2.2.2 96-Multiwell

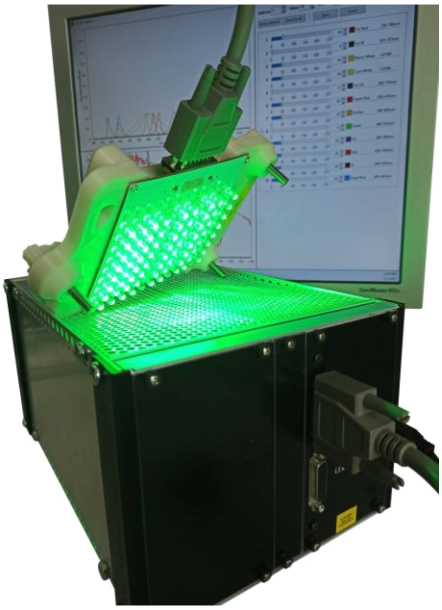

Figure 10 – Setup for a 96 multiwell with green monochromatic LEDs.

The framework used for MultiLED allows us to adapt the LED format during a collaboration with the University of Turin in the investigation of biological dyes for use in biomedical applications. The absorbance dynamics of biopolymethine dyes[17] and squaraine dyes[18] as effective photosensitizers for photodynamic therapy were investigated. NIR fluorescent heptamethine cyanine, showing effective in the field of cancer treatment was researched. Their main problem is solubility and stability, which was attempted to be resolved with the use of Solid Lipid Nanoparticles (SLN) and the nanoencapsulation of brominated squaraine, respectively. Using 96 LEDs configured in 12 controllable arrays of 8 LEDs driven by the same system as the MultiLED many cancer cell lines could be measured fast and cheap. The LED wavelength would be customized based on the absorption spectra of the dyes. They were illuminated at 8 mW/cm² for 24, 48 and 72 hours to show the effect of light stressing on the dyes and revealed improvements in their photoactive properties. This demonstration highlights the simplicity of the system that allowed for a quick adaptation to the requirements of the experiment.

2.2.3 Large area light soaking

Figure 11 – Large area LED-based light soaker. The control software for MPP tracking is shown next to it.

For larger devices, a different approach is needed as the MultiLED is not powerful enough to illuminate a large area at 1 sun intensity. With the large light soaker, multiple arrays of LEDs are placed on a plane with reflecting wall around it to homogenize the light as much as possible. A total internal working area of 30x30 cm is realized. As it is intended for 1 sun illumination, the system doesn't contain the fine independent control of the MultiLED. Instead, the LEDs are grouped into 4 lines each with 1 or more LED types that can be set in intensity (Table 1). The reason for this choice was to simplify the electronics while still giving the user the option to remove any unnecessary light sources such as the damaging UV radiation. Often for xenon or metal-halide light sources, UV filters are added to improve the lifetime of the devices. This LED based solution doesn't require any filters as any of the 4 groups can be simply turned off.

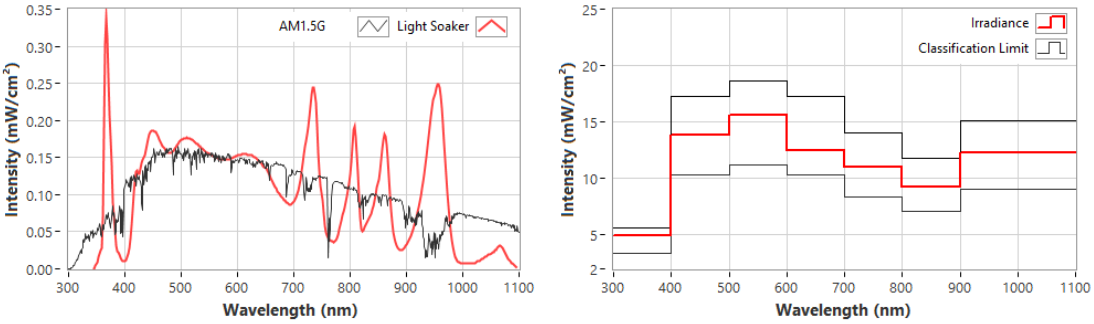

Figure 12 – Left: Spectral shape of the light soaker showing a comparison to the AM1.5G spectrum. Right: Classification graph according to the ASTM E927-19 standard.

Figure 12 (left) shows the spectral shape of the light soaker at 1 sun intensity. The sharp peaks of the LEDs result in some wavelengths being overrepresented compared to light sources based on a Xenon-arc or incandescent source. The widely used ASTM E927-19 classification standard requires the integrated irradiance to be withing spec at each band. The light soaker falls within Class A (i.e. within 25% in each band) shown in Figure 12 (right).

Line	Wavelength peak (nm)
UV	365
VIS	Visible
IR	730
	850
	940
FIR	800
	1050

Table 1 – List of LED types in the large area light soaker

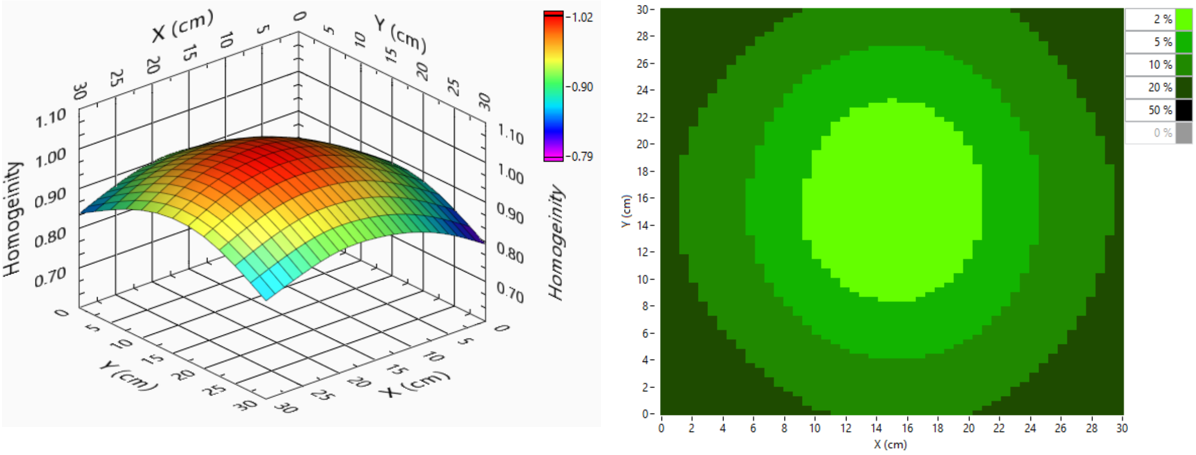

Figure 13 – Left: 3D homogeneity map of the light soaker. Right: Top view of the same graph showing the borders at which the light soaker is classified for Class A, B and C of the ASTM E927-19 standard.

The LEDs are placed across the entire top area of the light soaker. Despite the even distribution of the LEDs, the working plane doesn't show a homogeneously lit area. Figure 13 shows the relative homogeneity of the light at the working plane. The LEDs have a cone-like diverging light output. Most cones overlap in the middle of the working plane resulting in the highest intensity. Reflections from the walls help to even out the light output but still some inhomogeneity is observed. Practically, staying within a circle of diameter 18 cm places the light soaker in Class B of the ASTM E927-19 homogeneity classification as shown by Figure 13. The homogeneity can be improved by replacing the aluminium wall by more reflecting mirrors to better spread the light.

The large, illuminated area requires much more power than the previously described MultiLED, consuming around 1kW at 1 sun intensity with all LEDs on. For use in open-air, a large heat sink with multiple fans is added to stabilize the temperature of the LEDs. The system may also be used inside a glovebox to measure devices in an inert environment without the need for environmental chambers. Cooling 1 kW of LED heat in a glovebox presents several challenges. First, the confinement of the glovebox restricts airflow and limits the space available for cooling apparatus, creating an inherently difficult environment for heat dissipation. In such a confined space, a water-cooling system is preferred. This solution is more complex as it requires careful planning to avoid condensation and potential contamination, especially if the glovebox is used for sensitive materials or reactions. Ensuring that the cooling system is completely sealed is vital, as leaks could have detrimental effects on both the experiments within the glovebox and the equipment itself. Water cooled to 15 °C by an external chiller flows through tubes into the glovebox. They are insulated using a silicon resin paste to avoid any air leaks. A copper heat pipe passes through the heat sink at the LEDs to remove excess heat.

3 STEADY-STATE ELECTRO-OPTICAL TESTS

In this chapter the general working principles of a solar cell will be explained and how the system can be used to characterize the physical processes of three difference scenarios. First, advanced steady-state tests on bio inspired hybrid organic-inorganic dye-sensitized solar cells (DSSCs) fully characterize the workings of a device. These tests will be extended to the transient behaviour of perovskite devices in chapter 4. Second, the efficiency of luminescent solar concentrators based on bio polymers will be discussed. After which these tests will be used as a base to combine absorbance measurements with electrical stimuli for neuromorphic devices.

3.1 Photovoltaic Working Principle

While silicon is the most-used commercial type of solar panel, research is being on many different emerging types of solar cells, the most promising of which are perovskites (PSC)[19,20], DSSC[21,22] and organic (OPV)[23,24] solar cells. Although the specific working principle differ from material to material, the basic principle is the same: a photon causes a charge carrier to be excited after which it can be extracted by an external circuit[25].

A basic solar cell typically comprises a p-n junction, where one side (p-type) has an excess of holes (positively charged), and the other side (n-type) has an excess of electrons (negatively charged). When these two materials come into contact, some electrons from the n-type region recombine with holes in the p-type region. This creates a depletion zone or space-charge region, where mobile carriers are absent. This region possesses an electric field that opposes the further movement of carriers, thus reaching an equilibrium state.

Solar cells having a p-n junction exhibit diode-like behaviour and can therefore be described by the Shockley diode equation[26,27]:

$$J = J_0 \cdot e^{\frac{qV}{nk_BT}}$$

With J_0 the dark current, q the electron charge, n the ideality or quality factor, k_B the Boltzmann constant and T the temperature

Under illumination, photons generate additional electron-hole pairs in the semiconductor. If the energy (E) of these photons (calculated by the equation $E = h\nu$, where h is Planck's constant and ν is the frequency of the photon) exceeds the bandgap energy of the material, it can excite an electron from the valence band (HOMO) to the conduction band (LUMO) of the material. This transition results in the creation of an electron-hole pair or exciton. These excitons, if generated near or swept through the depletion region, are separated by the built-in electric field. This photogenerated current (often called the photocurrent) is in the opposite direction to the dark current described by the Shockley diode equation. Thus, for a solar cell under illumination, the equation becomes:

$$J_{tot} = -J_{abs} + J_0 \cdot e^{\frac{qV}{nk_BT}}$$

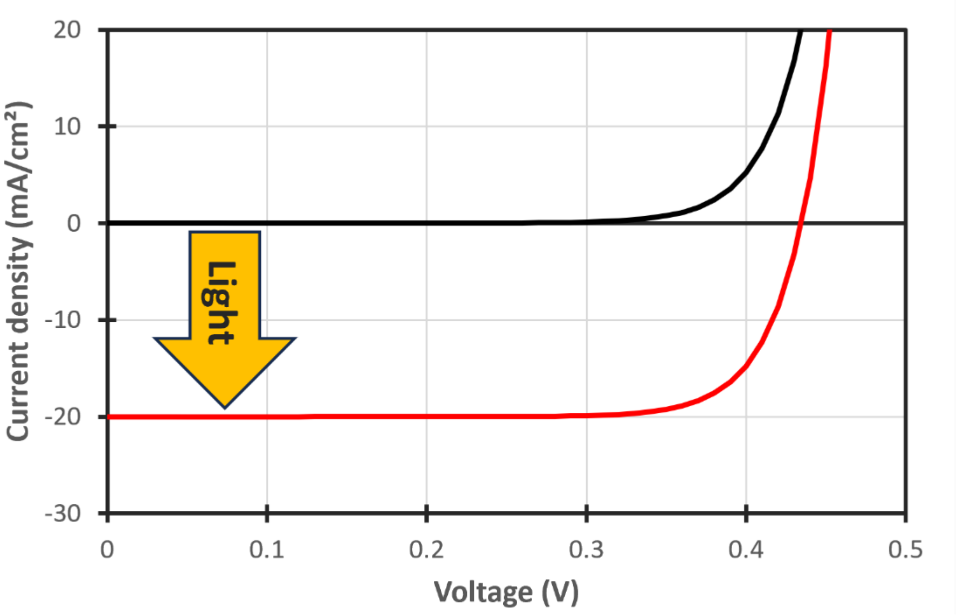

Figure 14 – Plot of the Shockley diode equation and the effect light has on it.

The Fermi level (E_F) in semiconductors represents the energy level at which the probability of an electronic state being occupied is 50% at absolute zero temperature ($T = 0\ K$). For intrinsic semiconductors, the Fermi level is located midway between the valence band (E_V) and the conduction band (E_C).

In the absence of external energy (like light), the Fermi level is continuous across the p-n junction. However, note that this doesn't mean that the energy bands are continuous. The E_C and E_V of both regions are shifted due to the built-in potential of the junction. The Fermi level remains constant to ensure thermodynamic equilibrium.

When the solar cell is illuminated, photons with energy greater than the bandgap of the semiconductor can generate electron-hole pairs by moving electrons from the valence band to the conduction band. These carriers are then separated by the electric field of the depletion zone. Electrons in the p-type region are driven towards the n-type region. Holes in the n-type region are driven towards the p-type region.

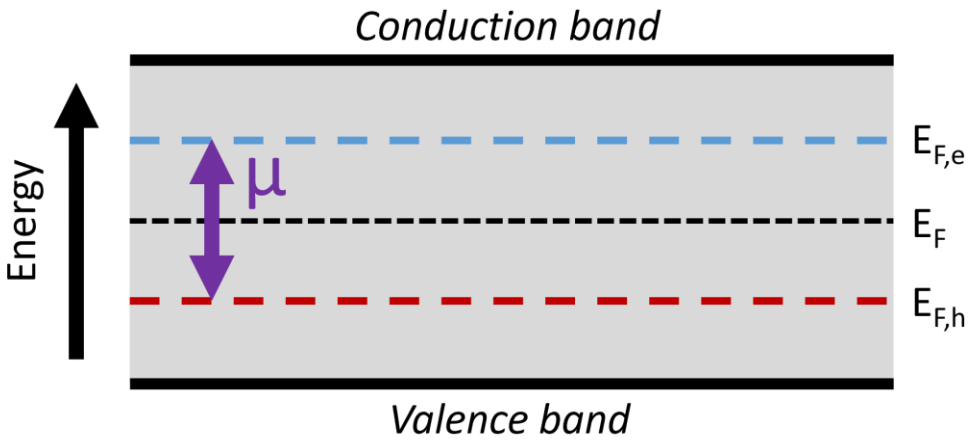

Figure 15 – Visualization of the splitting of the fermi level due to the migration and splitting of charge carriers in a p-n junction.

Under illumination, the concept of a single Fermi level becomes inadequate, and instead, two quasi-Fermi levels are used to describe the system. Because of this photogenerated carrier separation, the electron concentration in the n-type region increases, raising its quasi-Fermi level for electrons ($E_{F,e}$) while the hole concentration in the p-type region increases, lowering its quasi-Fermi level for holes ($E_{F,h}$). The separation between these quasi-Fermi levels under illumination represents the photovoltage (μ). The larger the splitting, the higher the potential difference developed, and consequently, the higher the open-circuit voltage (Voc) of the solar cell:

$$qV_{OC} \leq E_{f,e} - E_{f,h}$$

To generate a current, the excited charge carriers must be collected, to prevent them from immediately recombining. Once the charges reach the contacts, they flow through an external circuit, providing electrical power. This movement of charges constitutes the photocurrent. The direction of the current is such that electrons flow from the n-type contact to the p-type contact in the external circuit. To improve the charge extraction, especially organic photovoltaic cells (OPVs) and perovskite solar cells often have hole transport layers (HTLs) and electron transport layers (ETLs). These layers have their HOMO and LUMO levels optimized for high hole and electron mobility, respectively. This has the added benefit of blocking the opposite charge carrier.

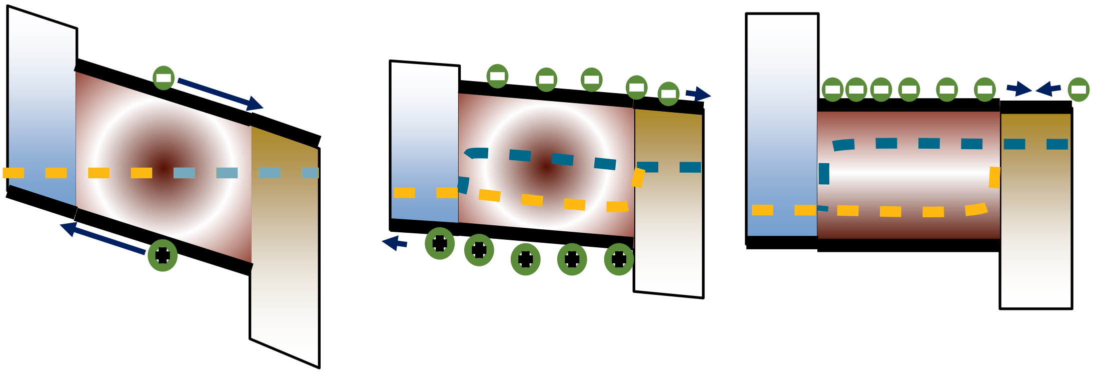

Figure 16 – Effects on the fermi level splitting when adding a bias voltage to the contact pads.

When the contacts are placed in short circuit the two quasi-fermi level equalize generating the maximum possible photocurrent (Jsc), but no useful work is provided (Figure 16). Adding a potential difference shifts the energy levels of the contacts resulting in an increasing splitting of the fermi level. The splitting can increase indefinitely, passing through the devices Voc and increasing exponentially further. Somewhere between the Jsc and Voc lies the device's optimum called the maximum power point providing the maximum amount of work to an externa load.

3.1.1 Dye-Sensitized Solar Cells

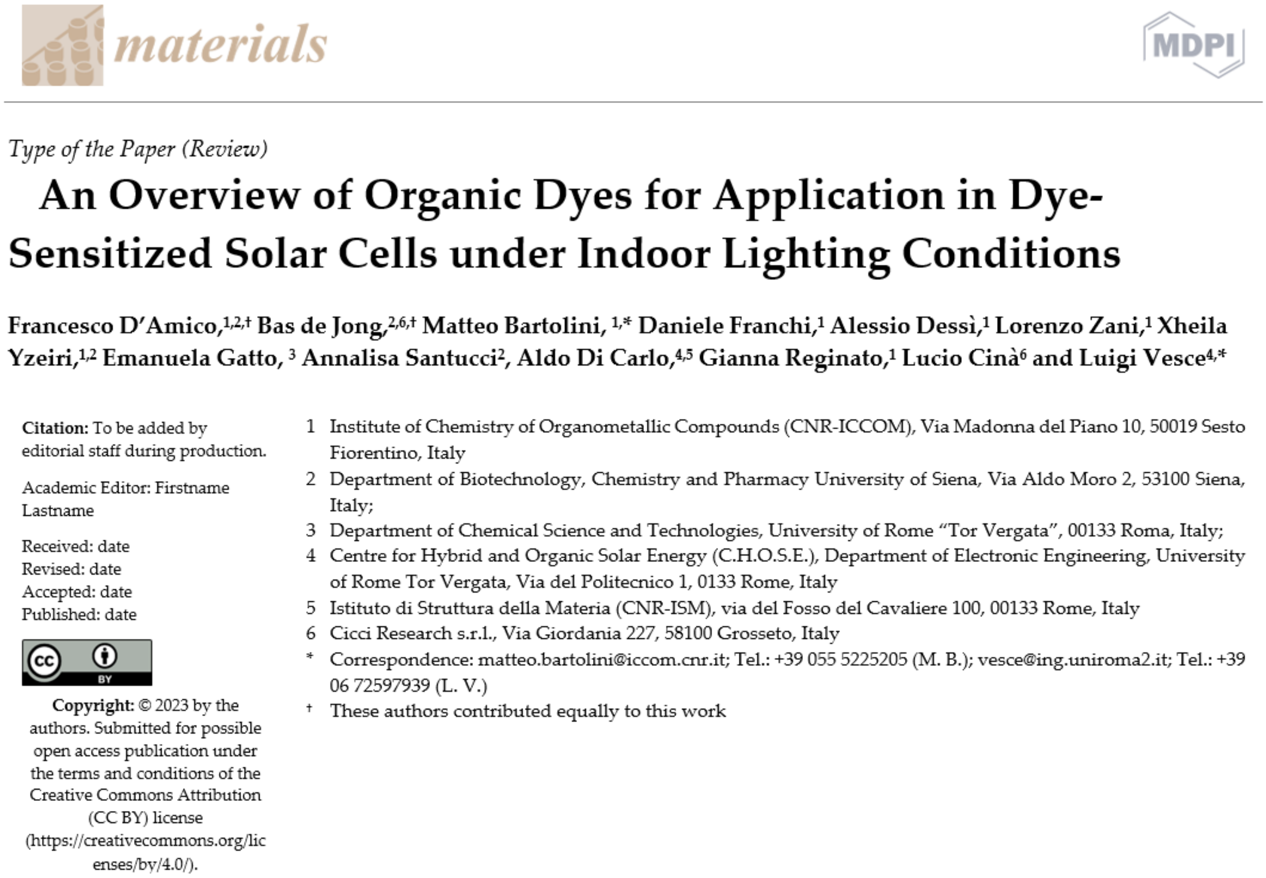

materials

Type of the Paper (Review)

An Overview of Organic Dyes for Application in Dye-Sensitized Solar Cells under Indoor Lighting Conditions

Francesco D'Amico,[1,2,†] Bas de Jong,[2,6,†] Matteo Bartolini, [1,*] Daniele Franchi,[1] Alessio Dessì,[1] Lorenzo Zani,[1] Xheila Yzeiri,[1,2] Emanuela Gatto, [3] Annalisa Santucci[2], Aldo Di Carlo,[4,5] Gianna Reginato,[1] Lucio Cinà[6] and Luigi Vesce[4,*]

1 Institute of Chemistry of Organometallic Compounds (CNR-ICCOM), Via Madonna del Piano 10, 50019 Sesto Fiorentino, Italy
2 Department of Biotechnology, Chemistry and Pharmacy University of Siena, Via Aldo Moro 2, 53100 Siena, Italy;
3 Department of Chemical Science and Technologies, University of Rome "Tor Vergata", 00133 Roma, Italy;
4 Centre for Hybrid and Organic Solar Energy (C.H.O.S.E.), Department of Electronic Engineering, University of Rome Tor Vergata, Via del Politecnico 1, 0133 Rome, Italy
5 Istituto di Struttura della Materia (CNR-ISM), via del Fosso del Cavaliere 100, 00133 Rome, Italy
6 Cicci Research s.r.l., Via Giordania 227, 58100 Grosseto, Italy
* Correspondence: matteo.bartolini@iccom.cnr.it; Tel.: +39 055 5225205 (M. B.); vesce@ing.uniroma2.it; Tel.: +39 06 72597939 (L. V.)
† These authors contributed equally to this work

Citation: To be added by editorial staff during production.

Academic Editor: Firstname Lastname

Received: date
Revised: date
Accepted: date
Published: date

A collaboration for the characterization of Dye-Sensitized Solar Cell (DSSC) devices in indoor lighting conditions was done with CNR-ICCOM and the university of Rome[1]. Solar cells are often characterized assuming sunlight as the illumination source. Indoor lighting is fundamentally different, both in intensity and its spectrum. Many protocols that are applied in standard conditions cannot be directly applied when working in indoor conditions. Due to the intensity affecting the Voc, the fill factor and in turn the efficiency of a device is also affected[28]. As indoor lighting only emits in the visible range, any solar cell that would absorb photons with energies outside this range won't generate current in this range. DSSC's are a good candidate for indoor applications due their bandgap being at 800 nm, around the cut-off for the visible range[29].

---

[1] Paper under review

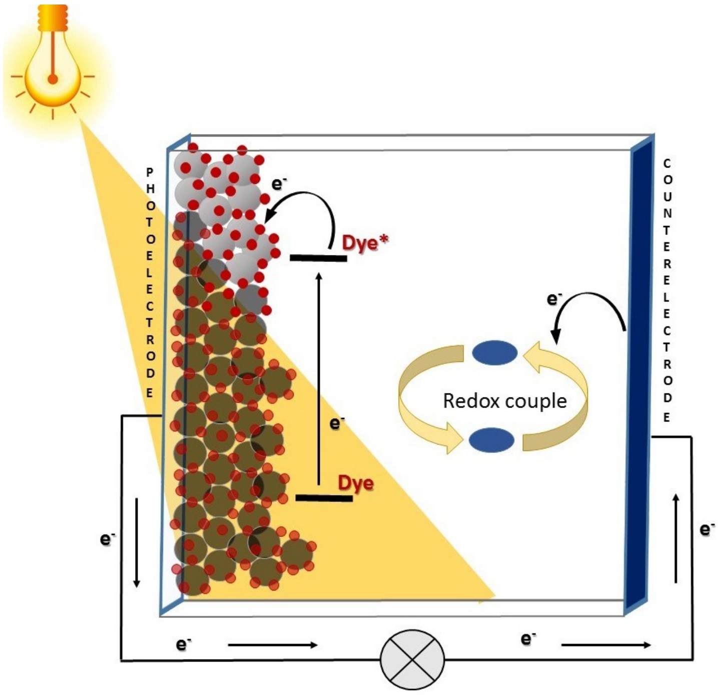

Figure 17 – Working mechanism of a DSSC.

Although the high-level working function of DSSCs is the same as describe in section *3.1 - Photovoltaic Working Principle*, their origin is quite different, coming from the natural process of photosynthesis through the use of dye molecules, semiconductors, and electrolytes[21]. The synergy between these components allows DSSCs to convert sunlight into electrical energy in a unique way. Instead of a semiconductor p-n junction, they comprise of an organic or metal-organic dye molecule absorbed onto a semiconductor material, typically TiO_2 nanoparticles. When they are hit by photons, they move to an excited state and lose an electron, which moves through the mesoporous semiconductor material from the photo electrode to the counter electrode. The lost electron of the dye is regenerated by the electrolyte which in turn moves to an oxidized state (typically from I^- to I^{3-}). At the counter electrode, the electrolyte regains electrons and is reduced back to its original state (I^{3-} to I^-) complete the cycle (Figure 17).

While DSSCs are known for their relatively lower efficiency compared to silicon-based and perovskite solar cells[6], they hold promise for applications such as indoor environments where flexibility, transparency, and lower cost are more important than high efficiency[30]. The main challenges include improving the long-term stability, increasing the efficiency, and developing solid-state or non-volatile electrolytes.

A growing concern is about the sustainability of photovoltaic devices, as the increase in efficiency comes paired with more and more exotic materials[7]. Instead, the search for more biological, sustainable, and low-cost materials is growing. For indoor purposes, pigments from naturally available sources, most efficient in the visible light part of the spectrum, are a good candidate. Indeed, dyes such as anthocyanins[31], chlorophyll[32] and carotenoids[33] as well as the use of bacterial protein complexes[34] have been reported as successful materials[35].

3.1.2 The Sun JV Test

A Sun JV test, also known as the current-voltage characteristic measurement, is a fundamental technique to characterize important parameters determining the performance of solar cells and other photovoltaic devices. It provides information about the electrical behaviour and efficiency of these devices under varying conditions. The JV test involves sweeping the voltage across the device and measuring the resulting current[19]. The separation between these quasi-Fermi levels under illumination represents the photovoltage (μ). The larger the splitting, the higher the potential difference developed, and consequently, the higher the open-circuit voltage (Voc) of the solar cell. Extracting the generated charges by applying an external potential results in a current flow. In a JV test the current-voltage characteristic of the device is obtained by sweeping the potential over a range. The current is often inverted when displaying JV results, this is merely a matter of convention.

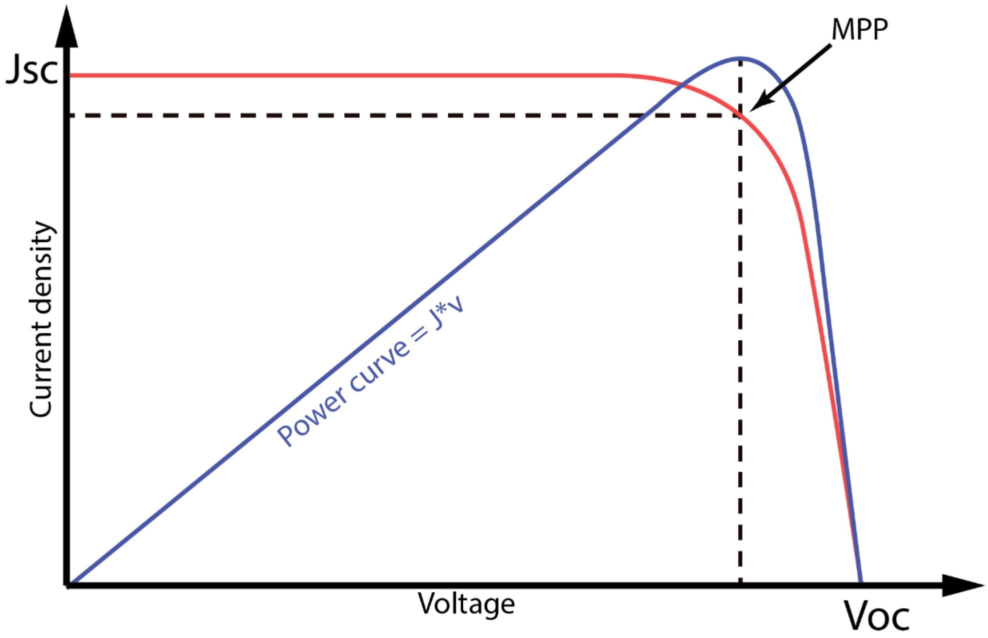

Figure 18 – Typical JV curve of a solar cell shown in red. The corresponding power curve is shown in blue.

From a typical JV characteristic of solar cells, as shown in Figure 18, four important parameters can be extracted that determine in large part the performance of the device[36].

Open-circuit voltage

The open-circuit voltage is a measure of the potential difference that builds up due to the separation of charge carriers within the device. The splitting of the fermi level is directly related to the voltage difference in the device also known as the "built-in potential" or "barrier potential". At Voc, the voltage applied across the device is in equilibrium with the barrier potential and prevents the flow of electrons and holes across the external circuit resulting in zero current flow.

Short-circuit Current

The short-circuit current (Jsc) is the maximum current that flows through a device when its terminals are short-circuited, meaning the voltage across the device is forced to zero. As there is no barrier potential, the charges are free to move within the active layer allowing for the maximum current of the device.

Efficiency

At both Voc and Jsc, the device isn't efficient at transferring its generated energy to an external load. Power is defined as P=I V, since I or V is zero in these states respectively, the useful power is zero as well. At some voltage between Voc and Jsc the device generates its maximum power output, or Maximum Power Point (MPP). During actual operation it is desirable to keep the device in this state. The efficiency of the device is highest here and can be calculated as:

$$\eta = \frac{P_{MPP}}{P_{light}}$$

Where P_{light} is the total irradiance of the incident light. The maximum power point of a device is not stable[8,37]. As a device degrades or its environment changes, the maximum power point also changes. It is desirable to keep the device at its optimal power output, so the MPP must be tracked over time. The system can perform this so-called Maximum Power Point Tracking (MPPT) in the MPPT module, an example test using outdoor lighting is shown in Figure 19. Although the All-in-One system is capable of MPPT, it is not very practical due to the length of a typical stability test, occupying the system for a long time. A multidevice system was therefore developed called the Multichannel system. As this system was designed for this purpose, the MPPT protocol will be explained in more detail in section 5.2.

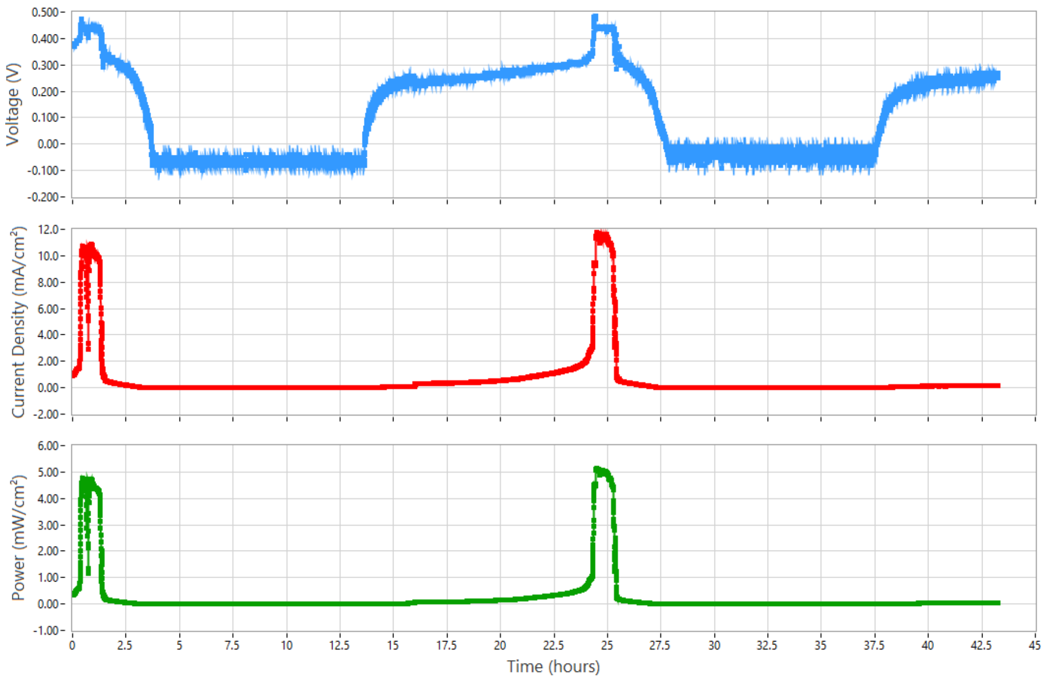

Figure 19 – Maximum power point tracking of a silicon solar cell in indoor condition with ambient lighting

Fill Factor (FF)

In an ideal device, the current remains at Jsc between 0V and Voc, after which the current becomes infinite when the potential barrier has been overcome. In reality, current losses due to charge recombination, and resistances in the device prevent this ideal scenario. The Fill Factor quantifies these losses by considering the drop-off in current during a JV sweep. It is defined as

$$FF = \frac{P_{MPP}}{V_{OC} \cdot J_{SC}}$$

And gives a direct indication of the quality of the device.

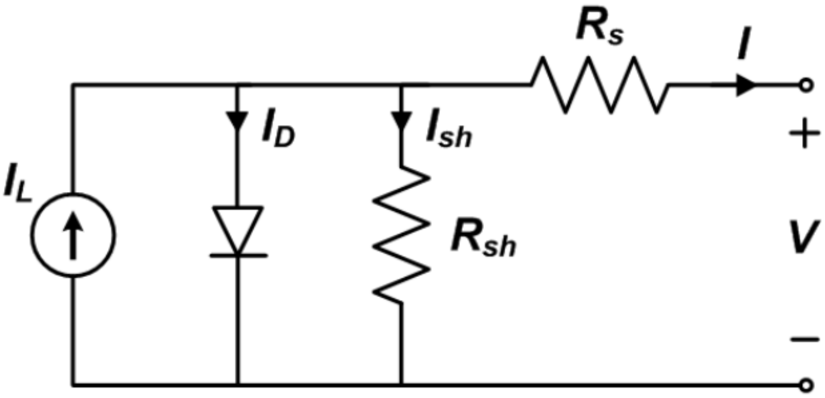

Figure 20 – One diode circuit model for solar cells.

Series and Shunt Resistances

Solar cells are often modelled using the equivalent circuit shown in

Figure 20, also known as the one diode mode[38]. The behaviour of solar cells can be adequately simulated using this circuit. I_L represents the current generation of the device.

The Shockley diode equation assumes a perfect diode with no losses. In the real world, losses occur due to imperfections in the material converting electrical energy to heat. The one-diode model summaries them into two resistances, a series and shunt resistance. Modifying the equation to include a loss term:

$$J = -J_{\text{ph}} + J_0 \cdot e^{\frac{q(V+IR_s)}{nk_BT}} + \frac{V + IR_s}{R_{sh}}$$

The series resistance (R_s) is a measure of the cumulative resistive effects that occur along the current path within the device. This includes the resistance encountered in the semiconductor material, contacts, interconnections, and any other elements in series with the photovoltaic material. At the interface between the metal contacts and the semiconductor, a certain resistance is encountered. This can be due to the imperfect nature of the contact, or the specific materials used. The resistance of the metal grid used to collect the current and any interconnections between cells in a module also contributes. The latter can be mitigated by using high conductance materials in the circuit such as gold or silver.

The shunt resistance (R_{sh}) refers to the resistance associated with the undesirable leakage pathways for the current. It provides an alternative path for the current to flow, bypassing the intended load, and thus may significantly influence the device's performance. Both R_s and R_{sh} are extracted directly from the JV curve as the slope at Voc and Jsc, respectively.

3.1.2.1 Light dependency

The intensity of the incident light affects the electrical behaviour of the solar cell. Current increases almost linearly as the efficiency of the device doesn't change much when the incident light intensity is changed[39]. Voc, however, scales with the logarithm of the intensity[28,40]

$$V_{oc} = \frac{n_{id} k_B T}{q} \ln(\phi) + b$$

where ϕ is the light intensity. Voc should exhibit a slope of $n_{id} k_B T/q$, when plotted as a function of the logarithm of light intensity. From this slope the diode ideality factor n_{id} can be extracted which represents the non-ideal behaviour of the diode in the equivalent circuit.

Many systems have a fixed luminosity light source which can only be turned on or off. In the All-in-One system, LED based light sources are used which can all be programmed to work at different light intensities. They will be explained in more detail later. The flexibility of these light sources allows the JV test to automatically perform measurements at different light intensities and extract the ideality factor.

3.1.2.2 Hysteresis

The fill factor can change depending on the direction of the JV scan. Hysteresis effects can lower the JV curve in a particular direction. Hysteresis can be quantified by the following formula[41]:

$$\text{Hysteresis Index}(HI) = \int_{SC}^{OC} \frac{\big(J_{FW}(V) - J_{RV}(V)\big)dV}{\int_{SC}^{OC} J_{RS}(V)dV}$$

where J_{FW} and J_{RV} are the current densities for forward and reverse scans, respectively.

In this test, it is assumed that the tested solar cell can be modelled according to

Figure 20. In this way, both the series resistance R_s and the shunt resistance R_{sh} can be measured. The shunt resistance is determined by the amount of current that flows through R_{sh} in

Figure 20, which should be as low as possible. A high current means a bigger voltage drop, hence the R_{sh} can be estimated from the slope of the JV curve near the short circuit current state. Like R_{sh}, the series resistance can be estimated from the slope near the open circuit voltage.

3.1.3 Quantum Efficiency

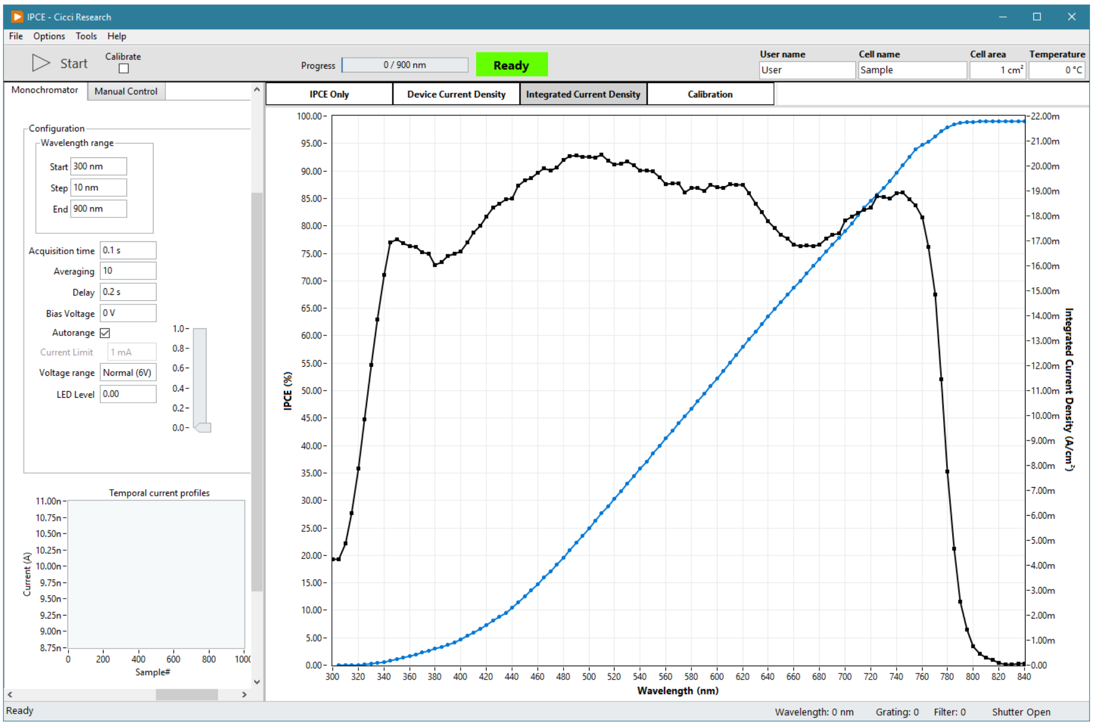

IPCE - Cicci Research

Progress 0 / 900 nm

Ready

User name User

Cell name Sample

Cell area 1 cm²

Temperature 0 °C

Start 300 nm

Step 10 nm

End 900 nm

Acquisition time 0.1 s

Averaging 10

Delay 0.2 s

Bias Voltage 0 V

Autorange ☑

Current Limit 1 mA

Voltage range Normal (6V)

LED Level 0.00

Calibrate ☐

Ready

Wavelength: 0 nm

Grating: 0

Filter: 0

Shutter Open

Figure 21 – Software interface for the IPCE module showing the efficiency at each wavelength of a typical Perovskite solar cell.

As described before, the efficiency of a solar cell is the ratio at which it can convert incident photons to charges. This efficiency is often expressed as a single number assuming a standard spectrum, usually the AM1.5G spectrum. In reality, the efficiency is wavelength dependent. To understand how the efficiency of a solar cell is affected by the spectrum of the light, its external quantum efficiency should be measured. In this test, the device is illuminated with monochromatic light at each wavelength of interest and the ratio of incident photons to generated electrons is measured.

$$\text{Quantum Efficiency (QE)} = \frac{\text{Number of Collected Electrons}}{\text{Number of Incident Photons}} \cdot 100\%$$

Solar cells have a limited range of photon energies that they can absorb (Figure 22). The lower limit is determined by the active layer's band gap. If a photon doesn't have energy to overcome it, an electron-hole pair cannot be generated resulting in zero efficiency. At higher energies, the photon has enough energy to create a charge carrier, but any excess energy is lost as heat, reducing the efficiency. Other losses can be incurred due to recombination of charges before extraction, trap states at the interlayers[42]. When considering the efficiency of the entire device, reflection, transmission, and parasitic absorption losses also affect the total efficiency. This efficiency is referred to as the External Quantum Efficiency (EQE). If the efficiency of just the active layer is considered it is referred to as the Internal Quantum Efficiency (IQE)[43]. IQE is much more difficult to achieve since detailed optical knowledge is required to remove losses from reflection and transmission (see IQE estimation with transfer matrix modelling).

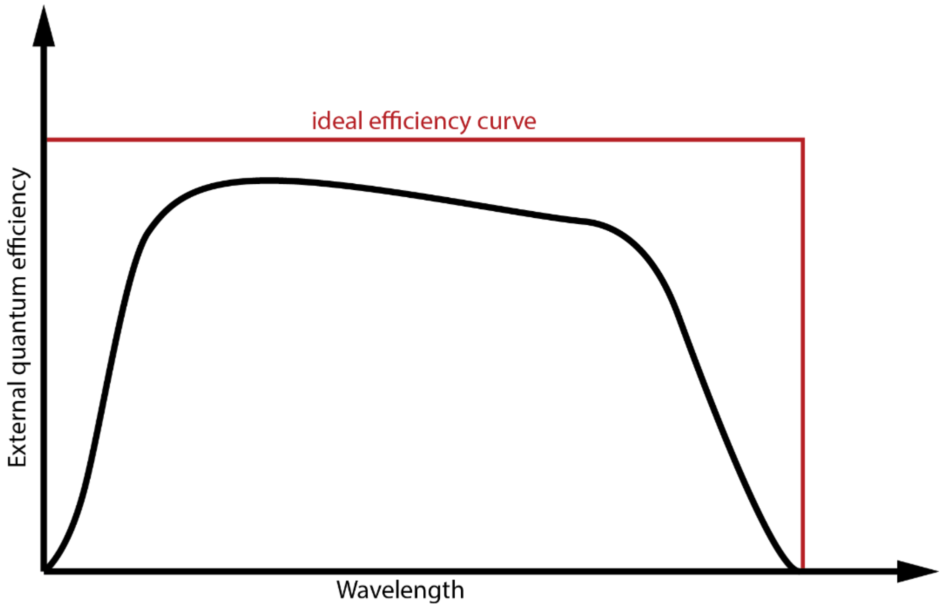

Figure 22 – Typical IPCE curve of a solar cell. Differences from the ideal curve are caused by reflection and recombination losses.

Measuring a QE requires a source meter unit to register the generated current. The device should then be illuminated by monochromatic light, one wavelength at a time. Generating a monochromatic light source is often done by placing a monochromator between the device and a broad-spectrum lamp that covers at least the band gap of the device. Xenon arc lamps are preferred due to their high intensity, broad spectrum, and similarity to the AM1.5G solar spectrum. The monochromatic light source is often not stable over time due to lamp heating, ambient fluctuations, or lamp ageing. A good IPCE measurement starts by calibrating the lamp. Although a calibrated spectroradiometer can be used, this introduces additional equipment and failure points to the system. As the measurement already requires the use of a source meter unit and contacting probes, a better way is to use a calibrated photodiode. Such a device has a known responsivity, i.e., a quantification of the current it generates at a given irradiance for each wavelength. By measuring the generated current using the same setup as used for the actual device, a precise measurement of the lamp irradiance can be obtained.

Once the incident irradiance is known, the generated current (i.e., charges) of the device is then measured and compared to the known number of photons of the incident light [44].

$$EQE(\lambda) = \frac{\text{current}(\lambda)\ /\ \text{charge of one electron}}{\text{power}(\lambda)\ /\ \text{energy of one photon}} = \frac{I(\lambda)/e}{P(\lambda)/(h\nu)} = 1240 \cdot \frac{I(\lambda)}{P(\lambda)} \cdot \frac{1}{\lambda}$$

With λ the current generated by the device, and P_λ the irradiance of the incident light, previously obtained using a calibrated photodiode.

Figure 22 shows a typical efficiency curve displaying the difference from the ideal case. The reduction of efficiency near the limits are due to surface recombination, while the reduction in the middle often occurs due to reflection of the light. Figure 23 shows an effort of reducing the number of defect

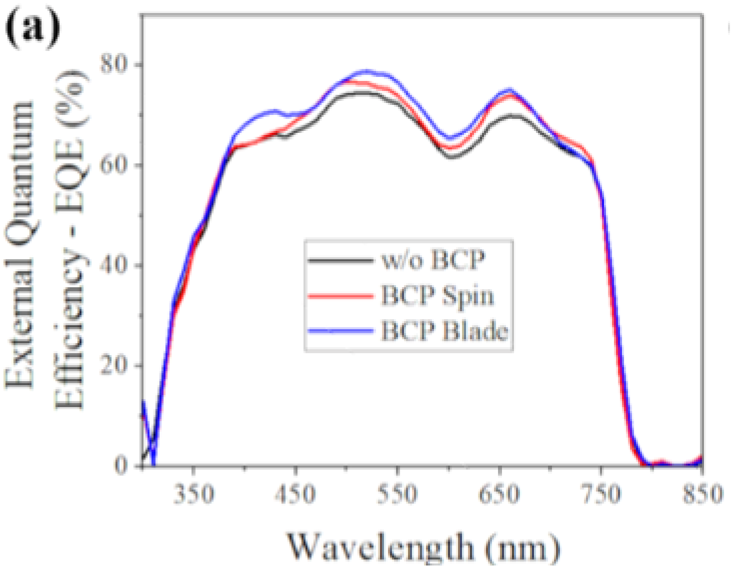

Figure 23 - Example of an IPCE curve showing efficiency increases due to the addition of a hole blocking layer (BCP)[42]

states at the devices' interlayer by the addition of a hole blocking layer (see section 0 - While steady-state characterization gives insights on the performance of a device, transient tests give an understanding of the physical behaviour leading to the performance losses in a device. Interesting parameters such as carrier lifetime and charge density can be calculated by observing the voltage and current decay of a device after it has been excited by light. Moreover, dynamic tests can help understand the behaviour in real-world changing conditions, important for grid stability and adaptability. With impedance spectroscopy showing a devices' frequency response allowing for the measurement of capacitance and inductance parameters, which can be important for AC-coupled systems and inverters. These parameters can be correlated and/or complement parameters extracted from steady state tests.

Perovskite Solar Cells for more details)[45].

By integrating the efficiency over all wavelengths, the total Jsc is calculated as[44]

$$J_{SC} = q\int_{\lambda_{min}}^{\lambda_{max}} \eta_{IPCE} \cdot \phi_{ph}^{source}(\lambda)d\lambda$$

Although this should match the Jsc obtained from a JV scan, this is often not the case [42]. One reason may be the different behaviour of generating charges at different light intensities between an EQE and JV measurement, especially when the photo-current is not linear with light intensity [46]. A bias light can be added during an EQE measurement to replicate the measurement conditions during a JV. Since the relatively weak monochromatic light is superimposed on the bias light, the small perturbation results in an approximately linear behaviour of the photo current.

When a bias light is used, the monochromatic light source is relatively weak, making it difficult to distinguish the photo-current generated by the monochromatic light from the bias photo-current. The source meter unit (SMU) of the system has a configurable current measuring range. Where a higher range, reduces the accuracy. A typical current generated by the calibrating photodiode is in the order of 1 µA, which can be measured without much noise as the SMU in its lowest range has an accuracy of 100 fA. With a bias light, the total current may be 10 mA + 1 µA. The current range must be increased several orders of magnitude, which in turn lowers the accuracy correspondingly. While the EQE can still be measured, adding a bias light results in a significant lower signal-to-noise ratio. The system mitigates this issue by adding a chopper with a configurable frequency. With the precise chopping frequency known, a software implemented lock-in amplifier is introduced to separate the periodic signal from the chopped monochromatic light from the steady bias current. For device with slow response times like DSSCs, the chopping frequency can affect the measured current, and in turn the EQE, if the period is longer than the settling time of the photo-current [47]. Sampling the current decay in the order of milliseconds will ensure a good understanding of the decay and the chopping frequency can be set accordingly.

3.1.4 Spectral mismatch

Classification Standard: ASTM E927-19 | Class A

Bin range (nm)		Intensity (mW/cm²)
300	400	4.124
400	500	13.552
500	600	14.038
600	700	14.948
700	800	10.019
800	900	9.977
900	1100	9.422

Total intensity	76.080 mW/cm²
1 sun intensity	79.706 mW/cm²
% of 1 sun	95.45 %
Gain	1

Reference Irradiance: C:\Arkeo\calibration\ASTM G-173 AM1.5G.txt

Show Mismatch Factor ☑

Spectral Mismatch	Spectral Deviation
0.9163	1.0211

Figure 24 – Software interface to calculating spectral mismatch and deviation between a LED based light source and AM1.5G

When using an artificial light source, the spectrum will never be exactly the same as the reference spectrum, e.g., the AM1.5G spectrum. Different light sources, optics and lack of absorbing atmospheric materials cause a mismatch, M, in the spectra, resulting in a different current under a simulator (I_{SIM}) and under a reference spectrum (I_{REF}).

$$I_{REF} = \frac{I_{SIM}}{M} \cdot \frac{I_{REF}^{PH}}{I_{SIM}^{PH}}$$

Where I_{REF}^{PH} and I_{SIM}^{PH} are the photocurrents of a reference photodiode. It can be used to match the generated photocurrent under both the reference and simulator irradiance. Once done, the above equation reduces to

$$I_{REF} = \frac{I_{SIM}}{M}$$

Where M is calculated as[48]

$$M = \frac{\int SR_{DUT}(\lambda) \cdot E_{SIM}(\lambda)\, d\lambda \;\; \int SR_{REF}(\lambda) \cdot E_{REF}(\lambda)\, d\lambda}{\int SR_{DUT}(\lambda) \cdot E_{REF}(\lambda)\, d\lambda \;\; \int SR_{REF}(\lambda) \cdot E_{SIM}(\lambda)\, d\lambda}$$

With $SR_{DUT}(\lambda)$ the spectral response of the cell under test, $SR_{REF}(\lambda)$ the spectral response of the reference cell, $E_{SIM}(\lambda)$ the irradiance of the incident light and $E_{REF}(\lambda)$ the irradiance of the reference spectrum. Where the spectral response of the device can readily be obtained from its EQE as

$$SR(\lambda) = \frac{q\lambda}{hc} \cdot EQE(\lambda) = \frac{\lambda}{1.2389} \cdot EQE(\lambda)$$

Note that all values can be normalized as the prefactor q/hc occurs in both the numerator and denominator, i.e., their factors cancel so that only the shapes of the curves matter. Moreover, the wavelength range they cover should cover the spectral response range of the device. M can automatically be calculated using the software interface shown in Figure 24 by providing the four spectra from the above equation. When accessed from the spectrometer software, the simulator light spectrum is shown in real-time. A tuneable MultiLED based light source can therefore be calibrated in real time to bring its spectral mismatch as close to 1 as possible.

The spectral mismatch is used to correct any current discrepancies that might occur from using a light source different from the final working conditions of the device. While for outdoor applications, the AM1.5G can be considered the working condition, indoor applications do not have such a standard and it is therefore not possible to calculate the mismatch factor as there is nothing to compare it to. Until a universal standard is agreed upon by the scientific community, comparing the performances of devices for indoor applications between researchers remains challenging[49].

3.1.5 Spectral deviation

Although the spectral mismatch gives a representation of how good the shape of the spectrum matches a reference spectrum, it may not always be possible to obtain a perfect enough match. Certain wavelengths could be missing from the simulator spectrum, for example when using LED sources. It may be sufficient to adjust the spectrum such that the generated current under the simulator produces the same current it would generate under the reference spectrum. Although this depends on the device specific EQE, requiring a flexible light source, it makes building a light source easier as a perfect match over all wavelengths is not required anymore. The so-called spectral deviation (SD) can be calculated as

$$SD = \frac{\int SR_{DUT}(\lambda) \cdot E_{SIM}(\lambda) d\lambda}{\int SR_{DUT}(\lambda) \cdot E_{REF}(\lambda) d\lambda}$$

3.1.6 IQE estimation with transfer matrix modelling

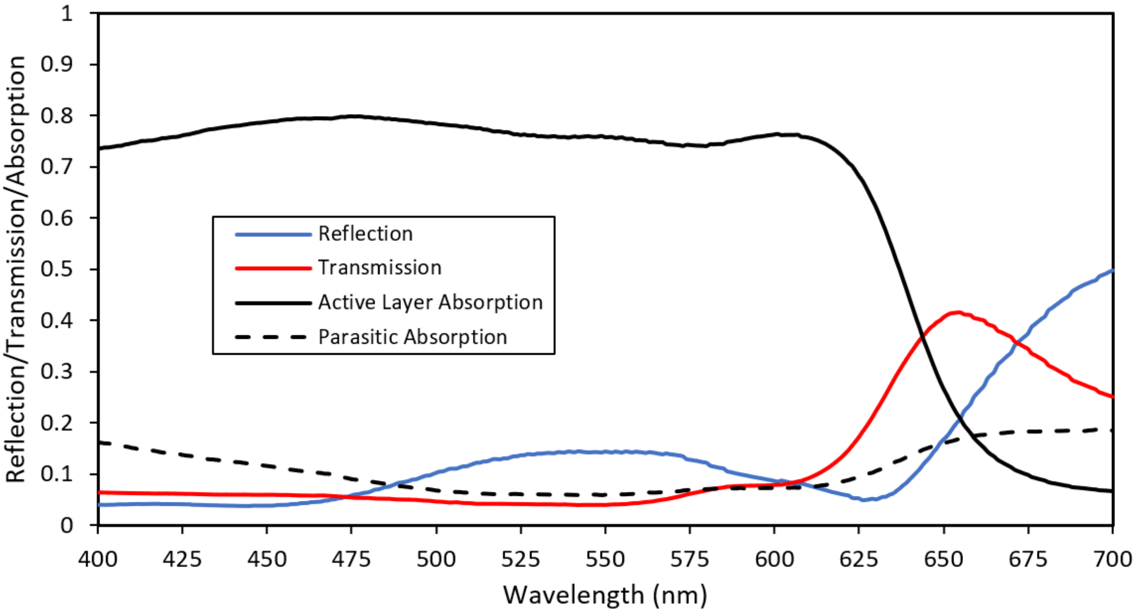

Figure 25 – Example of transfer matrix calculations on a photo voltaic device showing reflection, transmission as well as active and parasitic absorption.

The IQE of a device is difficult to measure directly as it requires knowledge about the optical properties of each material layer of the photovoltaic device. If these are known however, IQE spectra can be estimated from the directly measured EQE[50]. Solving the optical equations requires the knowledge of the complex indices of refraction of each layer: $\tilde{n} = n + i$. Values for many materials can be found in literature, however they must be used with care, as processing conditions and aging effects may influence the refractive index. For very accurate measurements of the refractive index, variable angle spectroscopic ellipsometry (VASE) may be performed. Though it has been suggested that accurate measurements may not be necessary as the error in the IQE with rough estimates is usually small[51].

With knowledge of the indices of refraction, optical properties can be calculated with the so-called transfer matrix method[52]. This method looks at the optics from the point of view of the electric field and how it interacts with the interfaces between each layer. This allows the calculation of properties such as reflection, transmission, and absorption for each individual layer, shown in Figure 25. Absorption is defined from the complex index of refraction.

$$\alpha = \frac{4\pi\kappa}{\lambda}$$

In PV devices it is convenient to separate κ into κ_{active} for absorption in the active layer and $\kappa_{\text{parasitic}}$ for absorption everywhere else. Parasitic absorption does not contribute to any useful energy and is treated as losses, like reflection and transmission[53]. As such, IQE is defined by:

$$\text{IQE} = \frac{\text{EQE}}{1 - R - T - ABS_{parasitic}}$$

Each of the values in the denominator can be modelled with the transfer matrix method, provided the indices of refraction are known.

3.2 Luminescent Solar Concentrators

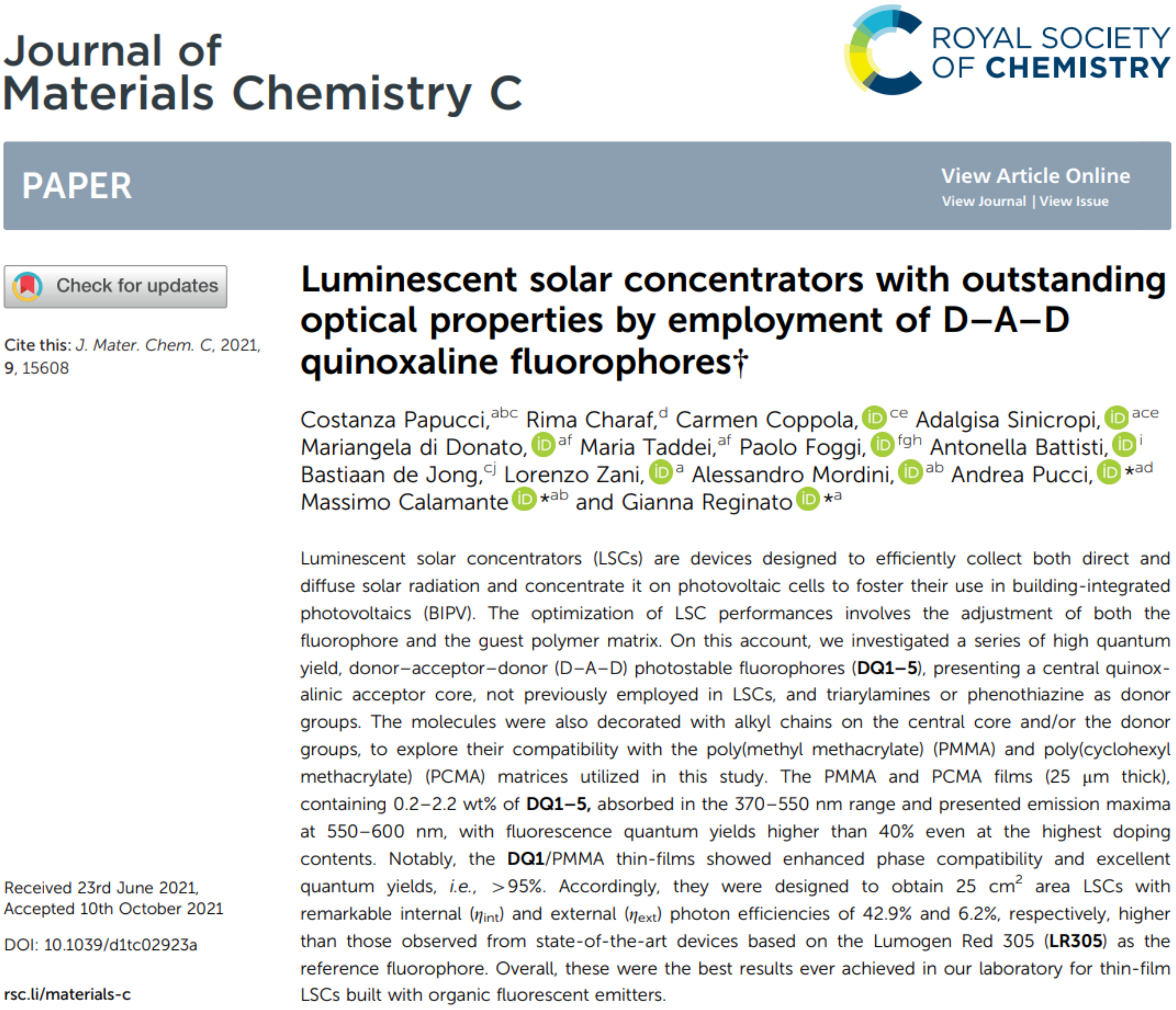

Journal of
Materials Chemistry C

ROYAL SOCIETY
OF CHEMISTRY

PAPER

View Article Online
View Journal | View Issue

Check for updates

Cite this: *J. Mater. Chem. C*, 2021, 9, 15608

Luminescent solar concentrators with outstanding optical properties by employment of D–A–D quinoxaline fluorophores†

Costanza Papucci,[abc] Rima Charaf,[d] Carmen Coppola,[ce] Adalgisa Sinicropi,[ace] Mariangela di Donato,[af] Maria Taddei,[af] Paolo Foggi,[fgh] Antonella Battisti,[i] Bastiaan de Jong,[cj] Lorenzo Zani,[a] Alessandro Mordini,[ab] Andrea Pucci,*[ad] Massimo Calamante*[ab] and Gianna Reginato*[a]

Luminescent solar concentrators (LSCs) are devices designed to efficiently collect both direct and diffuse solar radiation and concentrate it on photovoltaic cells to foster their use in building-integrated photovoltaics (BIPV). The optimization of LSC performances involves the adjustment of both the fluorophore and the guest polymer matrix. On this account, we investigated a series of high quantum yield, donor–acceptor–donor (D–A–D) photostable fluorophores (**DQ1–5**), presenting a central quinoxalinic acceptor core, not previously employed in LSCs, and triarylamines or phenothiazine as donor groups. The molecules were also decorated with alkyl chains on the central core and/or the donor groups, to explore their compatibility with the poly(methyl methacrylate) (PMMA) and poly(cyclohexyl methacrylate) (PCMA) matrices utilized in this study. The PMMA and PCMA films (25 μm thick), containing 0.2–2.2 wt% of **DQ1–5,** absorbed in the 370–550 nm range and presented emission maxima at 550–600 nm, with fluorescence quantum yields higher than 40% even at the highest doping contents. Notably, the **DQ1**/PMMA thin-films showed enhanced phase compatibility and excellent quantum yields, *i.e.*, >95%. Accordingly, they were designed to obtain 25 cm^2 area LSCs with remarkable internal (η_{int}) and external (η_{ext}) photon efficiencies of 42.9% and 6.2%, respectively, higher than those observed from state-of-the-art devices based on the Lumogen Red 305 (**LR305**) as the reference fluorophore. Overall, these were the best results ever achieved in our laboratory for thin-film LSCs built with organic fluorescent emitters.

Received 23rd June 2021,
Accepted 10th October 2021

DOI: 10.1039/d1tc02923a

rsc.li/materials-c

Luminescent solar concentrators (LSCs) represent an interesting concept in the field of photovoltaics[54]. They consist of a waveguide material (transparent glass or plastic) doped with a highly fluorescent fluorophore. They offer a potential solution for capturing sunlight efficiently over large areas by collecting light and guiding it to small solar cells by total internal reflection. Since the current of a device linearly scales with its size, a panel of half size but with double the intensity will produce an equal amount of power, while smaller panels are much easier to fabricate and integrate into building. At its core, an LSC is a transparent substrate, typically made of plastic or glass, which is embedded with luminescent species (e.g., organic dyes, quantum dots)[55]. These luminescent species are capable of absorbing incident sunlight and re-emitting it at a longer wavelength. In a collaboration with CNR-ICCOM and the university of Pisa, we investigated the performance increase of a series of high quantum yield, donor–acceptor–donor (D–A–D) photostable fluorophores compared to a commercial state-of-the-art LSC[56].

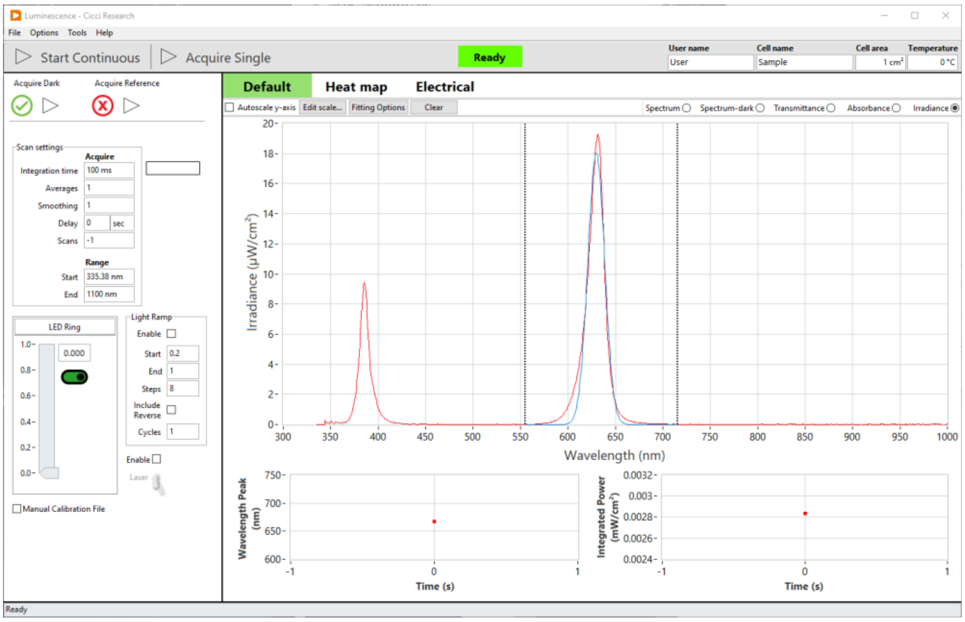

User name: User
Cell name: Sample
Cell area: 1 cm²
Temperature: 0 °C

Scan settings
Acquire
Integration time: 100 ms
Averages: 1
Smoothing: 1
Delay: 0 sec
Scans: -1
Range
Start: 335.38 nm
End: 1100 nm

LED Ring: 0.000

Light Ramp
Enable ☐
Start: 0.2
End: 1
Steps: 8
Include Reverse ☐
Cycles: 1

Enable ☐ Laser

☐ Manual Calibration File

Figure 26 – Software interface for the luminescence module showing an example of a photoluminescence signal of a perovskite solar cell illuminated by a 380 nm LED light. A gaussian fit is performed to estimate the power output.

In a photoluminescence (PL) test, a device is illuminated by light of a specific wavelength with an energy higher than the device's active layer's band gap. Since no electronics are attached to the device, PL is a non-contact, non-destructive method of probing materials. Some photons will be absorbed by the material causing electrons to move from the ground to excited state, provided the incident photon has a high enough energy to overcome the energy difference between the two states. After absorption, the luminescent species is typically in a vibrationally excited state within the excited electronic state. Before re-emission occurs, the species usually relaxes to the lowest vibrational level of that excited state through non-radiative processes, like phonon emissions (vibrations in the material). From the lowest vibrational level of the excited state, the luminescent species can return to the ground state by emitting a photon. The emitted light has a characteristic spectrum which is specific to the luminescent material in use. The non-radiative relaxation part causes the emitted photon to have a lower energy than the absorbed photon, a process called Stokes shift [55].

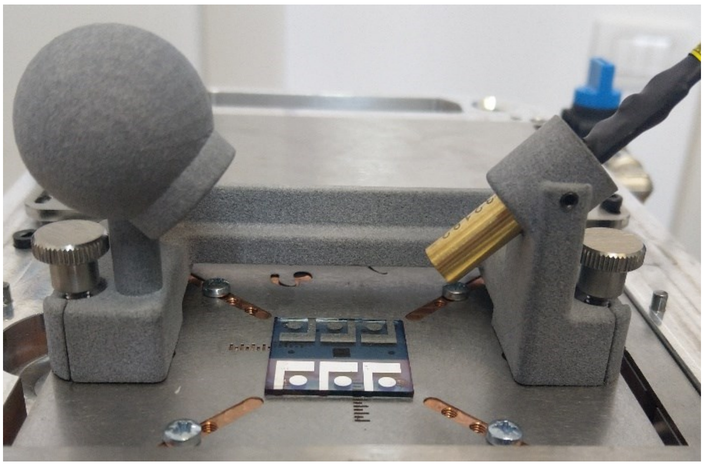

Figure 27 – Photoluminescence module showing a laser as a pump.

An LSC consisted of glass substrate on which is deposited a plastic material (here, poly(methyl methacrylate) (PMMA) and poly(cyclohexyl methacrylate) (PCMA) were investigated (Figure 28)) containing a fluorescent dopant (DQ1-5 (Figure 28)) with an absorption spectrum in the visible spectrum. The dopant should re-emit light with a Stokes shift such that the emission spectrum doesn’t overlap with the absorbance spectrum, which would result in reabsorption, negatively affecting the efficiency. Part of the re-emitted light will fall within the total internal reflection (TIR) angle, which will eventually guide it to the edge of the glass substrate where the light will be collected by solar cells [57]. An interesting application for these types of devices is the integration in building windows. The absorption spectrum, and therefore the colour of the device, can be tuned for aesthetics while the incident light can be absorbed by solar cell embedded in the window frames [54].

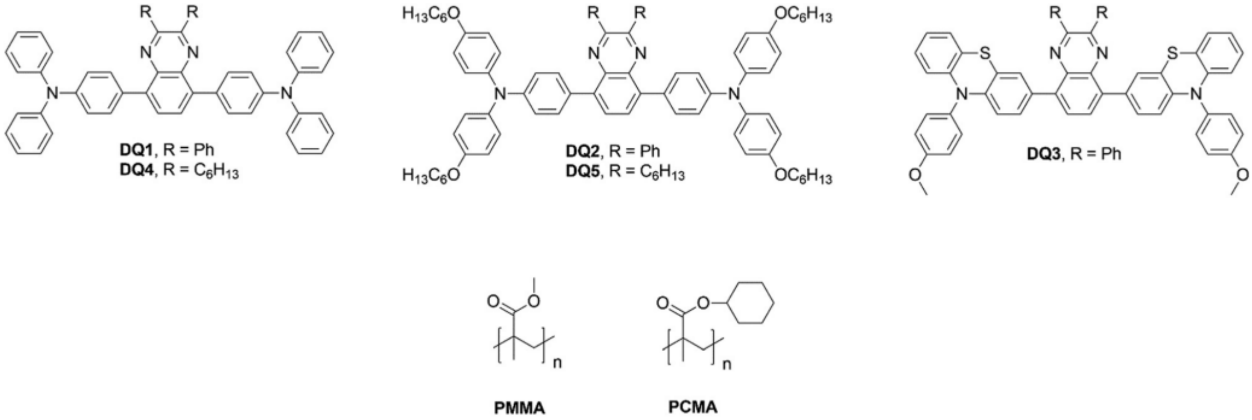

Figure 28 – Chemical structure of fluorophores based on 2,3-diphenyl-quinoxaline (DQ1-3) or 2,3-dihexyl-quinoxaline (DQ4-5) acceptor cores and of the used polymer matrices.

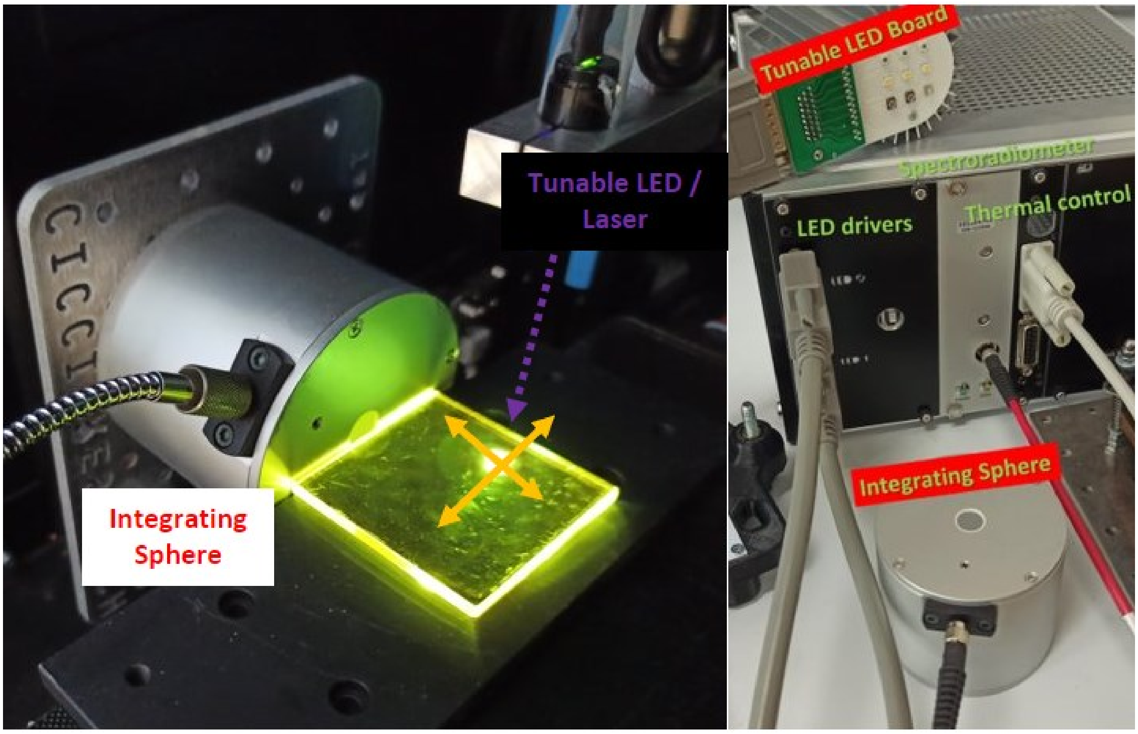

Figure 29 – Setup for measuring the quantum efficiency of an LSC.

The primary parameter determining the performance of an LSC is the ratio of number of photons reaching the lightguide edge to the number of incident photons. This metric provides a comprehensive understanding of the efficiency of the photon transport mechanism within the LSC. It evaluates the performance of luminophore emission, characterized by parameters such as the Stokes shift and photoluminescence quantum yield (PLQY), in conjunction with the quality of the light guide. The efficiency is often reported in one of two ways, each with different measurement setups. One efficiency is the actual ratio of emitted to incident number of photons, requiring a spectrometer with an integrating sphere collecting the edge-emitted photons. The second measures the generated power by a photovoltaic device attached to the edge. The former measures the actual physical efficiency, while the latter measures the practical efficiency as it would be applied in a real product[58].

Measuring the edge-emitted power density give more information and as such was decided to be measured. It can be further split into the external (η_{ext}) and internal (η_{int}) quantum efficiency. Where η_{ext} considers all incident photons, while η_{int} takes into account only the absorbed photons, disregarding any photons that are transmitted.

$$\eta_{ext} = \frac{\text{nr. edge-emitted photons}}{\text{nr. incident photons}}$$

$$\eta_{int} = \frac{\text{nr. edge-emitted photons}}{\text{nr. absorbed photons}}$$

Obviously, the spectrum of the incident light can greatly affect the efficiency of a device. If monochromatic light falling within the absorption spectrum is used, there won't be any transmitted photons, causing the external and internal efficiency to be equal. Practically, a standardized spectrum such as the AM1.5G solar spectrum should be used to fairly compare the performance of different LSC devices across the literature.

Finally, the area dependent concentration factor, C, should be reported. It is defined as the ratio between the incoming and emitted irradiance, where irradiance is given in W/m². Although both are given in units of power density, the incoming irradiance scales with area squared, while the emitted scales linearly with the area of the substrate, requiring the area to be reported to give the value relevance.

Figure 29 shows the setup for the measurement of the efficiency. Incident light coming from above, while the LSC is placed on a non-reflective black stage. An integrating sphere of 5 cm diameter and a 1 cm aperture is placed at the end of one edge. Because the integrating sphere does not capture the entire edge, it is attached to a motorized stage which can precisely move it 1 cm at a time until the irradiance of the entire edge is obtained. A convolution is then applied to obtain the total irradiance at one edge. A multi-LED based light source was used to mimic the AM1.5G spectrum.

Material	$\boldsymbol{\eta_{ext}}$ **(%)**	$\boldsymbol{\eta_{int}}$ **(%)**
LR305	4.7	16.6
DQ4	3.6	27.9
DQ1	6.2	42.9

Table 2 – Efficiencies for DQ1, DQ4 and a commercially available reference LSC

Table 2 shows the results of the efficiency measurements of the two best performing fluorophores compared to a state-of-the-art commercially available device (LR305). The investigated devices performed noticeably better than the LR305. Reabsorption of emitted photons negatively affects the efficiency[59]. To reveal the effects of reabsorption, the device was illuminated by a 350 nm laser creating a 0.25 cm² spot mounted on a motorized stage. The integrating sphere was placed in the middle of one of the edges. As the laser was moved away from the edge, the edge-emitted power was measured, resulting in a clear decrease of the power until the laser reached middle of the device, after which it stabilized. The normalized results shown in Figure 30 clearly shows the faster decrease in power from the LR305 device, implying a higher reabsorption rate, possibly due to the lowest Stokes shift of 36 nm compared to 106 and 89 nm for DQ1 and DQ4, respectively. This is further supported by a red shift of 20 nm in the emission spectrum.

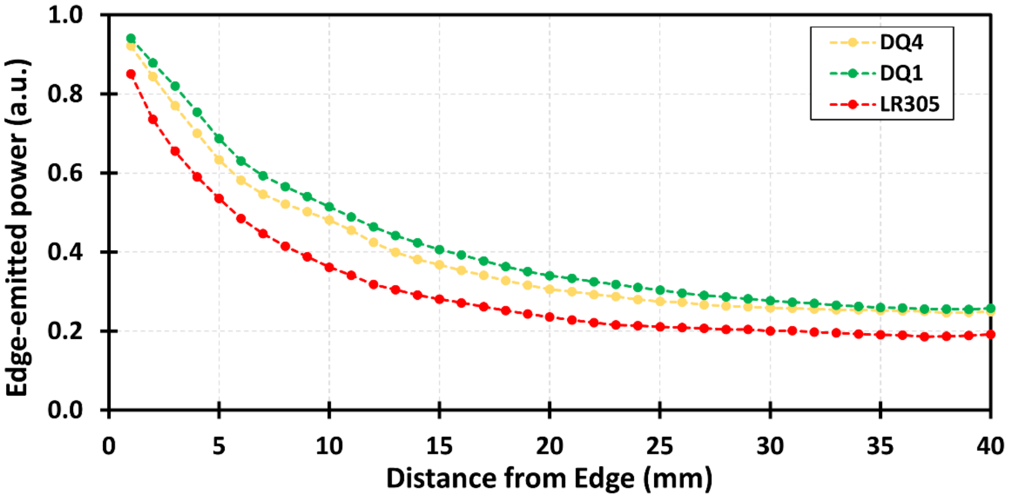

Figure 30 – A comparison of edge-emitted power as a 0.25 cm² 350 nm laser spot is moved across the LSC.

Although DQ1 showed the highest potential, the stability of the device must be investigated for to assess the use in practical applications. For this test, a larger 25x25 cm substrate was used and placed under a LED based light soaker at 1 sun equivalent. The edge-emitted power was monitored by a single-crystal silicon solar cell (ANYSOLAR SM182K01L). Figure 31a shows a sharp drop-off in power for the first 5 hours, after which it stabilizes until 20 hours of direct illumination.

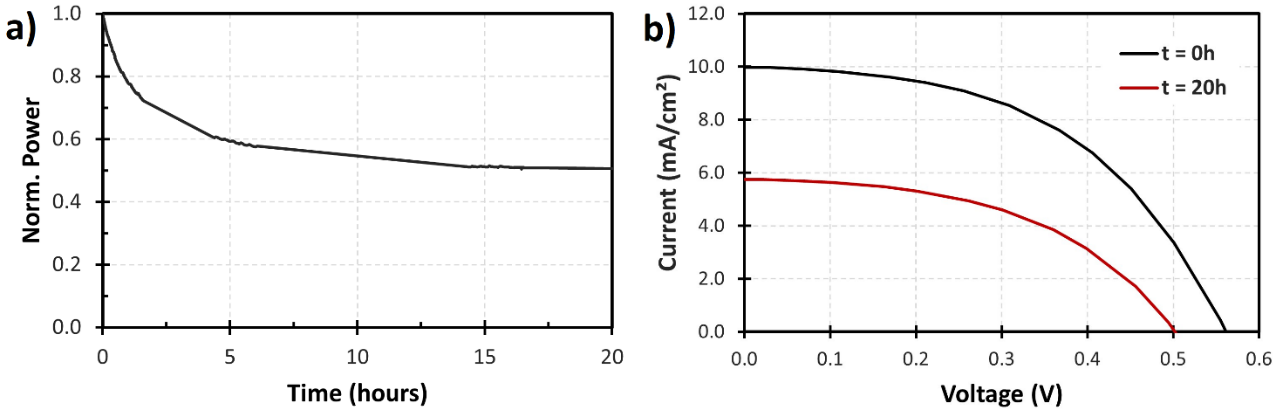

Figure 31 – a) Stability of the DQ1 LSC on a 25x25 cm substrate showing a fast drop in the first 5 hours, after which it stabilizes until 20 hours of direct sunlight. b) JV curves of the monitoring solar cell at the start and after 20 hours.

3.3 Absorbance Dynamics in Neuromorphic Organic Devices

The flexibility of the thermal stage combined using portable modules allows for the same module to be placed on top or on the bottom. For absorbance and transmittance analysis, the spectrometer module can be placed under the stage, while a light source, specifically the multiLED (see chapter 2.2.1), can easily be adapted with a 3D printed top-mounted bracket (Figure 32). Such a setup was used in a collaboration with the Eindhoven University of Technology and Istituto Italiano di Tecnologia Naples to investigate a transistor-like electrochemical neuromorphic organic device (ENODe) working as an artificial synapse[60]. Organic neuromorphic devices based on organic electrochemical transistors (OECTs) have shown a memory effect by permanently altering their conductivity by a factor of 2 after an electrical stimulus, only to reverse back after other electrical pulses.

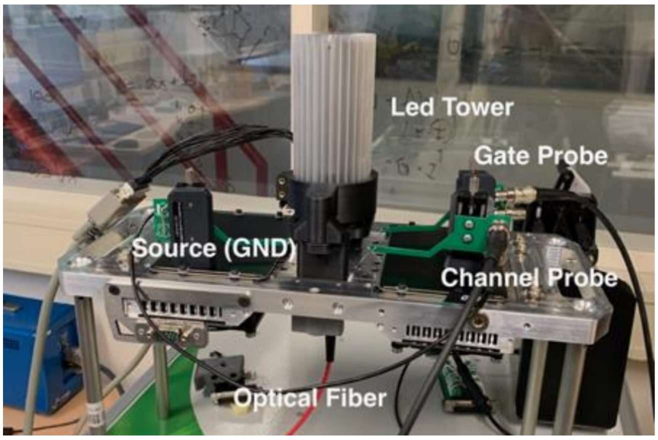

Figure 32 – Photograph of the thermal stage highlighting the positions of the ENODe device, the needle probes connections, the MultiLED and the optical fiber.

In the experiment, the plasticity of the channel conductance due to the presence of a neurotransmitter was investigated by measuring *in-situ* the absorbance or optical density (OD) changes as the gate electrode pulsed. Application of a voltage bias to the gate electrode initiates a de-doping process within the PEDOT:PS film, facilitated by the infiltration of cations into the bulk of the material. This de-doping process is reversible and is negated when the voltage bias is lifted. However, when high-frequency voltage pulses are used as input signals, this reversibility is compromised. As a consequence, cations progressively accumulate within the PEDOT channel, leading to an incremental de-doping effect that mimics short-term depressive (STD) behaviour.

As the experiment required the development of situ absorption measurements while simultaneously stimulating the device with electrical pulses to investigate the oxidation level of the dopamine as a measure of the memory effect. As two synchronized source meters were necessary, the recently developed Multichannel system was used (see chapter *5*) as a base. The flexibility of the system allows the programming of an arbitrary waveform sequence which can easily be generated using the integrated Arbitrary Waveform Tool. In conjunction with the electrical measurements, time-resolved OD measurements allow for in situ monitoring of the changing absorption peak, caused by the electrical pulses, by synchronizing the spectrometer acquisition to the source meter units. Spectra were continuously acquired, and the data displayed in real-time as the integral of the OD between the wavelength range of 550-650 nm during white LED light illumination. The gate was pulsed at 0.3 V for 3 s during the conditioning phase for 100 s, showing a permanent altering of the conductance. This plasticity was shown to be reversible through periodic gate pulses under PBS flow (Figure 33). Absorbance was calculated as

$$A = -\log_{10} T$$

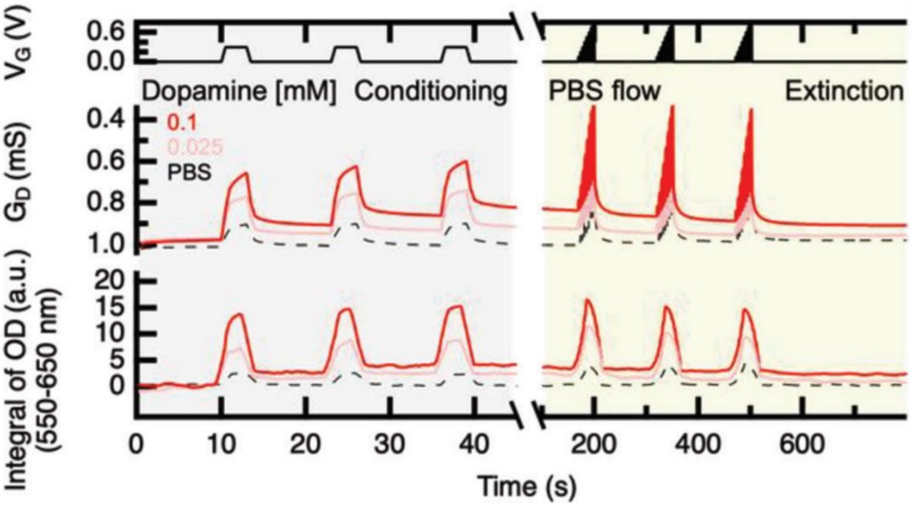

Figure 33 – Channel conductance modulation G_D and integral of optical density changes ∫OD upon gate periodic voltage pulses.

This single artificial synapse shows the first step for a biological neural network. Using the multichannel system with its multiple fully general SMUs, a network of these synapse can be established to perform multiple operation like learning and biological computation[61].

4 TRANSIENT AND DYNAMIC CHARACTERIZATION OF PEROVSKITE SOLAR CELLS

While steady-state characterization gives insights on the performance of a device, transient tests give an understanding of the physical behaviour leading to the performance losses in a device. Interesting parameters such as carrier lifetime and charge density can be calculated by observing the voltage and current decay of a device after it has been excited by light. Moreover, dynamic tests can help understand the behaviour in real-world changing conditions, important for grid stability and adaptability. With impedance spectroscopy showing a devices' frequency response allowing for the measurement of capacitance and inductance parameters, which can be important for AC-coupled systems and inverters. These parameters can be correlated and/or complement parameters extracted from steady state tests.

4.1 Perovskite Solar Cells

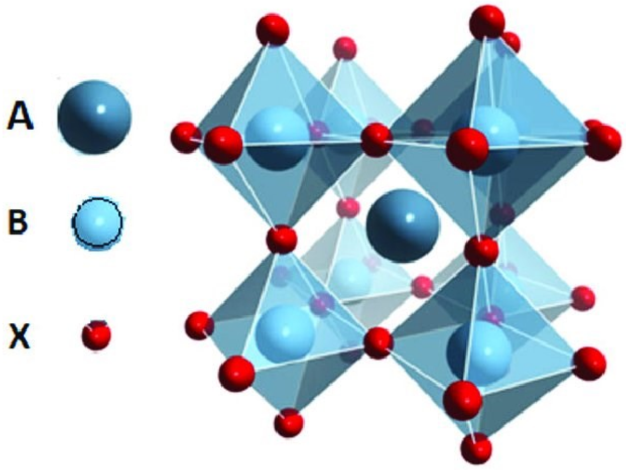

Figure 34 – General structure of a Perovskite[62].

PSCs have emerged as a promising next-generation photovoltaic technology due to their rapidly increasing power conversion efficiencies and relatively simple fabrication processes. A typical PSC comprises several layers[63]:

1. Transparent Conductive Electrode (TCE): Often fluorine-doped tin oxide (FTO) or indium tin oxide (ITO).
2. Electron Transport Layer (ETL): Commonly, titanium dioxide (TiO2) is used.
3. Perovskite Active Layer: The light-absorbing layer with a general formula of ABX3 (Figure 34). Here, A is a monovalent cation (e.g., methylammonium, formamidinium), B is a divalent metal cation (typically lead or tin), and X is a halide anion (e.g., iodide, bromide, or chloride).
4. Hole Transport Layer (HTL): Spiro-OMeTAD (2,2',7,7'-tetrakis[N,N-di(4-methoxyphenyl)amino]-9,9'-spirobifluorene) is a commonly used organic HTL.
5. Back Electrode: Gold (Au) or silver (Ag) are often employed.

The advantage of PSCs is their wide and tuneable bandgap by varying the composition of the ABX3 layer. Progress has been made in the structure of the PSC to improve the electron-hole diffusion lengths, charge carrier mobility and trap density to increase their efficiency from 2% in 2006 to over 25% today[6]. This combined with the flexibility, weight, and a lower potential production cost due to the application of roll-to-roll technology makes them a good candidate for the next generation of solar energy.

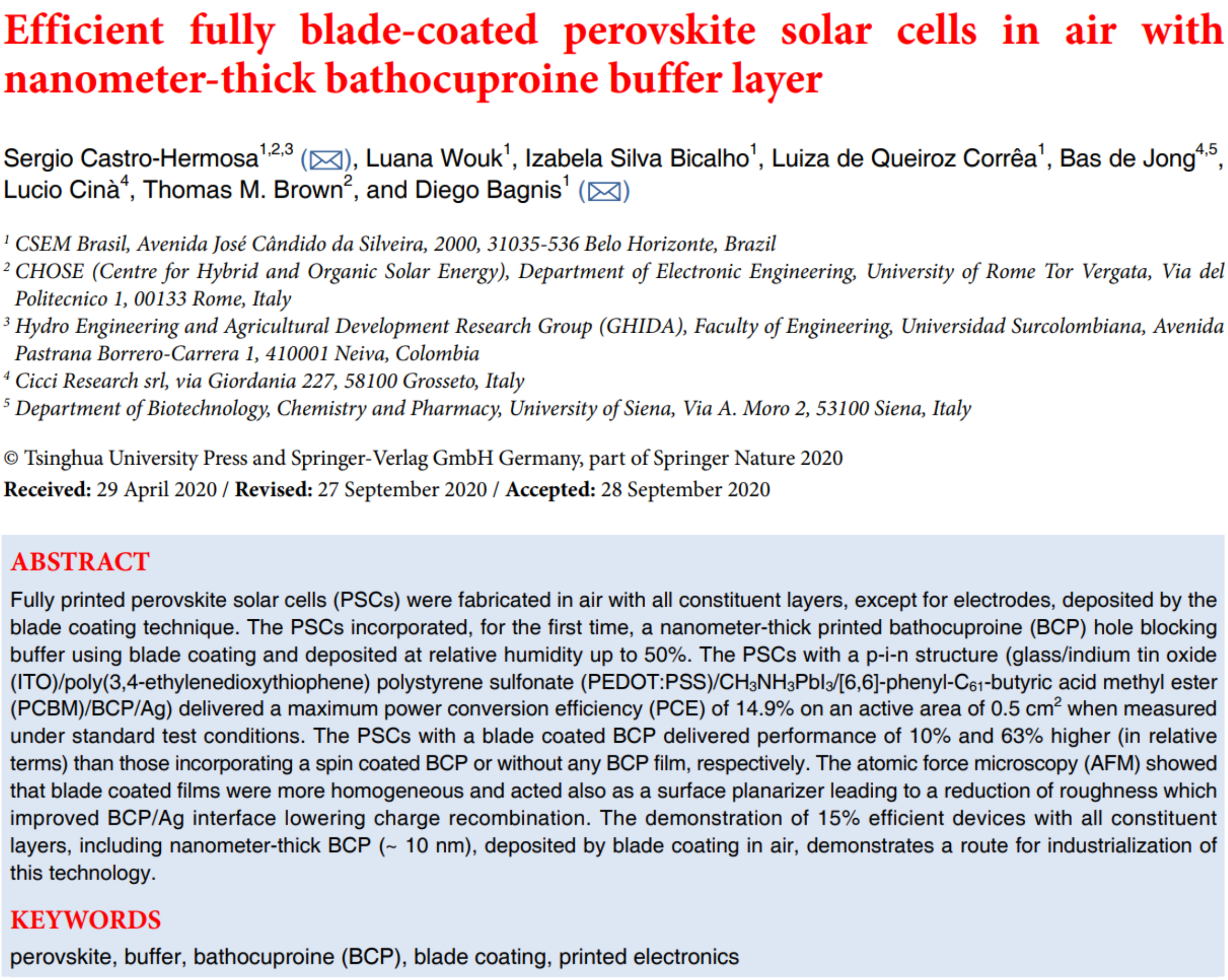

Efficient fully blade-coated perovskite solar cells in air with nanometer-thick bathocuproine buffer layer

Sergio Castro-Hermosa[1,2,3] (✉), Luana Wouk[1], Izabela Silva Bicalho[1], Luiza de Queiroz Corrêa[1], Bas de Jong[4,5], Lucio Cinà[4], Thomas M. Brown[2], and Diego Bagnis[1] (✉)

[1] *CSEM Brasil, Avenida José Cândido da Silveira, 2000, 31035-536 Belo Horizonte, Brazil*
[2] *CHOSE (Centre for Hybrid and Organic Solar Energy), Department of Electronic Engineering, University of Rome Tor Vergata, Via del Politecnico 1, 00133 Rome, Italy*
[3] *Hydro Engineering and Agricultural Development Research Group (GHIDA), Faculty of Engineering, Universidad Surcolombiana, Avenida Pastrana Borrero-Carrera 1, 410001 Neiva, Colombia*
[4] *Cicci Research srl, via Giordania 227, 58100 Grosseto, Italy*
[5] *Department of Biotechnology, Chemistry and Pharmacy, University of Siena, Via A. Moro 2, 53100 Siena, Italy*

Received: 29 April 2020 / **Revised:** 27 September 2020 / **Accepted:** 28 September 2020

ABSTRACT

Fully printed perovskite solar cells (PSCs) were fabricated in air with all constituent layers, except for electrodes, deposited by the blade coating technique. The PSCs incorporated, for the first time, a nanometer-thick printed bathocuproine (BCP) hole blocking buffer using blade coating and deposited at relative humidity up to 50%. The PSCs with a p-i-n structure (glass/indium tin oxide (ITO)/poly(3,4-ethylenedioxythiophene) polystyrene sulfonate (PEDOT:PSS)/$CH_3NH_3PbI_3$/[6,6]-phenyl-C_{61}-butyric acid methyl ester (PCBM)/BCP/Ag) delivered a maximum power conversion efficiency (PCE) of 14.9% on an active area of 0.5 cm^2 when measured under standard test conditions. The PSCs with a blade coated BCP delivered performance of 10% and 63% higher (in relative terms) than those incorporating a spin coated BCP or without any BCP film, respectively. The atomic force microscopy (AFM) showed that blade coated films were more homogeneous and acted also as a surface planarizer leading to a reduction of roughness which improved BCP/Ag interface lowering charge recombination. The demonstration of 15% efficient devices with all constituent layers, including nanometer-thick BCP (~ 10 nm), deposited by blade coating in air, demonstrates a route for industrialization of this technology.

KEYWORDS

perovskite, buffer, bathocuproine (BCP), blade coating, printed electronics

Up until now, only steady state and slow degradation phenomena have been described. In a collaboration with CSEM Brazil and CHOSE centre in Rome on the characterization of Perovskite solar cells (PSC)[45] the transient effects of perovskites were investigated. In particular, the effects of adding a nanometre-thick printed bathocuproine (BCP) hole blocking buffer to a Perovskite solar cell, by both spin coating and blade coating were compared. The devices were built with a p-i-n structure (glass/indium tin oxide (ITO)/poly(3,4-ethylenedioxythiophene) polystyrene sulfonate (PEDOT:PSS)/CH3NH3PbI3/[6,6]-phenyl-C61-butyric acid methyl ester (PCBM)/BCP/Ag). Transient photo response tests were performed to correlate to the results of IPCE and EL tests, confirming the improvement in performance due to addition of the BCP layer.

4.2 A Solar Cell in Reverse: Electroluminescence

Electroluminescence (EL) is a phenomenon where a material emits light in response to the passage of an electric current or a strong electric field[64]. This is a reciprocal process to the photoelectric effect, where the absorption of photons generates electron-hole pairs that can be mobilized by an external electric field. When a forward bias is applied to the p-n junction, electrons from the n-side gain enough energy to overcome the potential barrier and are injected into the p-side. Likewise, holes from the p-side move to the n-side. This carrier injection increases the minority carrier concentration on both sides. As the injected electrons move into the p-region and injected holes into the n-region, they recombine with majority carriers. Some of these recombination events are radiative, meaning that the recombination of an electron with a hole releases energy in the form of a photon. The shape of the photon emission spectrum is largely dependent on the band gap of the active material. The recombination releases photons with an energy more or less around the band gap, resulting in a characteristic Gaussian peak. The spectrum of emitted light when a material is excited can be modelled with the Planck's emission law:

$$B_{\mathrm{\mu}}(\mathrm{\mu}, T) = \frac{2h\nu^3}{c^2}\frac{1}{\exp\left(\frac{h\nu}{k_B T}\right) - 1}$$

However, this is for an ideal black body and the actual emission may be modified due to the properties of the material, such as its complex index of refraction and any possible photon re-absorption or scattering mechanisms. Furthermore, the emission is usually limited around the material's bandgap energy E_g typically expressed in terms of the wavelength λ_g as

$$E_g = \frac{hc}{\lambda_g}$$

Not all recombination processes result in an emitted photon. Instead, the energy is dissipated as heat or transferred to other carriers or lattice vibrations. Non-radiative recombination mechanisms are undesirable in photovoltaic devices because they reduce the efficiency of energy conversion. The three most important causes of non-radiative emission are the following.

- Shockley-Read-Hall (SRH) Recombination is the most common type of non-radiative recombination, where recombination occurs through defect states within the band gap. These defects could be vacancies, dislocations, impurities, or any irregularities in the crystal lattice. Carriers first get trapped in these defect (or trap) states and then recombine, transferring their energy to the lattice as heat.
- In Auger recombination, the energy released during the recombination of an electron and a hole is transferred to a third carrier, which is then excited to a higher energy state. This third carrier eventually releases the energy as heat when it relaxes back to a lower energy state.
- Surface recombination is other limitation in photovoltaic devices for radiative emission. During manufacturing, interlayer surfaces are often imperfect, resulting in recombination centres, in turn leading to higher rates of non-radiative recombination.

It is often difficult to capture all emitted photons, as they may be emitted in all directions. For a full qualitative analysis, the device should be placed in fully reflected integrating sphere which collects all light and focuses it to a singular aperture where the photons are captured by a spectrometer. Instead, if the EL signal is always captured in the same manner, by placing the device and optical aperture in a fixed position, the EL signal can be compared against devices of similar structures. A higher EL signal in one device indicates less defect states, implying a better performance.

This strategy was employed to show the relative difference in the EL signal between the device with a BCP layer and without. The results shown in Figure 35 highlight a quenching effect of BCP which was higher for films deposited by blade coating than spin coating. Quenching indicated a reduction of radiative recombination induced for the charge carrier extraction properties of the BCP/Ag cathode.

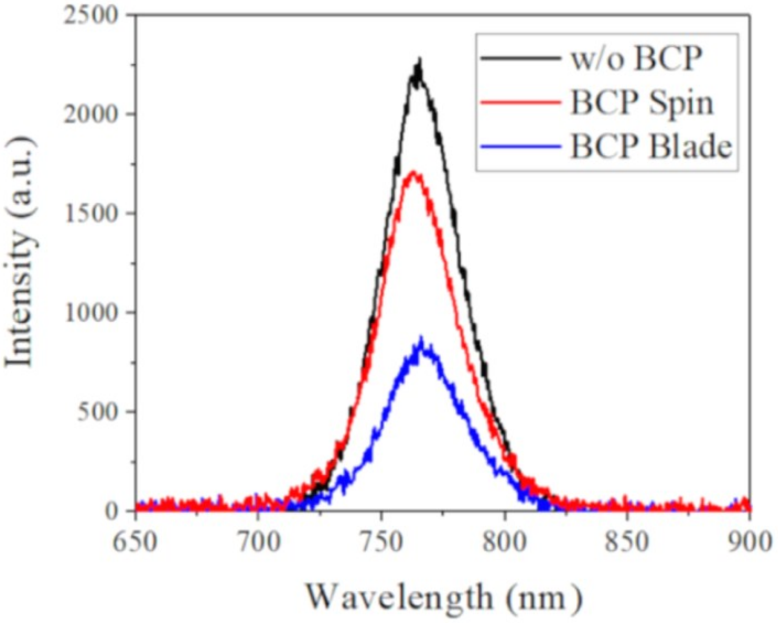

Figure 35 – Quenching effect in the EL signal of a perovskite device after adding a hole blocking buffer (BCP).

4.2.1 Pulsed Electroluminescence

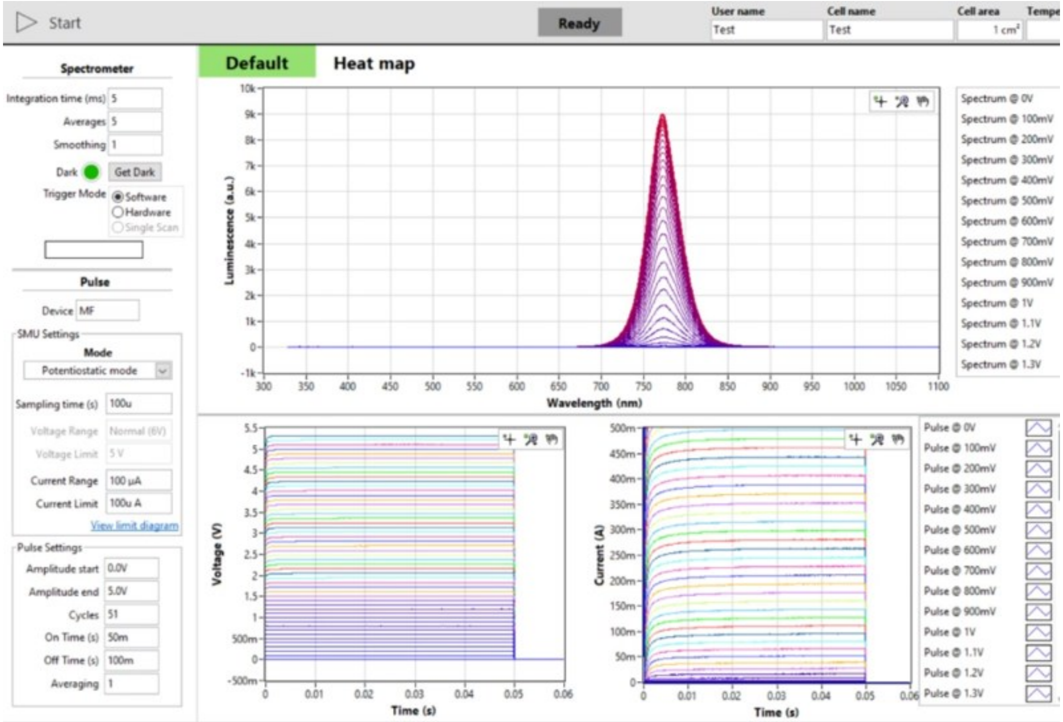
Ready
User name: Test
Cell name: Test
Cell area: 1 cm²

Spectrometer
Integration time (ms): 5
Averages: 5
Smoothing: 1
Dark ● Get Dark
Trigger Mode: ● Software ○ Hardware ○ Single Scan

Pulse
Device: MF
SMU Settings
Mode: Potentiostatic mode
Sampling time (s): 100u
Voltage Range: Normal (6V)
Voltage Limit: 5 V
Current Range: 100 µA
Current Limit: 100u A
View limit diagram
Pulse Settings
Amplitude start: 0.0V
Amplitude end: 5.0V
Cycles: 51
On Time (s): 50m
Off Time (s): 100m
Averaging: 1

Figure 36 – Example of a pulsed electroluminescence test showing a luminescence at very high currents applied on a small 0.5 cm² metal-halide perovskite PV.

At low current levels, the injection of carriers (electrons and holes) into the device is directly proportional to the applied current. If non-radiative recombination mechanisms are minimal, this leads to a nearly linear increase in the number of radiative recombinations, and hence, in the EL intensity. As the current further increases, various saturation effects can limit the proportionality between current and EL intensity. For example, trap states may become fully occupied, or Auger recombination rates may rise significantly, both due to the increase in carrier density and heating of the device due to current inefficiencies, leading to non-linear behaviour.

However, if the IQE (see section *3.1.3 - Quantum Efficiency*) is low, even high currents may not produce a strong EL signal, requiring a long integration time of the spectrometer, thus having the device under less-than-ideal conditions. Measuring a complete EL signal over a large range of voltages is often destructive, more so because it is not known at which current the device breaks down. The diode-like electrical behaviour of photovoltaic devices allow the current to continuously increase as the potential is increased. Instead of sending a continuous current, the device is pulsed at currents much higher than those which would otherwise destroy the device[65].

Figure 36 shows the software interface used to measure a pulsed EL signal. The device is pulsed in current long enough for the current and thus the EL signal to stabilize. The source meter unit (SMU) used to push the current is synchronized to a spectrometer. Once the current is stable, the spectrometer captures the signal using the exact same setup as for regular EL measurements. The pulses are repeated and averages as many times as necessary to increase the signal-to-noise ratio. The test is then repeated at different current levels. Figure 36 shows current levels of 0.5 A (2 orders of magnitude higher than its Jsc) without destroying the device, highlighting the power of this technique for devices with an EL signal too low to measure accurately when applying a continuous current.

The electrical signal requires some time to stabilize as the trap defects filled and ion migration has stopped as is clearly seen in Figure 36. This transient behaviour can reveal information about the recombination time and charge carrier density. As has been shown that electrical to optical behaviour is reversable in solar cell, techniques to extract these parameters instead use light pulses to excite charge carriers and analyse the electrical response.

4.3 Transient Photo Response

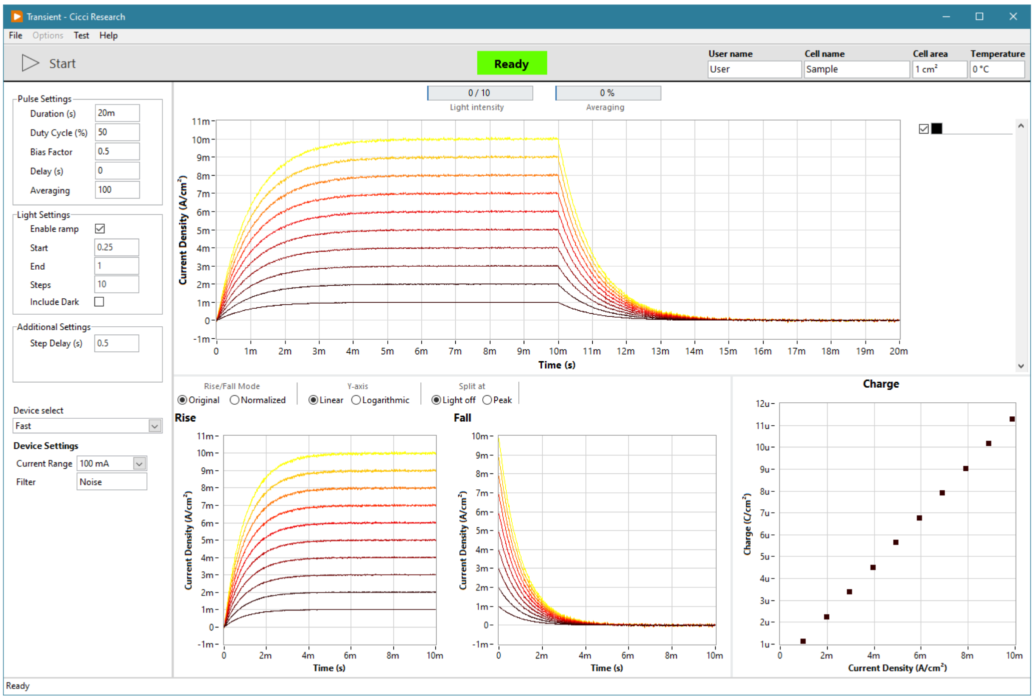

User name: User
Cell name: Sample
Cell area: 1 cm²
Temperature: 0 °C

Pulse Settings
Duration (s) 20m
Duty Cycle (%) 50
Bias Factor 0.5
Delay (s) 0
Averaging 100

Light Settings
Enable ramp ☑
Start 0.25
End 1
Steps 10
Include Dark ☐

Additional Settings
Step Delay (s) 0.5

Device select: Fast

Device Settings
Current Range 100 mA
Filter Noise

Rise/Fall Mode ● Original ○ Normalized
Y-axis ● Linear ○ Logarithmic
Split at ● Light off ○ Peak

Figure 37 – Software interface for the Transient Photo Response module. Showing an example of a Transient Photo Current measurement exhibiting an exponential current decay and automatic charge carrier density calculation.

In the Transient Photo-Voltage (TPV) test a device is illuminated by a short light pulse. The pulse should be short enough such that the generated charge carriers do not have enough time to fully recombine. The device is kept at open circuit so that no charge carriers are extracted, and all generated charges will recombine within the device. The device voltage is registered over time, from when the light turns on until all charges are recombined[66].

A large limitation off the efficiency of a devices is due to recombination of charge carriers after being excited and before reaching the contacts for extraction. Device with longer charge carrier lifetimes more efficiently extract generated charges and thus produce a higher current. Obtaining the charge carrier lifetime can be done by registering the decay of the open-circuit voltage Voc after the device stops being illuminated.

As described in section *3.1.2 - The Sun JV Test*, Voc is proportional on the incident light as:

$$V_{OC} \propto \ln(\phi)$$

Due to non-linear behaviour of the Voc, when the device would be illuminated from dark, a steady-state bias light is applied during the measurement. Then, a small light perturbation is applied on top of the bias light, ensuring that Voc increases approximately linear (slight changes in a non-linear system appear linear). This can be done by adding a second light source (often a laser is used). Instead, the All-in-one system uses a single LED which is driven by the fast function generator capable of outputting an arbitrary waveform. Due to the small perturbation over the bias light, many kinetics like trap filling and charge carrier concentrations can be considered constant. The decay of the voltage transient is therefore mono-exponential and can be fitted after normalization with[67]

$$\Delta V(t) \propto exp(-t/\tau_B)$$

Where τ_B is the first-order bulk recombination lifetime.

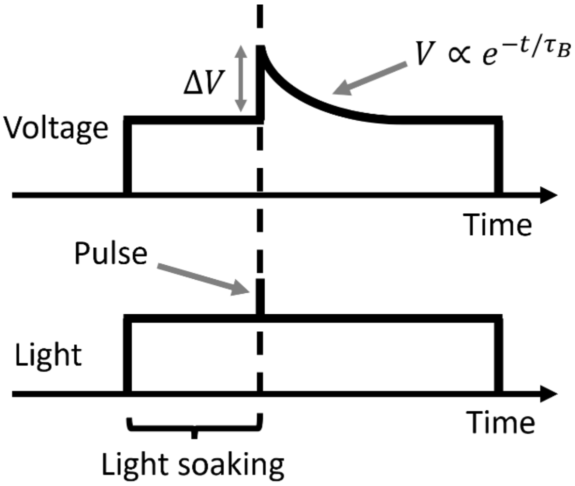

Figure 38 – Representation of the voltage (top) and light (bottom) signals for a TPV test.

Obtaining τ_B is done by fitting the decay curve according to the model shown in Figure 39. In general a mono-exponential fit is sufficient, i.e. $a_1e^{a_2x}$, however in some cases, there are two distinct recombination population, leading to the requirement of a bi-exponential fit[68]: $a_1e^{\tau_2x} + a_2e^{\tau_2x}$. If a monoexponential is sufficient then the two time constants of the bi-exponential fit will be the same. Therefore, biexponential fitting is always used to fit any decay curve.

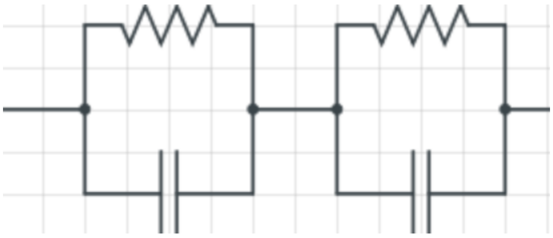

Figure 39 – Equivalent circuit used to model the bi-exponential decay behaviour of a transient photo voltage test.

The time constant for each intensity measurement can then be calculated as follows:

$$\tau_r = \frac{a_1\tau_1^2 + a_2\tau_2^2}{a_1\tau_1 + a_2\tau_2}$$

Increasing the bias light level, also increased the Voc increases, resulting in faster recombination dynamics[67] as clearly shown in Figure 40.

Note that the rise and fall graphs do not display an exponential curve immediately from the lights off state. It is constant for some time before charges start to recombine due to the presence of a shunt resistance. This delay may be longer or shorter depending on if the shunt resistance is higher or lower, respectively. Additionally, at very short time scales (ns - µs) there is a lag between the light pulse and the measurable signal due to transit times of the carriers[69]. The test gives an option to fit data starting from light off or from the voltage peak, which is useful in these particular cases.

Similar to the TPV test, but in short-circuit current conditions, the device is illuminated by short pulses to investigate the capability of generating charge carriers, providing insights into the charge collection efficiency. In a TPC test, a device is first illuminated to generate charge carriers (electron-hole pairs) under short-circuit conditions. Subsequently, these charges are extracted by rapidly switching off the light, and the resulting current is monitored. The integral of this extracted current over time gives a quantitative measure of the total number of charges that were present in the device at the moment of extraction.

$$Q = \int I(t)dt$$

The test is usually repeated at different light intensities or varying temperatures to provide insight into insight into different recombination mechanisms.

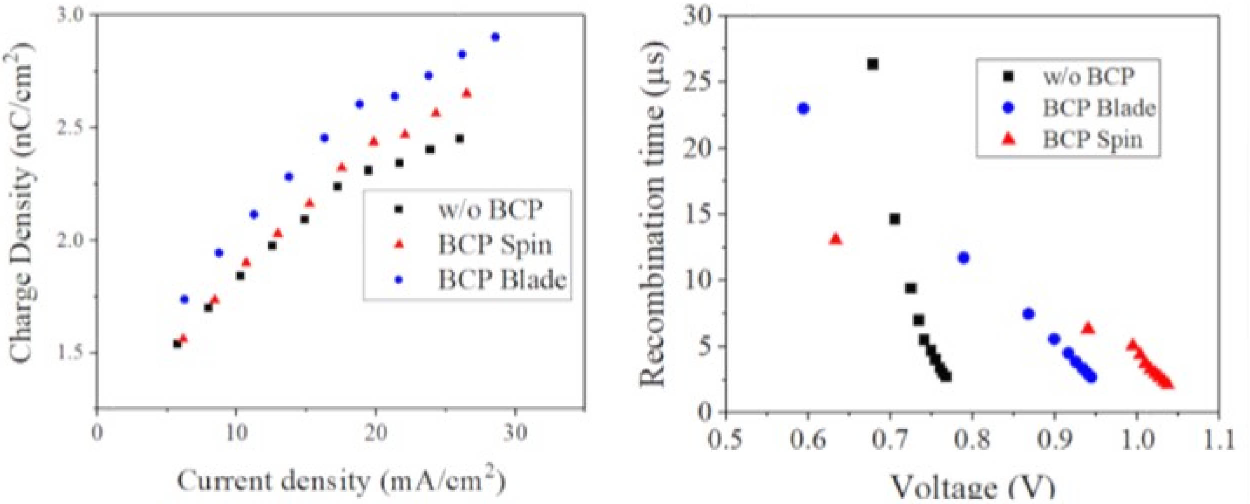

Figure 40 – Charge accumulation and charge carrier lifetime extracted from TPC and TPV decays, respectively, showing an improvement in both parameters after the addition of a BCP layer.

TPV and CE test were performed on the BCP enhanced perovskite devices introduced in chapter 4.2. They were performed using the fast oscilloscope and function generator driving a 5000K high-speed LED tuned to maintain a voltage perturbation within 50 mV above the bias light. Steady state bias light was increased from 0.1 to 2.0 sun equivalent. Recombination lifetime analysis showed a longer lifetime of the charge carriers when the BCP layer was added, with the spin coated technique providing the bigger improvement. Similarly, the charge extraction method revealed a PSC with a blade coated BCP film had the best extracted charge density. Which is consistent with the change in the EL signal (Figure 35) as well as the increased EQE due to the BCP layer[45]. The correlation between the different tests affirming each other's results shows the benefits of the all-in-one system by easily allowing multiple tests to be quickly performed.

5 FROM ONE DEVICE TO MANY: STATISTICS IN CHARACTERIZATION

During the development of the all-in-one system, it became clear that the throughput of measuring multiple devices wasn't enough for certain tests. In particular, the stability over time was impractical to measure for multiple devices as these tests regularly last 1000 hours[9]. Multiple devices must be measured to obtain statistically relevant data. While the performance of a single cherry-picked device can exceed 30%[6], devices are still tricky to manufacture, and the yield may not always be as expected. Advancements in production are still ongoing and to accelerate this process, as many devices as possible must be manufactured, and tested[8,9,70,71]. In addition to the challenges in the fabrication of PV devices, perovskites are vulnerable to extrinsic environmental properties such as temperatures, humidity and oxygen levels[72,73]. Encapsulation techniques protecting the devices are just as important and should be able to be tested simultaneously[71].

The single SMU, limits testing to only device at a time. One solution to improve the comfort of the user is to multiplex the SMU to an entire substrate with multiple pixels. This means that each pixel on the devices is connected using (usually) spring loaded contacts, but only one pixel is electrically connected to the SMU at a time. The system then automatically switches between all the pixels to measure each of them one after the other. Although this speeds up the total measurement time, because the user doesn't have to manually move the contact probes, the measurements are still not in parallel. Stability testing doesn't require the very high precision offered by the SMU in the All-in-one system since the tests are limited to JV and applying a more-or-less constant voltage. As such, the way forward for a multidevice measurement system was to implement a dedicated, independent, low cost, but lower precision, SMU for each device. To further lower the cost and complexity of the system, all SMUs are connected to a single high-speed multiplexed digitizer, capable of giving each SMU a 3 kS/s acquisition rate, plenty for the required tests. All source meter units are completely independent and fully controllable and can drive its device up to ±10 V, with currents up to ±250 mA. The digitizer can drive up to 32 SMUs, and multiple digitizers can easily be added to the system to increase the number of channels available in blocks of 32 devices. Source meter units are designed as plug-and-play boards in the Eurocard format. They connect to a custom backplane which provides power and communication with the computer.

Figure 41 shows an example of a source meter board being installed using the Eurocard rails and being connected to the backplane. Each Eurocard board contains 4 independent source meter unit (SMU) modules that can be accessed using a standardized DB25 connector. Each SMU measures and supplies voltage and current to the device. The voltage measurement contact points are connected, though a buffer, directly to the high-speed 250 kS/s digitizer, which has a programmable range from ±10 V down to ±0.10 V. Current flows through a current sensing resistance and the voltage drop is measured by the digitizer.

Each SMU has 2 current sensing resistors of 562 Ω and 5 Ω. As the digitizer can measure and supply a maximum of 10 V, these resistors allow for a maximum current of 18.8 mA and 2 A to flow. 2 A is too much for the small devices that the system is designed for, so it is limited to 250 mA to reduce cost and complexity of the SMUs.

The digitizer does not have infinite precision and at low currents, the signal-to-noise ratio starts to increase. The Low current range with the higher current sensing resistor improves the signal-to-noise ratio, but it may not be enough for currents less than ~10 µA. In that case, the current sensing resistor may be replaced by a higher resistance of, for example, 5 kΩ or 50 kΩ depending on the expected current of the devices. In addition, the SMUs have a current amplifier installed, which boosts the current by a factor of 10, 100 or 1000 for even more precision at the cost of maximum current to be measured.

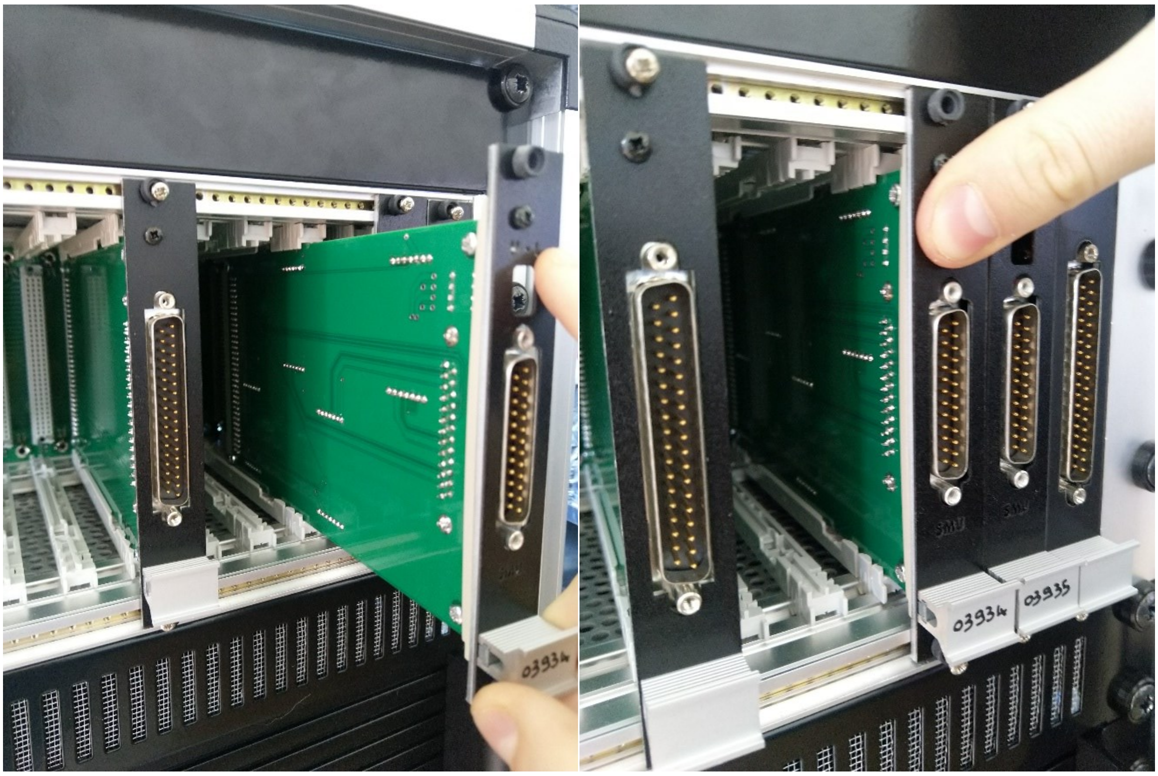

Figure 41 – Installing a source meter board. In this example 2 sensor boards are already installed. 2 source meter boards are inserted in slot 1 and 2.

To reduce load on both the devices and the SMUs, each SMU has an internal relay to switch the current to a high impedance (1 MΩ) state, blocking current flow. In this state, the connected devices may be considered in open-circuit voltage. This is useful both for checking whether the device is well connected as well as being able to measure the open-circuit voltage over time.

5.1 Challenges with Device Connections

Each digitizer can control 32 devices, or 8 SMUs with 4 devices each. In addition, 16 channels are available for monitoring the voltage of optional environmental sensors (see chapter: Environmental chamber). More blocks of 32 channels can be added with the same order. The simplest, most modular way to connect a device is using crocodile connecters attached to a DB25 connector, possibly through an extension cable (Figure 42).

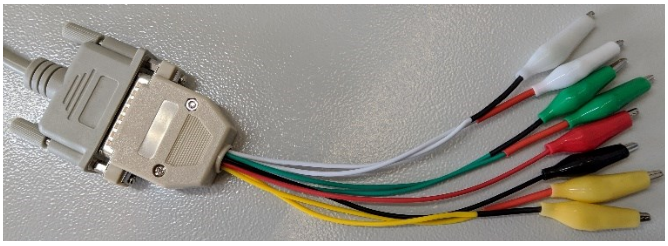

Figure 42 – Example of an adapter with crocodile clamps for manual connections to devices. Here, 4 devices can be connected to 1 SMU using the DB25 extension cable.

During the development of the system, it quickly became apparent that connecting many devices using crocodile clamps becomes unwieldy due to the number of cables required. Many device structures also had small contact pads which were difficult to connect and were easily destroyed when using clamps. Moreover, using clamps doesn't allow for device to be measured under different atmospheres. Unsealed devices may be testing in a nitrogen environments, requiring a sealed chamber[74]. if a standard device geometry is used, a PCB-based sample holder improves the connectivity, by allowing a device to simply be placed on preplaced pins. This is the same approach as discussed before with the multiplexed system, but now all devices can be measured in parallel.

A sample holder is generally a custom PCB with several spring-loaded probes positioned according to the device structure. The traces connect to a custom connector which in turn connects through a cable back to the source meter units. Devices on a sample holder are usually back contacted. This makes designing the sample holder easier as well as avoid having the contact probes blocking the incident light that is come from above. Devices are pushed onto the spring-loaded contacts using a metal mask with openings for the incident light. The mask can be fixed in place using screws or magnets.

Figure 43 shows an example of a sample holder for 32 devices in a small area. Since the devices are always grouped together in the same order, smaller and more flexible Samtec®, cables are used instead of 8 bulky DB25 connectors. These cables also carry the signals to measure the environmental sensors present on the sample holder. Testing each sample holder is not reliable when using lab-level devices since failing to measure a signal may be due to a failing device instead of failures in the sample holder. For each type of sample holder, instead, a custom PCB with the same layout as the solar cells is made. Solar cells are substituted with resistors to be able to reliable test the entire connection chain.

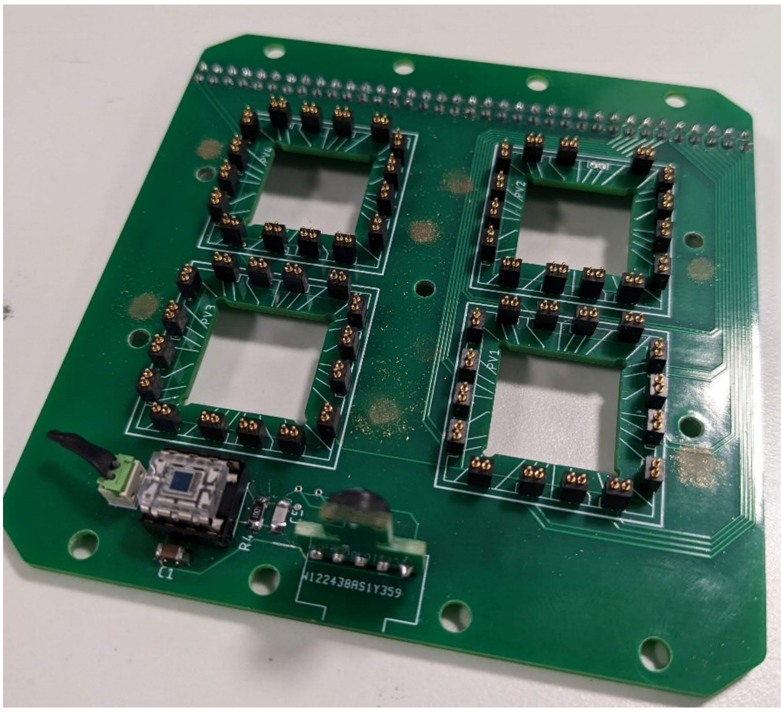

Figure 43 – Example of a sample holder connecting 4x8, or 32, devices distributed on 4 substrates. On the bottom left, temperature, humidity, and luminosity sensors can be found.

5.2 Stability Algorithms

There are 2 main purposes of the Multichannel system. The first and simplest is to acquire JV curves of many devices in parallel. By connecting up to 96 (3 banks or 32 SMUs) devices to the system and measuring them simultaneously, the research can be sped up immensely compared to measuring them one by one, even with a multiplexed system.

As an example, consider a standard perovskite solar cell with an open-circuit voltage (Voc) of 1.2 V. A JV scan is often done at 100 mV/s, starting from 0 V to Voc, a single scan takes 12 seconds, or 24 seconds if a reverse scan is included, which is often the case. Measuring multiple device one after the other will take increasingly more time. Using the Multichannel system, this time doesn't increase if more devices are added, although some extra time may be needed to connect the devices and verifying that all of them are well connected.

Once a preliminary JV has been performed, devices are biased to Voc, Jsc, MPP or a user selected fixed voltage. Some conditions are worse for the stability of a device than others, with Voc causing the fastest degradation[75–77]. MPP is most often chosen as it best represents the practical working condition of a device.

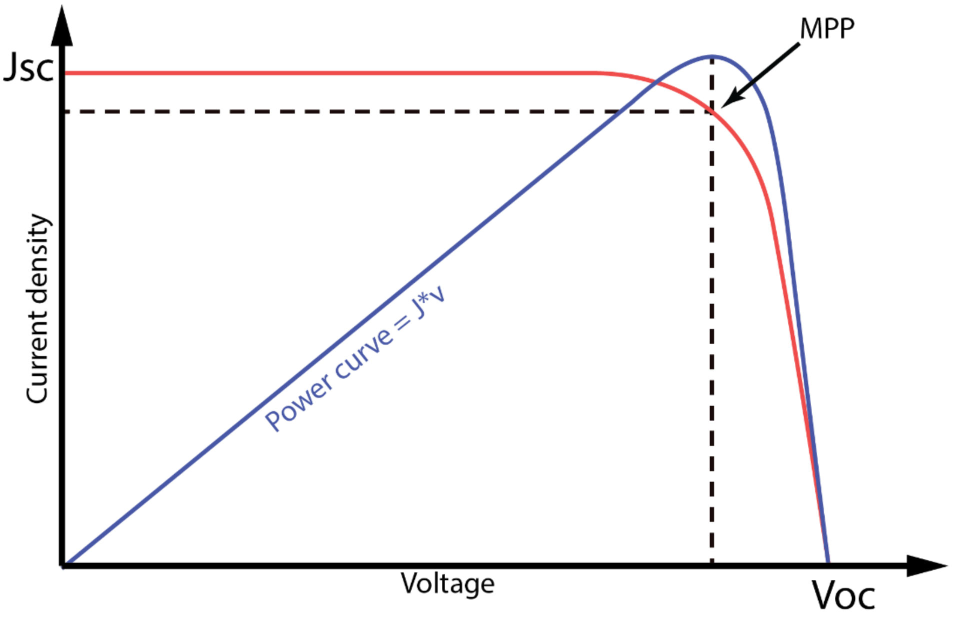

Figure 44 – Typical shape of a JV highlighting the important points.

Obtaining the maximum power point is done be performing a JV. A measurement with the Multichannel system will therefore always start with at least one JV curve. Apart from the MPP, other parameters from the JV such as, Voc, Jsc, FF and efficiency are recorded as well. The MPP obtained from the JV may not be the same as the steady-state maximum power point, especially in devices with hysteresis. Often, the steady state MPP is at a slightly higher voltage than in a JV curve. Because the MPP is unknown, and even more so that it can vary over time, a specialized algorithm is used to find the MPP and keep it there over longer periods of time. The Multichannel can implement three different algorithms: Perturb and Observe, Incremental Conductance and an in-house developed algorithm dubbed “stabilized MPPT”.

5.2.1 Perturb and Observe

The Perturb and Observe (PAO) algorithm is the most widely used algorithm for this task due its simplicity and robustness. Starting from an initial V_{MPP} obtained from the JV, the device is slightly positively and negatively perturbed (ΔV) with respect to V_{MPP}. This results in 3 points: $V_{MPP} - \Delta V$, V_{MPP}, $V_{MPP} + \Delta V$. For each point, the device power recorded, and the voltage associated with the maximum power is set as the new V_{MPP}[78]. The algorithm is then repeated indefinitely.

Jumps in voltage, especially when far from the MPP where the current changes more with changes in voltages, can cause problems in the measurement due to the capacitive effects of many photovoltaic devices. A JV scan stops either at Jsc (when measuring in reverse direction) or at Voc (when measuring in forward direction). A jump in voltage from this point to MPP causes a large current spike as the capacitive effect wears off. To avoid this issue, the Multichannel, therefore, slowly moves from the last JV point of the scan to the MPP. With a speed (in V/s) according to the JV scan speed. Similarly, when oscillating the voltage during the PAO tracking the voltage is moving in a triangle pattern instead of a sawtooth pattern as shown in Figure 45.

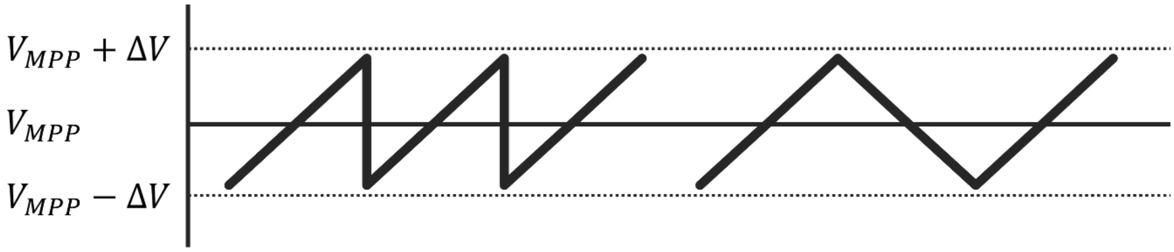

Figure 45 – The PAO used in the Multichannel software avoids sharp jumps in voltage (left). Instead, smoother transitions are always used (right).

The disadvantage of the PAO algorithm is the slow response if the MPP has large variation relative to the ΔV, for example when suddenly changing the intensity of the illuminating light source. Moreover, the ΔV must be chosen beforehand by the user, and an optimal value differs per device. Devices with higher V_{OC} require a higher ΔV (choosing a ΔV that is too low compared to the V_{MPP} can result in the algorithm tracking the noise level of the voltage measurement instead).

5.2.2 Incremental Conductance

Incremental Conductance (IC) tries to improve on the PAO algorithm by taking into account the slope between the three points[79]. A higher slope means that the actual working point is far away from the MPP, thus the ΔV is increased. Conversely, a lower slope means the working point is close to the maximum of the PV curve, thus the ΔV is reduced. This approach responds faster to sudden changes in MPP, has a higher precision as it can dynamically adapt the ΔV and is easier for the user since they don't have to set ΔV manually. ΔV will be limited to a minimum determined by the normalized power delta $\Delta P / P_{MPP}$ between steps, to not reduce ΔV below which the noise trend will be tracked instead of the actual MPP.

5.2.3 Stabilized MPPT

Both previous algorithms continuously oscillate the device in voltage[80]. In long term stability tests, one can assume a stable MPP. With this assumption, the MPP doesn't have to be checked as often, it can be checked once, and the device can stay there for a couple of minutes. In this "stabilized MPPT" algorithm the device is kept at a fixed voltage for longer periods of time compared to the previous algorithms (Figure 46). Care is taking during each step of the algorithm to not jump the voltage any higher than ΔV.

Voltage and current output of the device are continuously measured. Should the power output of the device suddenly drop more than 20 %, instead of moving slowly back to the new MPP as in the previous algorithms, a new JV is performed instead. A new MPP is quickly found, and the algorithm starts from the new MPP. Although this algorithm was designed for stable tests, day-night cycling with sudden switches in light intensity from light to dark or vice versa, can still be done with this algorithm.

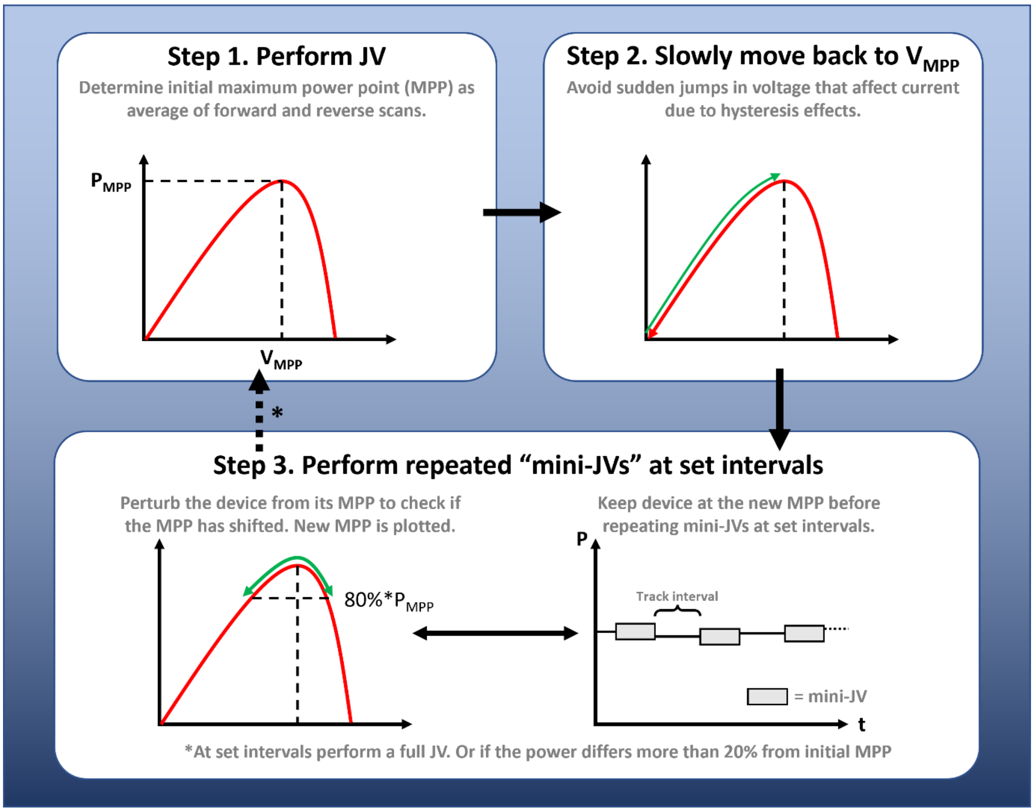

Figure 46 – Flowchart of the stabilized MPPT algorithm. MPP is checked at fixed intervals. A new JV is performed in case of sudden changes of MPP.

5.3 Environmental Control

As much as the light intensity of the incident light determines the performance of solar cells, so does the environment under which it is operating. Temperature and humidity play a big role in the stability of photovoltaics. Especially perovskites are very sensitive to humidity and many researchers are working on the encapsulation of their device to reduce damage done by moisture[11,81–83]. Some devices may work very well when operating in a sterile nitrogen environment but won't work very long under actual working conditions; the ultimate goal is to commercialize them, so they should work outdoors, or at least indoor.

The many factors that can influence the performance of a device make it difficult to compare results to other research if the test environment is different every time. Moreover, different device structures require different testing conditions. In 2011 testing guidelines and procedures for organic solar cells (OSC) were developed by a consortium of international researchers in the International Summit on Organic PV stability (ISOS) to provide a coherent and comparable approach to the stability assessment of these types of solar cells[84]. Similarly, for perovskite solar cells (PSC), a consensus of prominent researchers in the field was proposed based on the ISOS protocol. By following the ISOS procedures, researchers can ensure that the performance and durability of different devices are assessed using the same criteria, making comparisons more meaningful and accurate.

The key aspect of the ISOS protocol is the standardization of four stress factors during a stability measurement, summarized in Table 3. By imposing increasingly complex restrictions on these stress factors, standardized protocols can be designed. Figure 47 shows five categories with increasing restrictions and test complexity. The Multichannel system is designed to measure devices using any of the ISOS proposed protocols.

	Stress factor	Description
1	Light exposure	Specifies whether in dark or 1 sun equivalent, with UV present or not
2	Temperature	Specifies temperature at ambient (i.e. 25°C), 65°C or 85°C
3	Environment	Specifies ambient environment, e.g., ambient, indoor, outdoor, inert etc.
4	Electrical Load	Specifies the electrical condition, i.e., MPPT, OC or fixed voltage

Table 3 – Key stress factors laid down in the ISOS protocol.

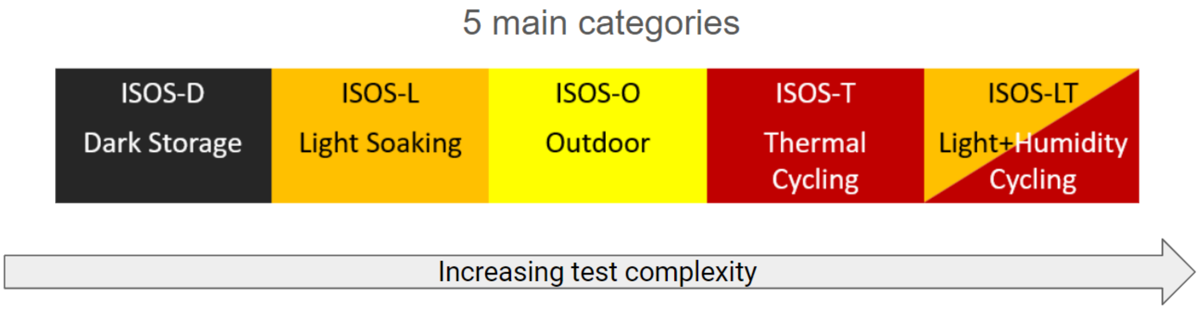

Figure 47 – The 5 ISOS categories with increasing complexity

5.3.1 Environmental chamber

The simplest ISOS-D protocol focuses on Damp Heat Exposure. It is designed to investigate the effects of temperature and humidity on photovoltaic devices. The measurement can be at ambient or a fixed temperature and in ambient air or with a fixed humidity. PSCs can quickly deteriorate if ambient gases (CO_2, NO, H_2S, etc.) come into contact with the active layer, leading to the formation of trap states and charge carrier barriers, resulting in the deterioration of the perovskite material and ultimately a reduction in the performance of the device[70]. Elevated temperature and humidity can accelerate these processes, allowing for faster testing[85]. During the development of an environmental chamber capable of achieving these conditions, it became clear that there was no one chamber fit for all requirements. At the moment, three different chambers are developed. Figure 48A shows the largest chamber with a working area of 15x30 cm capable of holding many devices at a time. A less bulky and more portable chamber was developed for use with gloveboxes. Figure 48B shows a square chamber, detachable from the temperature stage. This designed allows device to be inserted into the chamber inside a glovebox after which the entire chamber can be easily attached to the temperature stage. Lastly, Figure 48C shows a chamber having 4-compartments each which its own temperature controller and air/nitrogen inlet for individual environmental control. In addition, the round glass covers allow for top-mounted modules to be installed for individual light sources or in-situ luminescence measurements (Figure 6). The base of the chambers is made from an aluminium stage containing multiple PT100 Peltier-controlled heating and cooling systems, allowing a working temperature range of -5°C to 90°C.

Peltier elements, while having the advantage of have the capability of both heating and cooling, are not efficient at either of them. Therefore, a large heat sink is present under the stage with fans exhausting excess heat generated by the Peltier element. A glass cover with rubber sealing, seals the devices from the outside ambient environment, while allowing light to reach the devices. An inlet and outlet are present to allow humidity- and temperature-controlled air to flow through the system. Humidity levels between 0 % and 100 % are possible.

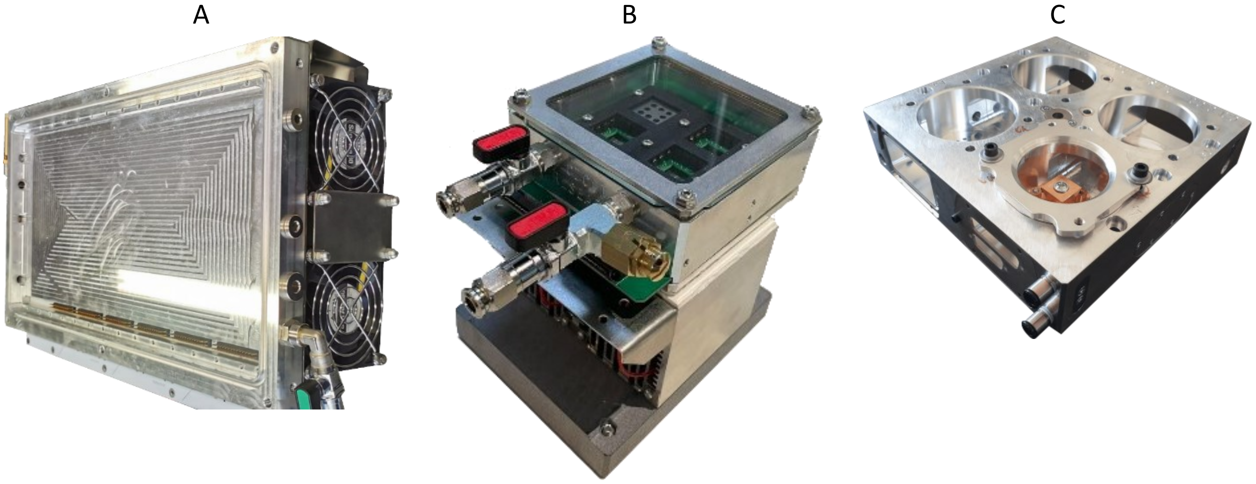

Figure 48 – Examples of different environmental chambers. A glass cover used to hermetically seal the devices. Devices are electrically connected in a sample holder and put in contact with the thermal stage.

Devices are electrically connected to the measurement system with the use of custom-designed sample holders. Many researchers have standardized designs for their substrates, which often contain multiple pixels. PCBs for electrical connections and 3D-print stand-offs to hold the devices in place can be quickly and cheaply made on-demand. Optionally, shadowing masks can be placed in the stand-offs. Sample holder such as in Figure 43 also have a hole allowing for an aluminium block to conduct heat from the temperature stage to the device. A pad of thermally conducting tape is placed between the device and the block to both increase the thermal conductivity and electrically insulate the device from the grounded stage.

Figure 6 shows a compact 4-compartment environmental chamber is designed to accommodate top-placed modules. It has the capability to house up to 16 devices (4 substrates per compartment with 4 pixels each) at a time. Each compartment is its own independent small chamber, with separate temperature control and air inlets compatible with the components of the XXL chamber. The top placed modules allow for more portability and flexibility in measurement setups. In the example 2 devices are illuminated by tuneable high-powered LED-based sources for accelerated testing under >1 illumination. This level of illumination usually requires a lot of power and cooling, but since the light is very close to the device, the power consumption is low, and a passive cooling solution is sufficient cool the LEDs. Another chamber is running electroluminescence tests with a spectrometer module on top to capture the luminescence signal. The simplicity of the design reduces the cost and maintenance, makes the setup more comfortable for the researcher and allows modular accessories to be used without requiring a technician.

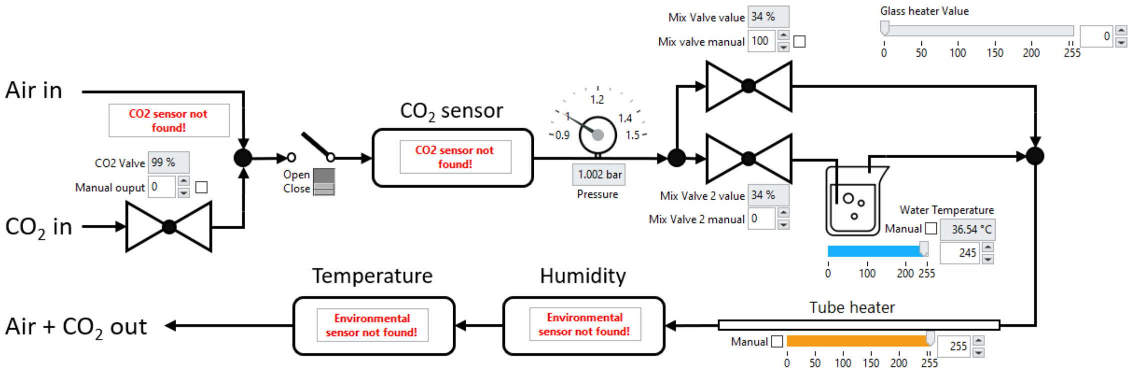

Figure 49 – software showing the schematic and control of several valves and sensors to output a controlled CO2 level.

Each chamber has a generic air inlet and outlet. This can be connected to a nitrogen source for inert environments or connected to an air unit. Figure 49 shows the layout of an in-house developed air unit able to control the temperature, humidity and CO2 level for controlled environments. Any of the inlets can be substituted with a gas of choice, provided the correct sensors are placed. With recent advancements in technology, these have become cheap and easy enough to use allowing for the simplicity and flexibility of this approach.

5.3.2 Light and thermal cycling

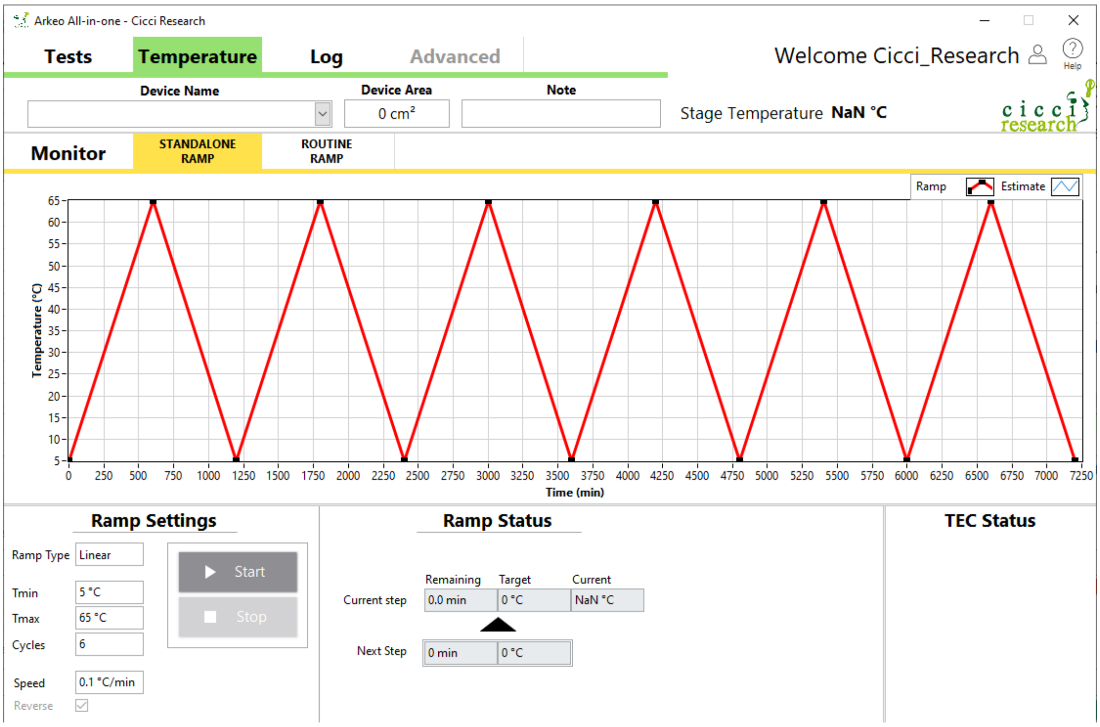

Device Name

Device Area 0 cm²

Note

Stage Temperature **NaN °C**

Ramp Settings

Ramp Type Linear
Tmin 5 °C
Tmax 65 °C
Cycles 6
Speed 0.1 °C/min
Reverse ☑

Ramp Status

	Remaining	Target	Current
Current step	0.0 min	0 °C	NaN °C
Next Step	0 min	0 °C	

Figure 50 – Software control of the temperature control driver board showing the setting for linear cycling between 5 °C and 65 °C with a period of 20 min.

The most complex ISOS protocols require cycling of illumination and/or temperature. The LED based solution allows for fine control of the intensity. Instead of turning the light on and off, a more realistic sine shape can be programmed to better simulate the outdoor day-night cycling.

The temperature stage with heating and cooling capability can be programmed and cycled according to the ISOS-T protocol. Varying temperatures are more realistic than fixed elevated temperatures and can indeed affect devices in different ways. Especially PSCs are sensitive to varying temperatures, with ion accumulation at the contacts being described as the reason. The temperature control driver can be programmed in a similar way to the LED driver board. Figure 50 shows the control software to set and monitor the temperature of an attached thermal stage. PT100 Peltier elements are used in all thermal stage variations, thus the software is universal for all thermal stage variations.

5.4 Control software

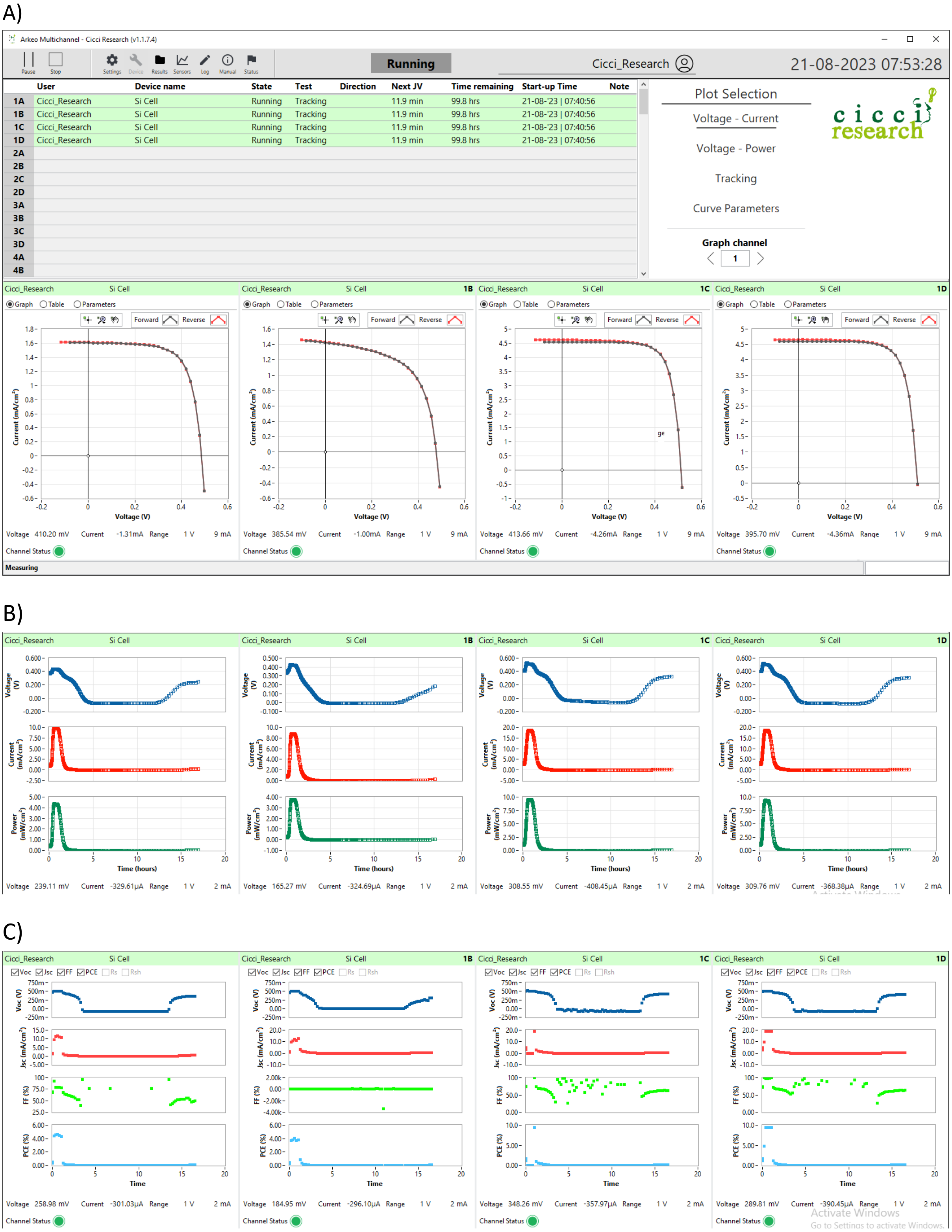

A)

	User	Device name	State	Test	Direction	Next JV	Time remaining	Start-up Time	Note
1A	Cicci_Research	Si Cell	Running	Tracking		11.9 min	99.8 hrs	21-08-'23 | 07:40:56	
1B	Cicci_Research	Si Cell	Running	Tracking		11.9 min	99.8 hrs	21-08-'23 | 07:40:56	
1C	Cicci_Research	Si Cell	Running	Tracking		11.9 min	99.8 hrs	21-08-'23 | 07:40:56	
1D	Cicci_Research	Si Cell	Running	Tracking		11.9 min	99.8 hrs	21-08-'23 | 07:40:56	
2A									
2B									
2C									
2D									
3A									
3B									
3C									
3D									
4A									
4B									

Cicci_Research Si Cell
Voltage 410.20 mV Current -1.31mA Range 1 V 9 mA
Channel Status ●

Cicci_Research Si Cell 1B
Voltage 385.54 mV Current -1.00mA Range 1 V 9 mA
Channel Status ●

Cicci_Research Si Cell 1C
Voltage 413.66 mV Current -4.26mA Range 1 V 9 mA
Channel Status ●

Cicci_Research Si Cell 1D
Voltage 395.70 mV Current -4.36mA Range 1 V 9 mA
Channel Status ●

Measuring

B)

Cicci_Research Si Cell
Voltage 239.11 mV Current -329.61μA Range 1 V 2 mA

Cicci_Research Si Cell 1B
Voltage 165.27 mV Current -324.69μA Range 1 V 2 mA

Cicci_Research Si Cell 1C
Voltage 308.55 mV Current -408.45μA Range 1 V 2 mA

Cicci_Research Si Cell 1D
Voltage 309.76 mV Current -368.38μA Range 1 V 2 mA

C)

Cicci_Research Si Cell
Voltage 258.98 mV Current -301.03μA Range 1 V 2 mA
Channel Status ●

Cicci_Research Si Cell 1B
Voltage 184.95 mV Current -296.10μA Range 1 V 2 mA
Channel Status ●

Cicci_Research Si Cell 1C
Voltage 348.26 mV Current -357.97μA Range 1 V 2 mA
Channel Status ●

Cicci_Research Si Cell 1D
Voltage 289.81 mV Current -390.45μA Range 1 V 2 mA
Channel Status ●

Figure 51 – The main window of the Multichannel software suite. 4 solar cells are being measured simultaneously and are being kept at their MPPT using the perturb & observe algorithm. A) shows a summary table and the latest JV of each device. B) Shows the voltage, current and power of the MPP over time. C) Shows the JV parameters of each JV scan over time.

The control software for system has been fully written in National Instruments® (NI) LabVIEW and runs on Windows. The language was chosen for its ease of implementation when working with NI hardware. The main monitoring window is shown in Figure 51. It shows a summary table of all channels with the status of each device. Under it, graphs showing the active measurements are shown. They can be switched between voltage-current, voltage-power, tracking over time, and JV parameters over time. 4 channels are always shown to reflect the 4 channels per SMU. All graphs are updated in real-time as the measurement is running.

The software is designed to be used by multiple people. While a measurement of another user is running, another user can log in to their appropriate account, setup their own device settings and add them to the ongoing measurement without disturbing the already ongoing measurements. The software manages each channel independently and in parallel. Each user has their own separate folder where their corresponding measurements are stored (see section: Data management).

5.4.1 Measurement process

The system is designed to perform parallelized JV and maximum power point tracking measurement. At the start of each measurement, a JV is always performed to get an estimate for the MPP. Once completed (if tracking is enabled), the voltage slowly (at the scan rate of the JV) moves to the MPP where it will perform any of the selected algorithms to keep the device at the desired point. This point can be any of the following:

- Maximum power point
- Open-circuit voltage (by setting the channel in high impedance)
- Short-circuit current
- Any voltage
- Any current

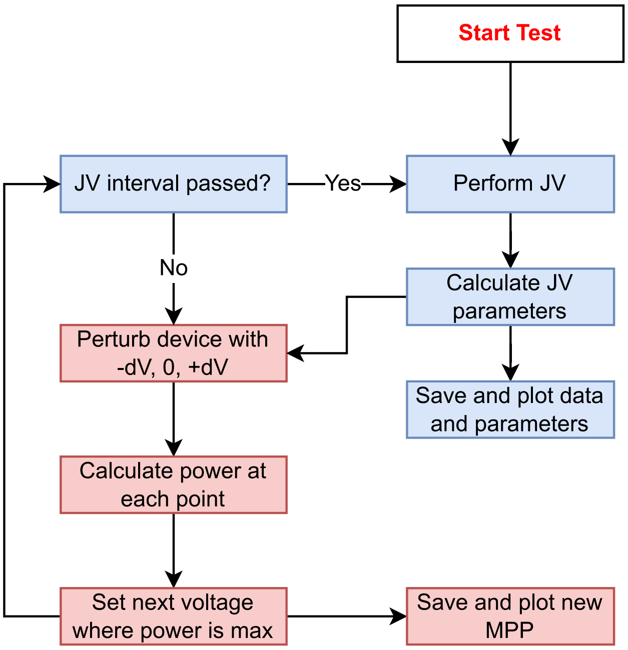

Figure 52 – Flowchart of a typical stability measurement with MPP tracking.

Since the boards are potentiostatic and lack a galvanostatic mode, all the above algorithms (except the open-circuit voltage, which simply sets the board in a high impedance state) use the PAO algorithm (or a variation as explained above) to keep the device at the desired set point. In the case of a fixed voltage, because there is no closed feedback loop, a small voltage drop due to the current flow, may introduce an offset between the set voltage and measurement voltage. This can be compensated by tracking the setpoint. During the JV scan, this may pose to be a problem as the voltage set is not the same as the actual voltage drop over the device. By default, JV scans start at a set voltage of -0.2 V instead of 0 V to make sure the JV scan crosses the current axis. Another solution is starting the scan in reverse. At V_{OC} the current is zero and therefore no voltage difference occurs. The voltage scan can then continue until the current axis is crossed.

For all points, at fixed intervals, a new JV is performed by default. This has 2 purposes. The first is to obtain JV parameters such as efficiency, fill factor, Voc and Jsc over time. These parameters give additional information about the degradation of devices compared to just measuring the MPP. The second is to ensure that the MPP is tracking the global maximum, and not a local maximum that may have formed over time.

5.4.2 Data management

When working with many devices as the same time, data management becomes a challenge. Moreover, the system is used by many different people, all with different needs. A standard hierarchy for storing data is maintained to allow for easier post processing. Minimal post-processing is done as the wishes for each researcher is different. The standard folder hierarchy is as follows:

[…]\<user name>\<start date>\<device name>_<channel>\<start time>\

This path is generated at the start of the measurement. Should the measurement take place over multiple days, the <start date> remains unchanged and all files are still saved in the same folder. The reason to add <start time> folder is to separate measurements should multiple be performed on the same day.

For a standard stability test, several files for each device will be generated at the start of and during the measurement:

1. *Parameters*
   This file contains a table of JV parameters, both for forward and reverse, of each JV scan. A timestamp is added to easily plot them as a function of time.
2. *Tracking*
   This file contains the voltage (V), current (A/cm²) and power (W/cm²) values of the device during the tracking phase of the measurement. A timestamp, in hours since the start, is included as well.
3. *JV*
   After each JV has been completed, a new file is generated containing the results of the JV scan. These files are numbered for easier sorting and post-processing.

5.4.3 File structure

To make data processing easier, all files have the same general structure, independent of the measurement type (Figure 53). Each file starts with a header section containing all measurement settings indicated by the `## Header ##` tag. Settings are further subdivided in categories indicated by the labels in square brackets. The `## Data ##` tag indicates where the actual measurement result begins. Data are always stored in a tab-delimited 2D array of values, always containing a header row. In the case of the JV file, a table with the JV parameters and a table with each raw data point of the JV scan is also stored. This file format is consistent among all different routines of the system.

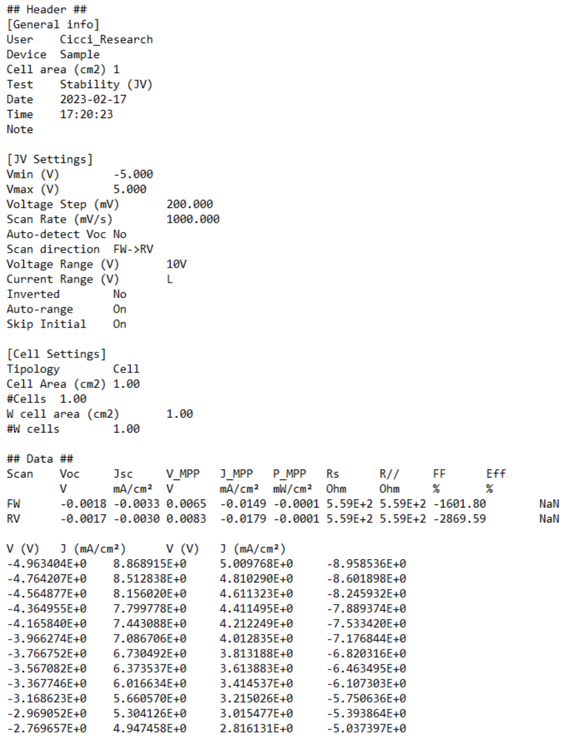

```
## Header ##
[General info]
User    Cicci_Research
Device  Sample
Cell area (cm2) 1
Test    Stability (JV)
Date    2023-02-17
Time    17:20:23
Note

[JV Settings]
Vmin (V)        -5.000
Vmax (V)        5.000
Voltage Step (mV)       200.000
Scan Rate (mV/s)        1000.000
Auto-detect Voc No
Scan direction  FW->RV
Voltage Range (V)       10V
Current Range (V)       L
Inverted        No
Auto-range      On
Skip Initial    On

[Cell Settings]
Tipology        Cell
Cell Area (cm2) 1.00
#Cells  1.00
W cell area (cm2)       1.00
#W cells        1.00

## Data ##
Scan    Voc     Jsc     V_MPP   J_MPP   P_MPP   Rs      R//     FF      Eff
        V       mA/cm²  V       mA/cm²  mW/cm²  Ohm     Ohm     %       %
FW      -0.0018 -0.0033 0.0065  -0.0149 -0.0001 5.59E+2 5.59E+2 -1601.80        NaN
RV      -0.0017 -0.0030 0.0083  -0.0179 -0.0001 5.59E+2 5.59E+2 -2869.59        NaN

V (V)   J (mA/cm²)      V (V)   J (mA/cm²)
-4.963404E+0    8.868915E+0     5.009768E+0     -8.958536E+0
-4.764207E+0    8.512838E+0     4.810290E+0     -8.601898E+0
-4.564877E+0    8.156020E+0     4.611323E+0     -8.245932E+0
-4.364955E+0    7.799778E+0     4.411495E+0     -7.889374E+0
-4.165840E+0    7.443088E+0     4.212249E+0     -7.533420E+0
-3.966274E+0    7.086706E+0     4.012835E+0     -7.176844E+0
-3.766752E+0    6.730492E+0     3.813188E+0     -6.820316E+0
-3.567082E+0    6.373537E+0     3.613883E+0     -6.463495E+0
-3.367746E+0    6.016634E+0     3.414537E+0     -6.107303E+0
-3.168623E+0    5.660570E+0     3.215026E+0     -5.750636E+0
-2.969052E+0    5.304126E+0     3.015477E+0     -5.393864E+0
-2.769657E+0    4.947458E+0     2.816131E+0     -5.037397E+0
```

Figure 53 – Example of a JV file showing the measurement settings under the ## Header ## tag and the data values under the ## data ## tag.

Rarely are the results of a single device representative for the performance of the device structure. Oftentimes, many devices with the same structure are measurement in parallel and the results are compared for statistical analysis. The software allows for devices to be grouped together using a group tag. This indicates to the software that the data files of those devices should be grouped together for easier selection of files during post-processing. For channels with a group tag, the folder hierarchy of the files is now changed to:

[…]\<User>\<Date>\<Group_tag>\<Start_time>\<Channel>\files.txt

In addition to grouping files together by their group tag, they are further grouped by their start time in case multiple measurement with the same group name are started. For each group tag, a file containing the average of the voltage, current and power is saved. Outliers are identified as having a more than 50% difference from the median value. This method is used to automatically perform statistics when many devices are measured in parallel.

6 CONCLUSION

A characterization system for opto-electronic tests has been utilized for the complete assessment of bio-inspired hybrid organic-inorganic technologies. Correlation of the IPCE, EL, TPV and TPC testing protocols confirming the validity of the tests had been demonstrated on perovskite and dye-sensitized device. Multiple programmable LED based light sources were developed to provide the illumination for different use cases, from monochromatic absorption and luminescence experiments to long term aging. Moreover, the flexibility of the system was demonstrated as the system was adapted for device other than photovoltaics. The efficiency and concentration factor of luminescent solar cells with different fluorophores were measured by employing a tuneable LED light source and a portable spectrometer module. The same setup was used to characterize in situ the absorbance of electrochromic neuromorphic devices also requiring the use of multiple synchronized source meter units. A newly developed software routine resulted in a complete understanding of the temporal chromaticity due to ion migration in the device.

In addition, a simpler, multidevice system has been shown to successfully measure the maximum power point dynamics of multiple devices over 1000 hours. Environmental chambers were developed in the process of making the system which were designed to adhere to the ISOS protocol for photovoltaics. Different points along the JV curve can be tracked over time, as the MPPT is the most important, three algorithms to keep the device at this point; the industry-standard Perturb and Observe, incremental conductance and an inhouse designed “stabilized MPPT” reducing the oscillation of the device during measurements.

7 REFERENCES

1. The rapid growth in global wealth | McKinsey. https://www.mckinsey.com/industries/financial-services/our-insights/the-rise-and-rise-of-the-global-balance-sheet-how-productively-are-we-using-our-wealth#/.
2. Ferguson, R., Wilkinson, W. & Hill, R. Electricity use and economic development. *Energy Policy* **28**, 923–934 (2000).
3. Solar power generation. *Our World in Data* https://ourworldindata.org/grapher/solar-energy-consumption.
4. International Technology Roadmap for Photovoltaic (ITRPV) - vdma.org - VDMA. https://www.vdma.org/international-technology-roadmap-photovoltaic.
5. Solar PV. *IEA* https://www.iea.org/energy-system/renewables/solar-pv.
6. Best Research-Cell Efficiency Chart. https://www.nrel.gov/pv/cell-efficiency.html.
7. Zhang, Y., Kim, M., Wang, L., Verlinden, P. & Hallam, B. Design considerations for multi-terawatt scale manufacturing of existing and future photovoltaic technologies: challenges and opportunities related to silver, indium and bismuth consumption. *Energy Environ. Sci.* **14**, 5587–5610 (2021).
8. Wang, R. *et al.* A Review of Perovskites Solar Cell Stability. *Adv. Funct. Mater.* **29**, 1808843 (2019).
9. Dipta, S. S. & Uddin, A. Stability Issues of Perovskite Solar Cells: A Critical Review. *Energy Technol.* **9**, 2100560 (2021).
10. Pazoki, M., Cappel, U. B., Johansson, E. M. J., Hagfeldt, A. & Boschloo, G. Characterization techniques for dye-sensitized solar cells. *Energy Environ. Sci.* **10**, 672–709 (2017).
11. Aitola, K. *et al.* Encapsulation of commercial and emerging solar cells with focus on perovskite solar cells. *Sol. Energy* **237**, 264–283 (2022).
12. Kirchartz, T., Ding, K. & Rau, U. Fundamental Electrical Characterization of Thin-Film Solar Cells. in *Advanced Characterization Techniques for Thin Film Solar Cells* 33–60 (John Wiley & Sons, Ltd, 2011). doi:10.1002/9783527636280.ch2.
13. Neukom, M., Züfle, S., Jenatsch, S. & Ruhstaller, B. Opto-electronic characterization of third-generation solar cells. *Sci. Technol. Adv. Mater.* **19**, 291–316 (2018).
14. Fraisse, G., Ramousse, J., Sgorlon, D. & Goupil, C. Comparison of different modeling approaches for thermoelectric elements. *Energy Convers. Manag.* **65**, 351–356 (2013).
15. Sharpe, L. T., Stockman, A., Jagla, W. & Jägle, H. A luminous efficiency function, VD65* (λ), for daylight adaptation: A correction. *Color Res. Appl.* **36**, 42–46 (2011).
16. Cui, Y. *et al.* Accurate photovoltaic measurement of organic cells for indoor applications. *Joule* **5**, 1016–1023 (2021).
17. Chinigò, G. *et al.* Polymethine dyes-loaded solid lipid nanoparticles (SLN) as promising photosensitizers for biomedical applications. *Spectrochim. Acta. A. Mol. Biomol. Spectrosc.* **271**, 120909 (2022).
18. Bordignon, N. *et al.* Quatsomes Loaded with Squaraine Dye as an Effective Photosensitizer for Photodynamic Therapy. *Pharmaceutics* **15**, 902 (2023).
19. Gonzalez-Pedro, V. *et al.* General Working Principles of CH3NH3PbX3 Perovskite Solar Cells. *Nano Lett.* **14**, 888–893 (2014).
20. Jung, H. S. & Park, N.-G. Perovskite Solar Cells: From Materials to Devices. *Small* **11**, 10–25 (2015).
21. O'Regan, B. & Grätzel, M. A low-cost, high-efficiency solar cell based on dye-sensitized colloidal TiO2 films. *Nature* **353**, 737–740 (1991).

22. Nazeeruddin, Md. K., Baranoff, E. & Grätzel, M. Dye-sensitized solar cells: A brief overview. *Sol. Energy* **85**, 1172–1178 (2011).

23. A. Mazzio, K. & K. Luscombe, C. The future of organic photovoltaics. *Chem. Soc. Rev.* **44**, 78–90 (2015).

24. Kippelen, B. & Brédas, J.-L. Organic photovoltaics. *Energy Environ. Sci.* **2**, 251–261 (2009).

25. Ranabhat, K. *et al.* An introduction to solar cell technology. *J. Appl. Eng. Sci.* **14**, 481–491 (2016).

26. Fonash, S. *Solar Cell Device Physics*. (Elsevier, 2012).

27. Nelson, J. A. *The Physics Of Solar Cells*. (World Scientific Publishing Company, 2003).

28. Koster, L. J. A., Mihailetchi, V. D., Ramaker, R. & Blom, P. W. M. Light intensity dependence of open-circuit voltage of polymer:fullerene solar cells. *Appl. Phys. Lett.* **86**, 123509 (2005).

29. Wang, Z.-S., Kawauchi, H., Kashima, T. & Arakawa, H. Significant influence of TiO2 photoelectrode morphology on the energy conversion efficiency of N719 dye-sensitized solar cell. *Coord. Chem. Rev.* **248**, 1381–1389 (2004).

30. Zhang, D. *et al.* A molecular photosensitizer achieves a Voc of 1.24 V enabling highly efficient and stable dye-sensitized solar cells with copper(II/I)-based electrolyte. *Nat. Commun.* **12**, 1777 (2021).

31. Gokilamani, N., Muthukumarasamy, N., Thambidurai, M., Ranjitha, A. & Velauthapillai, D. Utilization of natural anthocyanin pigments as photosensitizers for dye-sensitized solar cells. *J. Sol-Gel Sci. Technol.* **66**, 212–219 (2013).

32. Syafinar, R., Gomesh, N., Irwanto, M., Fareq, M. & Irwan, Y. M. Chlorophyll Pigments as Nature Based Dye for Dye-Sensitized Solar Cell (DSSC). *Energy Procedia* **79**, 896–902 (2015).

33. Supriyanto, A., Nurosyid, F. & Ahliha, A. H. Carotenoid pigment as sensitizers for applications of dye-sensitized solar cell (DSSC). *IOP Conf. Ser. Mater. Sci. Eng.* **432**, 012060 (2018).

34. Maddah, H. A., Berry, V. & Behura, S. K. Biomolecular photosensitizers for dye-sensitized solar cells: Recent developments and critical insights. *Renew. Sustain. Energy Rev.* **121**, 109678 (2020).

35. Shalini, S., Balasundara prabhu, R., Prasanna, S., Mallick, T. K. & Senthilarasu, S. Review on natural dye sensitized solar cells: Operation, materials and methods. *Renew. Sustain. Energy Rev.* **51**, 1306–1325 (2015).

36. Saleem, H. & Karmalkar, S. An Analytical Method to Extract the Physical Parameters of a Solar Cell From Four Points on the Illuminated J-V Curve. *IEEE Electron Device Lett.* **30**, 349–352 (2009).

37. Burlingame, Q., Ball, M. & Loo, Y.-L. It's time to focus on organic solar cell stability. *Nat. Energy* **5**, 947–949 (2020).

38. Ciulla, G., Lo Brano, V., Di Dio, V. & Cipriani, G. A comparison of different one-diode models for the representation of I–V characteristic of a PV cell. *Renew. Sustain. Energy Rev.* **32**, 684–696 (2014).

39. Fabregat-Santiago, F., Garcia-Belmonte, G., Mora-Seró, I. & Bisquert, J. Characterization of nanostructured hybrid and organic solar cells by impedance spectroscopy. *Phys Chem Chem Phys* **13**, 9083–9118 (2011).

40. Chen, B. *et al.* Impact of Capacitive Effect and Ion Migration on the Hysteretic Behavior of Perovskite Solar Cells. *J. Phys. Chem. Lett.* **6**, 4693–4700 (2015).

41. Habisreutinger, S. N., Noel, N. K. & Snaith, H. J. Hysteresis Index: A Figure without Merit for Quantifying Hysteresis in Perovskite Solar Cells. *ACS Energy Lett.* **3**, 2472–2476 (2018).

42. Saliba, M. & Etgar, L. Current Density Mismatch in Perovskite Solar Cells. *ACS Energy Lett.* **5**, 2886–2888 (2020).

43. Tai, Q. & Yan, F. Emerging Semitransparent Solar Cells: Materials and Device Design. *Adv. Mater.* **29**, 1700192 (2017).

44. Cinà, L., Taheri, B., Reale, A. & Di Carlo, A. Diffusion Length Mapping for Dye-Sensitized Solar Cells. *Energies* **9**, 686 (2016).
45. Castro-Hermosa, S. *et al.* Efficient fully blade-coated perovskite solar cells in air with nanometer-thick bathocuproine buffer layer. *Nano Res.* **14**, 1034–1042 (2021).
46. Bliss, M. *et al.* Spectral Response Measurements of Perovskite Solar Cells. *IEEE J. Photovolt.* **9**, 220–226 (2019).
47. Takagi, K., Magaino, S., Saito, H., Aoki, T. & Aoki, D. Measurements and evaluation of dye-sensitized solar cell performance. *J. Photochem. Photobiol. C Photochem. Rev.* **14**, 1–12 (2013).
48. Curtis, H. B. *Errors in short circuit current measurements due to spectral mismatch between sunlight and solar simulators*. https://www.osti.gov/biblio/7310840 (1976).
49. Mathews, I., Kantareddy, S. N., Buonassisi, T. & Peters, I. M. Technology and Market Perspective for Indoor Photovoltaic Cells. *Joule* **3**, 1415–1426 (2019).
50. Burkhard, G. F., Hoke, E. T. & McGehee, M. D. Accounting for Interference, Scattering, and Electrode Absorption to Make Accurate Internal Quantum Efficiency Measurements in Organic and Other Thin Solar Cells. *Adv. Mater.* **22**, 3293–3297 (2010).
51. Margulis, G. Y., Hardin, B. E., Ding, I.-K., Hoke, E. T. & McGehee, M. D. Parasitic Absorption and Internal Quantum Efficiency Measurements of Solid-State Dye Sensitized Solar Cells. *Adv. Energy Mater.* **3**, 959–966 (2013).
52. Pettersson, L. A. A., Roman, L. S. & Inganäs, O. Modeling photocurrent action spectra of photovoltaic devices based on organic thin films. *J. Appl. Phys.* **86**, 487–496 (1999).
53. Ball, J. M. *et al.* Optical properties and limiting photocurrent of thin-film perovskite solar cells. *Energy Environ. Sci.* **8**, 602–609 (2015).
54. Meinardi, F., Bruni, F. & Brovelli, S. Luminescent solar concentrators for building-integrated photovoltaics. *Nat. Rev. Mater.* **2**, 1–9 (2017).
55. Corsini, F. *et al.* Large-Area Semi-Transparent Luminescent Solar Concentrators Based on Large Stokes Shift Aggregation-Induced Fluorinated Emitters Obtained Through a Sustainable Synthetic Approach. *Adv. Opt. Mater.* **9**, 2100182 (2021).
56. Papucci, C. *et al.* Luminescent solar concentrators with outstanding optical properties by employment of D–A–D quinoxaline fluorophores. *J. Mater. Chem. C* **9**, 15608–15621 (2021).
57. Hermann, A. M. Luminescent solar concentrators—A review. *Sol. Energy* **29**, 323–329 (1982).
58. Debije, M. G., Evans, R. C. & Griffini, G. Laboratory protocols for measuring and reporting the performance of luminescent solar concentrators. *Energy Environ. Sci.* **14**, 293–301 (2021).
59. de Clercq, D. M., Chan, S. V., Hardy, J., Price, M. B. & Davis, N. J. L. K. Reducing reabsorption in luminescent solar concentrators with a self-assembling polymer matrix. *J. Lumin.* **236**, 118095 (2021).
60. Matrone, G. M. *et al.* Electrical and Optical Modulation of a PEDOT:PSS-Based Electrochemical Transistor for Multiple Neurotransmitter-Mediated Artificial Synapses. *Adv. Mater. Technol.* **8**, 2201911 (2023).
61. Marković, D., Mizrahi, A., Querlioz, D. & Grollier, J. Physics for neuromorphic computing. *Nat. Rev. Phys.* **2**, 499–510 (2020).
62. Masood, M. T. Solution-Processable Compact and Mesoporous Titanium Dioxide Thin Films as Electron-Selective Layers for Perovskite Solar Cells. (2020).
63. Bhalla, A. S., Guo, R. & Roy, R. The perovskite structure—a review of its role in ceramic science and technology. *Mater. Res. Innov.* **4**, 3–26 (2000).
64. Cho, H. *et al.* Overcoming the electroluminescence efficiency limitations of perovskite light-emitting diodes. *Science* **350**, 1222–1225 (2015).

65. Gil-Escrig, L. *et al.* Efficient photovoltaic and electroluminescent perovskite devices. *Chem. Commun.* **51**, 569–571 (2014).

66. Sandberg, O. J., Tvingstedt, K., Meredith, P. & Armin, A. Theoretical Perspective on Transient Photovoltage and Charge Extraction Techniques. *J. Phys. Chem. C* **123**, 14261–14271 (2019).

67. Palomares, E. *et al.* Chapter 7 - Photovoltage/photocurrent transient techniques. in *Characterization Techniques for Perovskite Solar Cell Materials* (eds. Pazoki, M., Hagfeldt, A. & Edvinsson, T.) 161–180 (Elsevier, 2020). doi:10.1016/B978-0-12-814727-6.00007-4.

68. Roiati, V. *et al.* Investigating charge dynamics in halide perovskite-sensitized mesostructured solar cells. *Energy Env. Sci* **7**, 1889–1894 (2014).

69. Elliott, L. C. C. *et al.* Probing Charge Recombination Dynamics in Organic Photovoltaic Devices under OpenCircuit Conditions. **4**, 1400356 (2014).

70. Boyd, C. C., Cheacharoen, R., Leijtens, T. & McGehee, M. D. Understanding Degradation Mechanisms and Improving Stability of Perovskite Photovoltaics. *Chem. Rev.* **119**, 3418–3451 (2019).

71. Cheng, Y. & Ding, L. Pushing commercialization of perovskite solar cells by improving their intrinsic stability. *Energy Environ. Sci.* **14**, 3233–3255 (2021).

72. Zhang, D., Li, D., Hu, Y., Mei, A. & Han, H. Degradation pathways in perovskite solar cells and how to meet international standards. *Commun. Mater.* **3**, 1–14 (2022).

73. Bisquert, J. & Juarez-Perez, E. J. The Causes of Degradation of Perovskite Solar Cells. *J. Phys. Chem. Lett.* **10**, 5889–5891 (2019).

74. Guo, R. *et al.* Degradation mechanisms of perovskite solar cells under vacuum and one atmosphere of nitrogen. *Nat. Energy* **6**, (2021).

75. Domanski, K., Alharbi, E. A., Hagfeldt, A., Grätzel, M. & Tress, W. Systematic investigation of the impact of operation conditions on the degradation behaviour of perovskite solar cells. *Nat. Energy* **3**, 61–67 (2018).

76. Tress, W. *et al.* Interpretation and evolution of open-circuit voltage, recombination, ideality factor and subgap defect states during reversible light-soaking and irreversible degradation of perovskite solar cells. *Energy Environ. Sci.* **11**, 151–165 (2018).

77. Caprioglio, P. *et al.* Open-circuit and short-circuit loss management in wide-gap perovskite p-i-n solar cells. *Nat. Commun.* **14**, 932 (2023).

78. Femia, N., Petrone, G., Spagnuolo, G. & Vitelli, M. Optimization of perturb and observe maximum power point tracking method. *IEEE Trans. Power Electron.* **20**, 963–973 (2005).

79. Sera, D., Mathe, L., Kerekes, T., Spataru, S. V. & Teodorescu, R. On the Perturb-and-Observe and Incremental Conductance MPPT Methods for PV Systems. *IEEE J. Photovolt.* **3**, 1070–1078 (2013).

80. Hua, C.-C. & Chen, Y. Modified perturb and observe MPPT with zero oscillation in steady-state for PV systems under partial shaded conditions. in *2017 IEEE Conference on Energy Conversion (CENCON)* 5–9 (2017). doi:10.1109/CENCON.2017.8262448.

81. Ma, S. *et al.* Development of encapsulation strategies towards the commercialization of perovskite solar cells. *Energy Environ. Sci.* **15**, 13–55 (2022).

82. Uddin, A., Upama, M. B., Yi, H. & Duan, L. Encapsulation of Organic and Perovskite Solar Cells: A Review. *Coatings* **9**, 65 (2019).

83. Channa, I. A., Distler, A., Zaiser, M., Brabec, C. J. & Egelhaaf, H.-J. Thin Film Encapsulation of Organic Solar Cells by Direct Deposition of Polysilazanes from Solution. *Adv. Energy Mater.* **9**, 1900598 (2019).

84. Khenkin, M. V. *et al.* Consensus statement for stability assessment and reporting for perovskite photovoltaics based on ISOS procedures. *Nat. Energy* **5**, 35–49 (2020).

85. Zhao, X. *et al.* Accelerated aging of all-inorganic, interface-stabilized perovskite solar cells. *Science* **377**, 307–310 (2022).